Astronomy & Astrophysics manuscript no. AGILESecondCatalogPublishedVersionV2_Arxiv ©ESO 2020
January 11, 2020

Second AGILE catalogue of gamma-ray sources*

A. Bulgarelli[1], V. Fioretti[1], N. Parmiggiani[1], F. Verrecchia[2,3], C. Pittori[2,3], F. Lucarelli[2,3], M. Tavani[4,5,6,7], A. Aboudan[7,12], M. Cardillo[4], A. Giuliani[8], P. W. Cattaneo[9], A.W. Chen[15], G. Piano[4], A. Rappoldi[9], L. Baroncelli[7], A. Argan[4], L.A. Antonelli[3], I. Donnarumma[4,16], F. Gianotti[1], P. Giommi[16], M. Giusti[4,5], F. Longo[13,14], A. Pellizzoni[10], M. Pilia[10], M. Trifoglio[1], A. Trois[10], S. Vercellone[11], A. Zoli[1]

[1] INAF-OAS Bologna, via Gobetti 93/3, I-40129 Bologna, Italy.
[2] ASI Space Science Data Center (SSDC), Via del Politecnico snc, 00133 Roma, Italy.
[3] INAF-Osservatorio Astronomico di Roma, Via di Frascati 33, I-00078 Monte Porzio Catone, Italy.
[4] INAF-IAPS Roma, via del Fosso del Cavaliere 100, I-00133 Roma, Italy.
[5] Dipartimento di Fisica, Università Tor Vergata, via della Ricerca Scientifica 1,I-00133 Roma, Italy.
[6] INFN Roma Tor Vergata, via della Ricerca Scientifica 1, I-00133 Roma, Italy.
[7] Consorzio Interuniversitario Fisica Spaziale (CIFS), villa Gualino - v.le Settimio Severo 63, I-10133 Torino, Italy.
[8] INAF-IASF Milano, via E. Bassini 15, I-20133 Milano, Italy.
[9] INFN Pavia, via Bassi 6, I-27100 Pavia, Italy.
[10] INAF-Osservatorio Astronomico di Cagliari, via della Scienza 5, I-09047, Selargius (CA), Italy.
[11] INAF–Osservatorio Astronomico di Brera, Via E. Bianchi 46, I-23807 Merate (LC), Italy.
[12] CISAS, University of Padova, Padova, Italy.
[13] Dipartimento di Fisica, University of Trieste, via Valerio 2, 34127 Trieste
[14] INFN, sezione di Trieste, via Valerio 2, 34127 Trieste
[15] School of Physics, University of the Witwatersrand, 1 Jan Smuts Avenue, Braamfontein, Johannesburg, 2050 South Africa.
[16] ASI, Via del Politecnico snc, 00133 Roma, Italy.

Published online 25 June 2019, A&A 627, A13 (2019)

ABSTRACT

Aims. We present the second AGILE-GRID catalogue (2AGL) of γ-ray sources in the energy range 100 MeV – 10 GeV.
Methods. With respect to previous AGILE-GRID catalogues, the current 2AGL catalogue is based on the first 2.3 years of science data from the AGILE mission (the so-called pointing mode) and incorporates more data and several analysis improvements, including better calibrations at the event reconstruction level, an updated model for the Galactic diffuse γ-ray emission, a refined procedure for point-like source detection, and the inclusion of a search for extended γ-ray sources.
Results. The 2AGL catalogue includes 175 high-confidence sources (above 4σ significance) with their location regions and spectral properties and a variability analysis with four-day light curves for the most significant. Relying on the error region of each source position, including systematic uncertainties, 122 sources are considered as positionally associated with known counterparts at different wavelengths or detected by other γ-ray instruments. Among the identified or associated sources, 62 are active galactic nuclei (AGNs) of the blazar class. Pulsars represent the largest Galactic source class, with 41 associated pulsars, 7 of which have detected pulsation; 8 supernova remnants and 4 high-mass X-ray binaries have also been identified. A substantial number of 2AGL sources are unidentified: for 53 sources no known counterpart is found at different wavelengths. Among these sources, we discuss a subclass of 29 AGILE-GRID-only γ-ray sources that are not present in 1FGL, 2FGL, or 3FGL catalogues; the remaining sources are unidentified in both 2AGL and 3FGL catalogues. We also present an extension of the analysis of 2AGL sources detected in the energy range 50 – 100 MeV.

Key words. gamma rays: general – catalogue – survey

1. Introduction

This paper presents the 2AGL catalogue of high-energy γ-ray sources detected by the AGILE Gamma-Ray Imager Detector (GRID) in the energy range 100 MeV – 10 GeV during the first 2.3 years of operations (2007-2009) in the so-called pointing mode. This paper follows three previously published papers: the first AGILE-GRID catalogue of γ-ray sources (1AGL; Pittori et al. 2009), the catalogue of variable γ-ray sources during the first 2.3 years of observations (1AGLR; Verrecchia et al. 2013), and a paper dedicated to the search of AGILE-GRID TeV source counterparts (Rappoldi et al. 2016). Compared to previous investigations, we have implemented several refinements in the analysis of γ-ray sources as follows:

1. A new background event filter, called FM3.119, and new instrument response functions (IRFs), called H0025, were used. The main differences relative to the previous F4 event filter used for the 1AGL catalogue are an improved effective area ($A_{\rm eff}$) above 100 MeV and a better characterisation of

Send offprint requests to: A. Bulgarelli, e-mail: andrea.bulgarelli@inaf.it. * Full Tables 10 and 11 (the catalog) are available at the CDS (Strasbourg astronomical Data Center) via anonymous ftp to cdsarc.u-strasbg.fr (130.79.128.5) or via http://cdsarc.u-strasbg.fr/viz-bin/qcat?J/A+A/627/A13. Text is also available at https://doi.org/10.1051/0004-6361/201834143

the point spread function (PSF) (Chen et al. 2013; Sabatini et al. 2015). In addition, systematic errors of the IRFs were estimated with greater accuracy.
2. We analyse a larger data set than in the 1AGL, which was based on the first 12 months of observations from July 13, 2007 to June 30, 2008. The 2AGL catalogue is, indeed, based on the entire pointing mode period corresponding to 2.3 years from July 13, 2007 to October 15, 2009.
3. This catalogue employs a new diffuse Galactic emission model, in particular for the Galactic central region.
4. We developed new methods for characterising and localising source candidate seeds, then evaluated for inclusion in the catalogue, using both wavelet techniques and an iterative approach.
5. In the search for associations of AGILE-GRID sources with counterparts at different wavelengths, we used new association procedures.
6. A new version of the AGILE-GRID Science Tools was used (BUILD25), which is publicly available from the AGILE website at SSDC[1].
7. Energy dispersion (Chen et al. 2013) has been taken into account in the analysis with the new science tools.

The outline of the paper is as follows. In Sect.2 we describe the instrument, data reduction, and pointing strategy. In Sect. 3 we describe the AGILE-GRID γ-ray background models used in the data analysis. We then present in Sect. 4 the analysis methods used to build the second AGILE-GRID catalogue of γ-ray sources; 2AGL. Limitations and systematic uncertainties are described in Sect. 5. Our results and the list of the 2AGL γ-ray sources are shown in Sect. 6, where potential counterparts at other wavelengths and correspondences with Fermi-LAT catalogue sources are also discussed. In Sect. 7 we comment on some specific 2AGL sources, divided by classes or sky regions. In Sect. 8 we report on an extension of the 2AGL catalogue where the sources detected in the energy range 50 – 100 MeV are listed. Finally, in Sect. 9, we discuss our results and make some concluding remarks.

2. AGILE-GRID instrument, data, and observations

2.1. AGILE-GRID instrument

AGILE (Astrorivelatore Gamma ad Immagini LEggero) Tavani et al. (2008, 2009a) is a mission of the Italian Space Agency (ASI) devoted to γ-ray and X-ray astrophysics in the energy ranges 30 MeV – 50 GeV, and 18 – 60 keV, respectively. AGILE was successfully launched on 23 April 2007 in a $\sim$ 550 km equatorial orbit with low inclination angle, $\sim 2.5°$.

AGILE was the only mission entirely dedicated to high-energy astrophysics above 30 MeV during the April 2007-June 2008 period. Later it has operated together with the Fermi Large Area Telescope (LAT), launched on June 11, 2008 (Michelson 2008; Atwood et al. 2009). The highly innovative AGILE-GRID instrument is the first of the current generation of high-energy space missions based on solid-state silicon technology.

The AGILE payload detector consists of the silicon tracker (ST) (Barbiellini et al. 2001; Prest et al. 2003; Bulgarelli et al. 2010; Cattaneo et al. 2011) the Super-AGILE X-ray detector (Feroci et al. 2007), the CsI(Tl) Mini-Calorimeter (MCAL) (Labanti et al. 2009), and an anticoincidence (AC) system (Perotti et al. 2006). The combination of ST, MCAL, and AC forms the Gamma-Ray Imaging Detector (GRID). Accurate timing, positional, and attitude information is provided by the precise positioning System and the two star sensor units. The ST is the core of the AGILE-GRID and plays two roles at the same time: it converts the γ-rays in heavy-Z material layers (245 mm of Tungsten, 0.07 radiation length), where the photon interacts producing an e^+e^- pair in the detector, and records the electron/positron tracks by a sophisticated combination of silicon microstrip detectors and associated readout, providing 3D hits. The ST consists of a total of 12 trays, the first 10 with the Tungsten converter foil followed by two layers of 16 single-sided, 410 μm thick, 9.5×9.5 cm^2 silicon detectors with strips orthogonal to each other, the last two trays consisting only of the silicon detectors. The MCAL instrument is composed of 30 CsI(Tl) scintillator bars each one $15 \times 23 \times 375$ mm^3 in size, arranged in two orthogonal layers, for a total thickness of 1.5 radiation lengths. In each bar the readout of the scintillation light is accomplished by two custom PIN photodiodes (PD) coupled one at each small side of the bar. The AC system is aimed at a very efficient charged particle background rejection. It completely surrounds all AGILE detectors (Super-AGILE, ST, and MCAL). Each lateral face is segmented in three plastic scintillator layers (0.6 cm thick) connected to photomultipliers placed at the bottom of the panels. A single plastic scintillator layer (0.5 cm thick) constitutes the top-AC whose signal is read by four light photomultipliers placed at the four corners of the structure frame. The AGILE-GRID event processing is operated by on-board trigger logic algorithms (Argan et al. 2004) and by on-ground event filtering (see Sect. 2.2).

2.2. AGILE-GRID response characteristics

Energy estimation and direction reconstruction. The track reconstruction for energy estimation and event direction reconstruction is carried out by an AGILE-GRID specific implementation of the Kalman Filter technique (Giuliani et al. 2006) and provides the incident direction and the energy of the events in the AGILE-GRID reference system.

On-ground background event filter. The FM3.119 is the currently used on-ground background event filter for the scientific analysis of the AGILE-GRID data. The filter assigns a classification flag to each event depending on whether it is recognised as a γ-ray event, a charged particle, a "single-track" event, or an event of uncertain classification (limbo). The filter is based on a boosted decision tree (BDT) technique; this technique is used with success in high-energy physics (HEP) experiments (Yang et al. 2005) in order to select events of interest, the so-called signal events, out of numerous background events. The BDT technique maximises the signal-to-background ratio, efficiently suppressing the background events and, in the meanwhile, keeping a high signal detection efficiency. The selection is done on a majority vote on the result of several decision trees, which are all derived from the same training sample by supplying different event weights during the training. For the development of the FM3.119 filter these techniques have been tuned with one sample of Monte Carlo events, the training sample, and then tested with an independent Monte Carlo sample, i.e. the testing sample. From these simulations 182 descriptor parameters of the interacting event inside the AGILE-GRID are extracted and used for training, with the aim of selecting a subset of these descriptor parameters as discriminant input variables for optimising the event separation. A final set of 57 discriminant variables has been selected; an additional post-fitting set of cuts further improves the signal-to-noise ratio, also comprising the previously developed more stringent F4 on-ground background

[1] http://agile.ssdc.asi.it

event filter, optimised for a good pattern recognition of a sub-class of γ-ray events.

Instrument response functions. The effective area ($A_{\rm eff}$), the PSF, and the energy dispersion probability (EDP), collectively referred to as the IRFs, depend on the direction of the incoming γ-ray in instrument coordinates. New efforts in the development of the background rejection filter FM3.119 led to reprocessing all AGILE-GRID data with the new IRFs H0025. The $A_{\rm eff}$ above 100 MeV is improved with a precise characterisation of the PSF with flight data (Chen et al. (2013); Sabatini et al. (2015)). The IRFs I0023 analysed in (Chen et al. 2013) are the same as H0025, except for a different boundary of two energy channels: we have 100 – 400 MeV, 400 – 1000 MeV in I0023, and 100 – 300 MeV, 300 – 1000 MeV in H0025. Both AGILE-GRID PSF and $A_{\rm eff}$ are characterised by a very good off-axis performance and are well calibrated up to almost 60°, showing a very smooth variations with the angle relative to the instrument axis (Chen et al. 2013). On-ground calibrations were also used to characterise the performances of the FM3.119 filter and to validate the new IRFs (Cattaneo et al. 2018). In addition, systematic errors of the IRFs are better characterised (see Sect. 5.1). The scientific performances of the AGILE-GRID can be summarised as follows: $A_{\rm eff}$ ~ 400 cm^2 at 100 MeV, field of view (FoV) ~ 2.5 sr, energy range 30 MeV – 50 GeV, and a PSF at 30° off-axis for $E > 100$ MeV of 2.1°, for $E > 400$ MeV of 1.1°, and for $E > 1$ GeV of 0.8°.

2.3. Data reduction

All AGILE-GRID data are routinely processed using the scientific data reduction software tasks developed by the AGILE team and integrated into an automatic pipeline system developed at the ASI Space Science Data Center (ASI/SSDC). The first step of the data reduction pipeline converts on a contact-by-contact basis the satellite data time into Terrestrial Time (TT), and performs some preliminary calculations and unit conversions. A second step consists in the γ-ray event reconstruction with the AGILE-GRID implementation of the Kalman filter technique. The background event filter FM3.119 is then applied and a classification flag is assigned to each event. An AGILE auxiliary file (LOG) is then created, containing all the spacecraft information relevant to the computation of the effective exposure and GTI (good time interval). Finally, the event direction in sky coordinates is reconstructed and reported in the AGILE event files (EVT), excluding events flagged as charged background particles. This step produces the Level-2 (LV2) archive of LOG and EVT files, that have been used for the construction of this catalogue. The AGILE-GRID data obtained both in pointing and in spinning mode are publicly available from the ASI/SSDC[2].

2.4. Observations

The 2AGL catalogue sensitivity is not uniform, reflecting the inhomogeneous AGILE-GRID sky coverage during the “pointing period”, with a mean exposure focussed mainly towards the Galactic plane: this means that the catalogue covers the entire sky with this observational bias. In addition, the sensitivity is not intrinsically uniform over the sky owing to the large range of brightness of the foreground diffuse Galactic γ-ray emission. The total γ-ray exposure and intensity maps obtained over the selected period with the FM3.119 filter, in Hammer-Aitoff projection and Galactic coordinates, are shown in Fig. 1 and Fig. 2, respectively. Exposure values span from 1 to 20235 cm^2 s sr; 10% of the pixels have a value of less than 1200 cm^2 s sr, which corresponds to about 16 days of effective exposure. This is the minimum exposure value corresponding to a 2AGL source detection.

The AGILE Commissioning ended on July 9, 2007, and the following science verification phase lasted about four months, up to November 30, 2007. On December 1, 2007 the baseline nominal observations and pointing plan of AO Cycle-1 (AO-1) started with the Guest Observer programme, in which the AGILE spacecraft operated in pointing mode until October 15, 2009, and completing 101 pointings called observation blocks (OBs); see Table 1.

The AGILE pointings are subject to illumination constraints requiring that the fixed solar panels always be orientated within 3° from the Sun direction. The OBs usually consisted of predefined long exposures, drifting about 1° per day with respect to the initial boresight direction to obey solar panels constraints. The strategy that drove the pointing history during the first two years of observations (Cycle-1 and Cycle-2) reflected the need to achieve a good balance between Galactic and extragalactic targets as well as optimal observability from both space- and ground-based facilities.

The AGILE Pointing Plan has been prepared, taking several scientific and operational requirements into account, such as

- maximisation of the overall sky exposure factor by limiting the observation of the sky regions more affected by Earth occultation;
- substantial exposure of the Galactic plane and in particular of the Galactic center and of the Cygnus regions during Cycle-1 to achieve long timescale monitoring of Galactic γ-ray and hard X-ray sources;
- maximisation of the scientific output of the mission during Cycle-2 in co-presence with the Fermi satellite, looking for confirmation of transient activity from several candidates detected during Cycle-1.

The AGILE Pointing Plan was aimed in particular at reaching specific scientific goals, including

- large photon counting statistic for γ-ray pulsar candidates;
- improved positioning of the majority of unidentified γ-ray sources concentrated in the galactic plane;
- micro-quasar studies with simultaneous hard X-ray and γ-ray data;
- determination of the origin of γ-ray emission associated with a selected list of supernova remnants (SNR);
- an improvement of the γ-ray Galactic diffuse emission model and of the Galactic cosmic-ray (CR) propagation and interaction in specific regions.

Because of the transient nature of the majority of extragalactic γ-ray sources and of many new γ-ray candidates in our Galaxy, and taking into account the large FoV of the AGILE-GRID, the general strategy to reconcile extragalactic and Galactic investigations within a single observing plan, was to carry out 4 to 6 Target of Opportunity (ToO) repointings per year due to source flaring activity. Nine repointings were actually carried out resulting from Galactic or extragalactic flaring activity, for a total of 12 ToO OBs out of 101 (3 of which have been extension of previous ones.) These 9 ToO repointings had a minimal impact (about 9%) on the long-duration baseline coverage of the Galactic plane. There is however an observational bias regarding a few

[2] https://www.asdc.asi.it/mmia/index.php?mission=agilemmia

well-known high-latitude blazars such as 3C279 and PKS 0537-441, which in the 2AGL have an high average flux value because they have been mainly observed in ToO pointings during flares.

A γ-ray flare monitoring programme has been active on a daily basis since the beginning of the mission, and has a dedicated alert system that is implemented within the AGILE Ground Segment and a Flare Advocate working group. Details are reported in (Bulgarelli et al. 2014; Pittori et al. 2013).

Since November 2009, because of a failure of the spacecraft reaction wheel, the attitude control system was reconfigured and the scientific mode of operation was changed. Currently the instrument operates in spinning mode, i.e. the instrument scans the sky with an angular velocity of about $0.8^{\circ}\mathrm{s}^{-1}$, resulting in an exposure of about 7×10^{6} cm^{2} s for about 70% of the sky in one day.

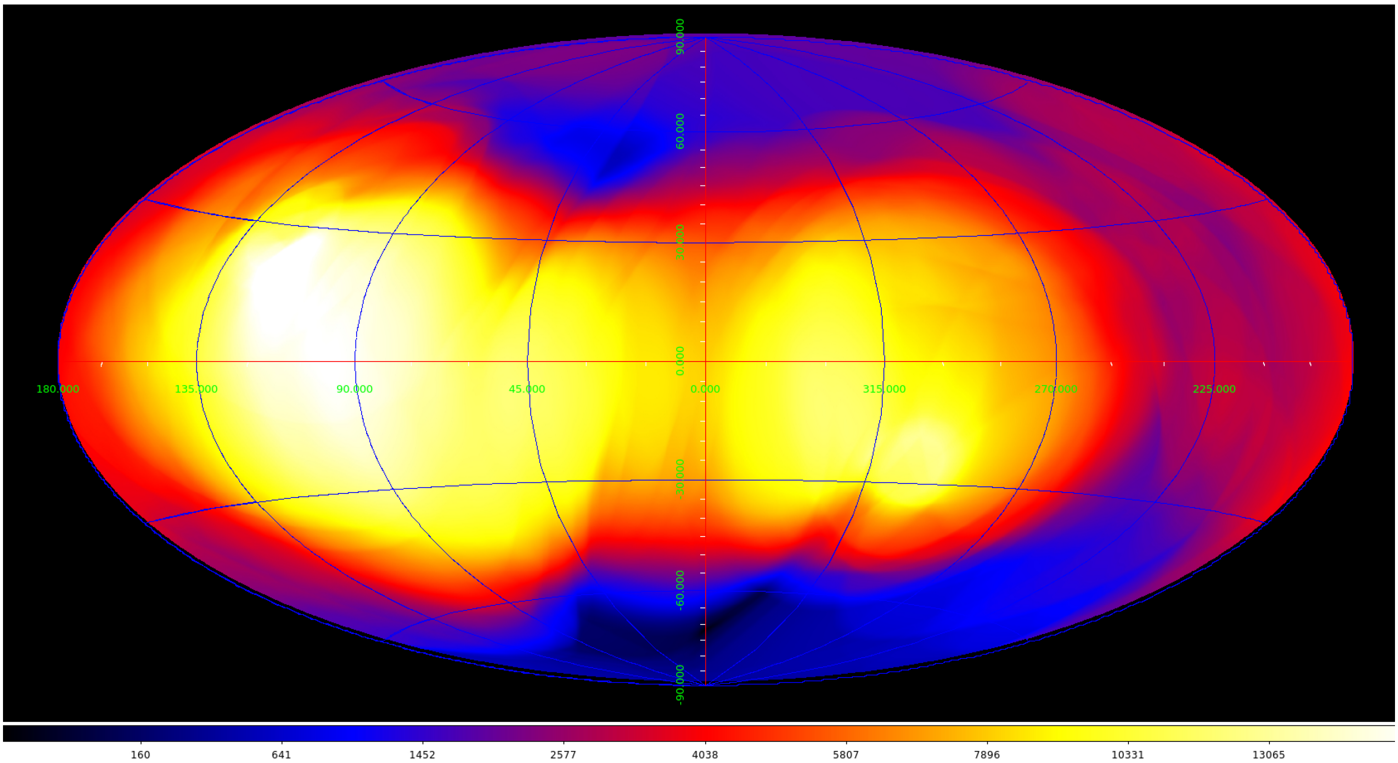

Fig. 1: Squared root scaled exposure sky map in the energy range 100 MeV – 10 GeV in Galactic coordinates and Hammer-Aitoff projection for the 2.3-year period analysed for the 2AGL catalogue (expressed in units of cm^2 s sr). Bin size = 0.1°.

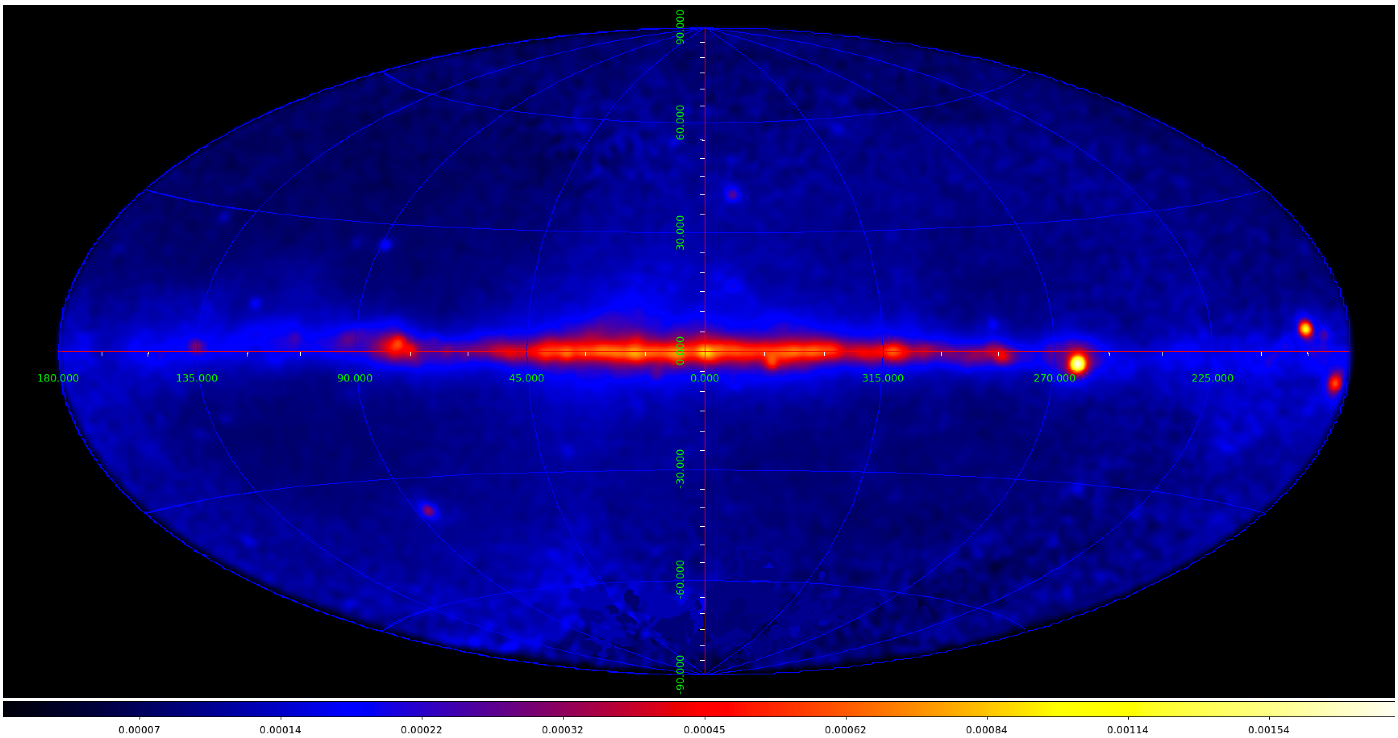

Fig. 2: Intensity map in the 100 MeV – 10 GeV energy band in Galactic coordinates and Hammer-Aitoff projection for the 2.3-year period analysed for the 2AGL catalogue (expressed in units of ph $cm^{-2}s^{-1}sr^{-1}$). Bin size = 0.1°.

Region name	OB number	Starting RA, Dec J2000 (deg)	Starting LII, BII (deg)	Observation start (UTC)	Observation end (UTC)	Observation start (MJD)	Observation end (MJD)
3C279 Region	900	195.596 , -6.649	307.8118 , 56.1183	2007-07-09 12:00	2007-07-13 12:00	54290.500	54294.500
VELA Region	1000	157.979 , -60.214	286.4188 , -1.8951	2007-07-13 12:00	2007-07-24 12:00	54294.500	54305.500
ToO 3C 454.3	1100	17.829 , 36.694	127.3645 , -26.0059	2007-07-24 12:00	2007-07-30 12:00	54305.500	54311.500
ToO 3C 454.3	1150	17.829 , 36.694	127.3645 , -26.0059	2007-07-24 12:00	2007-07-30 12:00	54305.500	54311.500
VELA Region	1200	150.836 , -70.19	289.5293 , -11.8265	2007-07-30 12:00	2007-08-01 12:00	54311.500	54313.500
SA Crab -45	1300	37.097 , 12.712	156.5885 , -43.7329	2007-08-01 12:00	2007-08-02 12:00	54313.500	54314.500
VELA Region	1400	176.006 , -66.063	296.1593 , -4.0824	2007-08-02 12:00	2007-08-12 12:00	54314.500	54324.500
SA Crab -35	1500	47.41 , 16.075	164.8343 , -35.3162	2007-08-12 12:00	2007-08-13 12:00	54324.500	54325.500
VELA Region	1600	195.551 , -66.564	304.0044 , -3.7154	2007-08-13 12:00	2007-08-22 12:00	54325.500	54334.500
SA Crab -25	1700	57.139 , 18.566	171.0790 , -27.3115	2007-08-22 12:00	2007-08-23 12:00	54334.500	54335.500
VELA Region	1800	216.979 , -64.437	313.1071 , -3.4890	2007-08-23 12:00	2007-08-27 12:00	54335.500	54339.500
Galactic Plane	1900	236.570 , -41.874	334.4369 , 10.0581	2007-08-27 12:00	2007-09-01 12:00	54339.500	54344.500
SA Crab (15,15)	2000	69.483 , 5.592	190.8962 , -26.2858	2007-09-01 12:00	2007-09-02 12:00	54344.500	54345.500
SA Crab (0,15)	2100	68.205 , 20.566	177.1349 , -18.2781	2007-09-02 12:00	2007-09-03 12:00	54345.500	54346.500
SA Crab (-15,15)	2200	66.651 , 35.559	164.6334 , -9.3529	2007-09-03 12:00	2007-09-04 12:00	54346.500	54347.500
Field 8	2300	51.408 , 71.022	134.8816 , 11.8210	2007-09-04 12:00	2007-09-12 12:00	54347.500	54355.500
SA Crab (0,5)	2400	78.535 , 21.730	182.1630 , -9.8874	2007-09-12 12:00	2007-09-13 12:00	54355.500	54356.500
Field 8	2500	74.882 , 58.334	150.9906 , 9.7255	2007-09-13 12:00	2007-09-15 12:00	54356.500	54358.500
SA Crab (45,0)	2600	84.212 , -23.014	226.7035 , -26.1161	2007-09-15 12:00	2007-09-16 12:00	54358.500	54359.500
SA Crab (5,0)	2700	82.987 , 16.983	188.5217 , -8.9833	2007-09-16 12:00	2007-09-17 12:00	54359.500	54360.500
SA Crab (0,0)	2800	83.774 , 22.026	184.6179 , -5.6675	2007-09-17 12:00	2007-09-18 12:00	54360.500	54361.500
SA Crab (-5,0)	2900	84.62 , 27.048	180.7737 , -2.3343	2007-09-18 12:00	2007-09-19 12:00	54361.500	54362.500
SA Crab (-15,0)	3000	85.347 , 37.089	172.5873 , 3.5179	2007-09-19 12:00	2007-09-20 12:00	54362.500	54363.500
SA Crab (-25,0)	3100	86.174 , 47.118	164.2603 , 9.2213	2007-09-20 12:00	2007-09-21 12:00	54363.500	54364.500
SA Crab (-35,0)	3200	87.140 , 57.126	155.6110 , 14.6016	2007-09-21 12:00	2007-09-22 12:00	54364.500	54365.500
SA Crab (-45,0)	3300	88.348 , 67.136	146.4473 , 19.4825	2007-09-22 12:00	2007-09-23 12:00	54365.500	54366.500
SA Crab (0,-5)	3400	90.097 , 22.143	187.5419 , -0.5862	2007-09-23 12:00	2007-09-24 12:00	54366.500	54367.500
SA Crab (15,0)	3500	91.034 , 7.141	201.1056 , -7.1395	2007-09-24 12:00	2007-09-25 12:00	54367.500	54368.500
SA Crab (25,0)	3600	91.838 , -2.882	210.4602 , -11.1195	2007-09-25 12:00	2007-09-26 12:00	54368.500	54369.500
SA Crab (35,0)	3700	92.502 , -12.926	220.0176 , -14.9489	2007-09-26 12:00	2007-09-27 12:00	54369.500	54370.500
Crab Nebula	3800	94.323 , 22.050	189.5211 , 2.7938	2007-09-27 12:00	2007-10-01 12:00	54370.500	54374.500
SA Crab (0,-15)	3900	98.552 , 21.875	191.4932 , 6.1922	2007-10-01 12:00	2007-10-02 12:00	54374.500	54375.500
SA Crab (-15,-15)	4000	100.839 , 36.784	178.6417 , 14.3544	2007-10-02 12:00	2007-10-03 12:00	54375.500	54376.500
SA Crab (15,-15)	4100	99.566 , 6.788	205.3927 , 0.1791	2007-10-03 12:00	2007-10-04 12:00	54376.500	54377.500
Crab Field	4200	101.724 , 21.699	192.9681 , 8.7550	2007-10-04 12:00	2007-10-12 12:00	54377.500	54385.500
SA Crab (0,-25)	4300	110.131 , 20.718	197.2281 , 15.4667	2007-10-12 12:00	2007-10-13 12:00	54385.500	54386.500
Gal. Center	4400	290.920 , -18.896	19.2683 , -15.4110	2007-10-13 12:00	2007-10-22 12:00	54386.500	54395.500
SA Crab (0,-35)	4500	120.494 , 18.879	203.0392 , 23.7444	2007-10-22 12:00	2007-10-23 12:00	54395.500	54396.500
Gal. Center Reg.	4600	301.173 , -17.107	25.0972 , -23.6663	2007-10-23 12:00	2007-10-24 08:00	54396.500	54397.333
ToO 0716+714	4610	148.939 , 67.888	143.3642 , 41.5875	2007-10-24 08:00	2007-10-29 12:00	54397.333	54402.500
ToO Extended	4630	157.461 , 66.942	141.5537 , 44.7248	2007-10-29 12:00	2007-11-01 12:00	54402.500	54405.500
SA Crab (0,-45)	4700	130.614 , 16.339	209.7914 , 31.7351	2007-11-01 12:00	2007-11-02 12:00	54405.500	54406.500
Cygnus Region	4800	296.880 , 34.501	69.5937 , 4.6227	2007-11-02 12:00	2007-12-01 12:00	54406.500	54435.500
Cygnus Field 1	4900	304.432 , 53.552	88.8156 , 9.9272	2007-12-01 12:00	2007-12-05 09:00	54435.500	54439.375
Cygnus Repointing	4910	322.496 , 38.244	85.1187 , -9.4171	2007-12-05 09:00	2007-12-16 12:00	54439.375	54450.500
Cygnus Repointing	4920	322.496 , 38.244	85.1187 , -9.4171	2007-12-05 09:00	2007-12-16 12:00	54439.375	54450.500
Virgo Field	5010	173.433 , -0.437	265.6464 , 56.7005	2007-12-16 12:00	2008-01-08 12:00	54450.500	54473.500
Vela Field	5100	147.060 , -62.517	283.4703 , -6.7881	2008-01-08 12:00	2008-02-01 12:00	54473.500	54497.500
South Gal Pole	5200	58.347 , -37.795	240.3889 , -50.5780	2008-02-01 12:00	2008-02-09 09:00	54497.500	54505.375
ToO MKN 421	5210	250.974 , 50.293	77.3096 , 40.6278	2008-02-09 09:00	2008-02-12 12:00	54505.375	54508.500
South Gal Pole Repointing	5220	65.660 , -35.714	237.5007 , -44.6737	2008-02-12 12:00	2008-02-14 12:00	54508.500	54510.500
Musca Field	5300	191.934 , -71.893	302.6408 , -9.0241	2008-02-14 12:00	2008-03-01 12:00	54510.500	54526.500
Gal. Center 1	5400	243.596 , -50.979	332.1063 , 0.0207	2008-03-01 12:00	2008-03-16 12:00	54526.500	54541.500
Gal. Center 2	5450	265.781 , -28.626	359.9782 , 0.6280	2008-03-16 12:00	2008-03-30 12:00	54541.500	54555.500

Table 1: AGILE observation OBs in pointing mode.

Region name	OB number	Starting RA, Dec J2000 (deg)	Starting LII, BII (deg)	Observation start (UTC)	Observation end (UTC)	Observation start (MJD)	Observation end (MJD)
Anti-Center 1	5500	100.944 , 21.711	192.6369 , 8.1084	2008-03-30 12:00	2008-04-05 12:00	54555.500	54561.500
SA Crab (8,24)	5510	108.283 , 28.625	188.9607 , 16.9953	2008-04-05 12:00	2008-04-07 12:00	54561.500	54563.500
SA Crab (15,26)	5520	111.762 , 35.688	183.0072 , 22.2023	2008-04-07 12:00	2008-04-08 12:00	54563.500	54564.500
Anti-Center 2	5530	110.404 , 20.758	197.2962 , 15.7167	2008-04-08 12:00	2008-04-10 12:00	54564.500	54566.500
Vulpecula Field	5600	286.259 , 20.819	53.0394 , 6.4733	2008-04-10 12:00	2008-04-30 12:00	54566.500	54586.500
North Gal Pole	5700	250.075 , 72.497	104.8522 , 35.4379	2008-04-30 12:00	2008-05-10 12:00	54586.500	54596.500
Cygnus Field 2	5800	304.286 , 35.974	74.0497 , 0.2720	2008-05-10 12:00	2008-06-09 18:00	54596.500	54626.750
ToO WComae ON+231	5810	182.285 , 29.614	195.5016 , 80.3738	2008-06-09 18:00	2008-06-15 12:00	54626.750	54632.500
Cygnus Repointing	5820	323.248 , 50.079	93.6645 , -1.1664	2008-06-15 12:00	2008-06-30 12:00	54632.500	54647.500
Antlia Field	5900	161.83 , -47.73	282.31 , 10.11	2008-06-30 12:00	2008-07-25 18:00	54647.500	54672.750
TOO 3C 454.3	5910	19.37 , 38.09	128.56 , -24.49	2008-07-25 18:00	2008-07-31 12:00	54672.750	54678.500
Extension TOO 3C454.3	5920	25.09 , 40.12	330.46 , 28.98	2008-07-31 12:00	2008-08-15 12:00	54678.500	54693.500
Musca Field 2	6010	175.31 , -74.13	298.10 , -11.92	2008-08-15 12:00	2008-08-31 12:00	54693.500	54709.500
ToO SGR 0501+4516	6110	61.87 , 44.06	333.90 , 27.26	2008-08-31 12:00	2008-09-10 12:00	54709.500	54719.500
Gal. Center 3	6200	256.55 , -28.53	355.51 , 7.40	2008-09-10 12:00	2008-10-10 12:00	54719.500	54749.500
ToO PKS 0537-441	6210	98.80 , -46.77	255.44 , -22.05	2008-10-10 12:00	2008-10-17 12:00	54749.500	54756.500
Aquila Field	6310	290.97 , 10.10	45.62 , -2.51	2008-10-17 12:00	2008-10-31 12:00	54756.500	54770.500
Cygnus Field 3	6400	295.52 , 35.64	70.03 , 6.15	2008-10-31 12:00	2008-11-30 12:00	54770.500	54800.500
Cygnus Field 4	6500	320.40 , 35.50	81.95 , -10.17	2008-11-30 12:00	2008-12-20 12:00	54800.500	54820.500
Cygnus Field 5	6600	334.10 , 44.05	95.70 , -10.47	2008-12-20 12:00	2009-01-12 18:00	54820.500	54843.750
ToO Carina Field	6610	161.67 , -59.86	287.86 , -0.69	2009-01-12 18:00	2009-01-19 18:00	54843.750	54850.750
Cygnus Field 6	6710	325.75 , 68.11	106.75 , 11.37	2009-01-19 18:00	2009-02-28 12:00	54850.750	54890.500
Gal.Center 4	6800	247.20 , -29.03	349.85 , 13.43	2009-02-28 12:00	2009-03-25 12:00	54890.500	54915.500
Gal.Center Prolonged	6810	275.73 , -30.50	2.59 , -7.83	2009-03-25 12:00	2009-03-31 12:00	54915.500	54921.500
Crab Field	6910	102.70 , 31.71	184.07 , 13.75	2009-03-31 12:00	2009-04-07 12:00	54921.500	54928.500
Aquila Field 1	7010	288.88 , -19.31	18.06 , -13.82	2009-04-07 12:00	2009-04-15 12:00	54928.500	54936.500
Aquila Field 2	7100	290.88 , 16.16	50.92 , 0.44	2009-04-15 12:00	2009-04-30 12:00	54936.500	54951.500
Cygnus Field 7	7200	299.11 , 29.78	66.49 , 0.59	2009-04-30 12:00	2009-05-15 12:00	54951.500	54966.500
Vela Field 2	7300	127.35 , -37.14	256.41 , 1.08	2009-05-15 12:00	2009-05-25 18:00	54966.500	54976.750
3rd ToO 3C454.3	7310	328.44 , 10.91	68.32 , -32.54	2009-05-25 18:00	2009-05-29 12:00	54976.750	54980.500
Restart Vela Field 2	7320	136.50 , -40.71	263.67 , 4.38	2009-05-29 12:00	2009-06-04 12:00	54980.500	54986.500
Virgo Field 2	7410	167.14 , 10.71	242.13 , 60.76	2009-06-04 12:00	2009-06-15 12:00	54986.500	54997.500
Cygnus Field 8	7500	330.22 , 43.11	92.83 , -9.58	2009-06-15 12:00	2009-06-25 12:00	54997.500	55007.500
Cygnus Field 9	7600	344.77 , 37.90	99.66 , -19.84	2009-06-25 12:00	2009-07-15 12:00	55007.500	55027.500
Cygnus Field 10	7700	330.35 , 64.26	105.73 , 7.23	2009-07-15 12:00	2009-08-12 12:00	55027.500	55055.500
Vela Field 3	7800	202.30 , -62.10	307.33 , 0.45	2009-08-12 12:00	2009-08-31 12:00	55055.500	55074.500
Norma Field	7900	243.77 , -35.45	343.05 , 11.11	2009-08-31 12:00	2009-09-10 12:00	55074.500	55084.500
SA Crab (15,6)	8000	78.33 , 6.66	195.06 , -18.31	2009-09-10 12:00	2009-09-13 12:00	55084.500	55087.500
SA Crab (25,3)	8100	81.78 , -3.12	205.88 , -20.15	2009-09-13 12:00	2009-09-16 12:00	55087.500	55090.500
Galactic Center 5	8200	263.19 , -23.49	232.78 , -28.89	2009-09-16 12:00	2009-09-30 12:00	55090.500	55104.500
Aquila Field 3	8300	278.13 , -23.22	10.11 , -6.45	2009-09-30 12:00	2009-10-15 12:00	55104.500	55119.500

Table 1: AGILE observation OBs in pointing mode.

3. Background Modelling

3.1. Galactic diffuse γ-ray background

The diffuse γ-ray background is the primary component of the background. It is assumed to be produced by the interaction of CRs with the Galactic interstellar medium, the cosmic microwave background (CMB), and the interstellar radiation field (ISRF) through three physical processes: hadron-hadron collision, Bremsstrahlung, and inverse Compton emission. The model for the diffuse γ-ray background has been updated for the 2AGL catalogue, with an update of the Galactic centre region diffuse γ-ray emission and convolved with the new IRFs H0025.

The AGILE diffuse emission model Giuliani et al. (2004) substantially improves the previous EGRET model by using neutral hydrogen (HI) and CO updated maps to model the matter distribution in the Galaxy. It is based on a 3D grid with $0.1° \times 0.1°$ binning in Galactic longitude and latitude, and a 0.2 kpc step in distance along the line of sight. Concerning the distribution of neutral hydrogen, we use the Leiden-Argentine-Bonn (LAB) survey of Galactic HI Kalberla et al. (2005). The LAB survey improves the previous results especially in terms of sensitivity (by an order of magnitude), velocity range, and resolution. In order to properly project the velocity-resolved radio data, we use the Galactic rotation curves parameterised by (Clemens 1985). The detailed and relatively high-resolution distribution of molecular hydrogen is obtained from the CO observations described in Dame et al. (2001). The CO is assumed to be a tracer of molecular hydrogen, through a known ratio of hydrogen density to CO radio emissivity.

Cosmic rays can emit γ-rays through the inverse Compton mechanism due to their interaction with photons of the CMB and the ISRF. We use the analytical model proposed by Chi & Wolfendale (1991) to account for the latter component. It describes the ISRF as the result of three main contributions: far infrared (due to dust emission), near infrared, and optical/UV (from stellar emission). The CR distribution (both protons and electrons) in the Galaxy is obtained using the GALPROP CR model (Strong et al. 2000). As an example, Fig. 3 reports the AGILE diffuse γ-ray background emission model convolved with PSF and energy dispersion in the energy range 300 MeV – 1 GeV.

3.2. Isotropic background

The (quasi) isotropic background includes both a contribution from the cosmic extragalactic diffuse emission and a component of noise due to residual CR induced backgrounds at the detector level. This residual particle background is dominant in the AGILE data used for this analysis (based on the standard filter FM3.119)[3]. We evaluate the isotropic background with the maximum likelihood estimator (MLE) method in each region within the radius of analysis of each gamma-ray candidate source (see Sect. 4.1). This background is represented by a parameter for each energy bin in the MLE, which could be left free or fixed after its evaluation, taking typical values between $4 - 8 \times 10^{-5}$ cts cm^{-2}s^{-1}sr^{-1} in the energy range 100 MeV – 10 GeV.

[3] Estimate of the pure cosmic extragalactic diffuse emission is out of the scope of this paper, and it would require much more stringent requirements on the purity of the γ-ray event selection (Ackermann et al. (2015)).

3.3. Residual Earth limb

At the ~ 550 km altitude of the (equatorial nearly-circular) orbit of AGILE, the limb of the Earth is an intense source of γ-rays from CR collisions with the upper atmosphere, and during the observations the AGILE-GRID FoV generally subtended part of the Earth limb. Even if an effective on-board background rejection filtering (Argan et al. 2004) is present, a residual component of limb emission remains in the data; to further reduce γ-ray Earth-albedo contamination we limit the data selection and exposure calculations excluding photons coming within 80° from the reconstructed satellite-Earth vector (*albrad*=80), as in the 1AGL and 1AGLR catalogues. The AGILE TeVCat (Rappoldi et al. 2016) uses a more conservative angle cut with a value of *albrad*=85°.

4. Construction of the catalogue

The 2AGL is a catalogue of point-like and extended sources. In this section we report the procedure to construct the 2AGL catalogue, emphasising the differences with respect to the 1AGL catalogue. Most of the procedure reported in this paper is relevant for point-like sources. The analysis of extended sources is described in Sect. 4.9.

The basic analysis steps are source detection and localisation, significance estimation, and spectral shape determination. Each step has been performed with the AGILE-GRID Science Tools (version BUILD25).

4.1. General analysis method

All analyses were performed using a binned MLE method. The analysis depends on the isotropic and Galactic diffuse emission, γ-ray photon statistics, IRFs as functions of energy and off-axis angle, and on the background filtering.

We used a likelihood ratio test to compare two ensembles of models. Each model is a linear combination of parameters for point-like and extended sources, isotropic, and Galactic diffuse γ-ray background components of the γ-ray emission, and in addition to point-like sources with fixed γ-ray emission; the two ensembles of models are a parameter subset of the other. For each ensemble of models the set of free parameters is estimated by fitting the model with the data and computing the maximum likelihoods, where L_0 is the likelihood for the null hypothesis and L_1 is the likelihood for the alternative hypothesis. The likelihood ratio test is L_0/L_1, and the test statistics TS is defined as $TS = -2\ln(L_0/L_1)$ (Mattox et al. 1996; Bulgarelli et al. 2012a). The test statistics TS is used for quantifying how significantly a source emerges from the background (Wilks 1938).

To describe a single point-like source, between four and six parameters are used: two for the position, one for the predicted counts and the remaining for the shape parameters of the spectral model (see Sect. 4.1.2). The results are the predicted source counts, the values of the spectral shape parameters, and the position of the source in Galactic coordinates. The parameters reported in this paper are estimated by a likelihood analysis of the 10° field surrounding the sources and considering nearby sources.

Among the parameters evaluated by MLE, the background is described by the coefficients of the Galactic diffuse (see Sect. 3.1) and isotropic (see Sect. 3.2) background. We have two parameters for each energy bin to describe the Galactic (diffuse) and isotropic γ-ray emission: $g_{\rm gal}$, the coefficient of the Galactic diffuse emission model, and $g_{\rm iso} \times 10^{-5}$cts cm^{-2}s^{-1}sr^{-1}, the

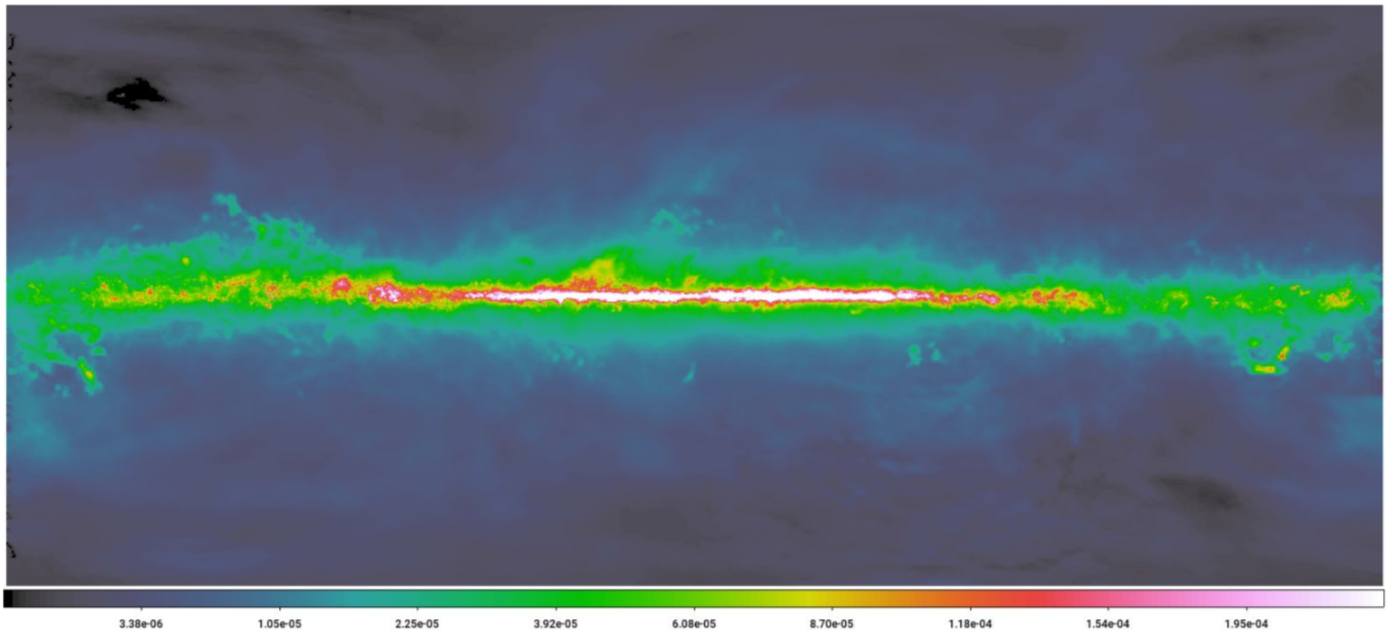

Fig. 3: AGILE diffuse γ-ray background emission model Giuliani et al. (2004) in the energy range 300 MeV – 1 GeV, in ph cm^{-2}s^{-1}sr^{-1}, in plate carree projection with a bin size of 0.1°.

isotropic diffuse intensity. A value of $g_{\rm gal} < 1$ is expected if the Galactic diffuse emission model is correct. An average value of $\bar{g}_{\rm gal} = (0.46 \pm 0.09)$ is obtained in this analysis.

The parameters kept free are estimated by the MLE. It is possible to keep each parameter either free or fixed; a free parameter is allowed to vary to find the maximum likelihood. We varied the point-like source parameters with the following possible combinations: (1) variation of only the flux, (2) variation of position and flux, (3) variation of spectral shape and flux, or (4) variation of all parameters. For the 2AGL catalogue the position, flux, and spectral model parameters were estimated in the same procedure with a global fitting that takes care at the same time, for instance that a shifted position would affect the spectral models or the positions of nearby sources. For some cases described hereafter the number of free parameters is reduced (see Sect. 4.1.1 and 4.1.2).

To describe an extended source we produced a template of the shape of the extended emission at the expected position and we fit this shape with data with a fixed spectral index α (we use $\alpha = 2.1$) of a power law (PL; the only available spectral shape for extended source provided by the AGILE Science Tools), allowing the predicted counts to vary.

The photons were binned into FITS count maps. The γ-ray exposure maps and Galactic diffuse emission maps were then used to calculate the parameters of the models. Particular care is required to carry out the analysis in regions of the Galactic plane that are characterised by a relatively high and structured flux of the diffuse Galactic emission, as well as in regions near bright γ-ray sources leading to possible source confusion.

4.1.1. Localisation

The position of each source was determined by maximising the likelihood with respect to its position, keeping the other parameters of the point-like source free. For each source we evaluated the 95% elliptical and circular confidence regions.

The AGILE Science Tools perform the positional and spectral shape optimisation at the same time, but sometimes the contour is not evaluated during the spectral shape evaluation owing to the high number of free parameters; as consequence, it is not possible to obtain confidence regions optimised with the spectral shape, even if the best position of the source is correctly evaluated by MLE. To overcome this problem we evaluated the best position and elliptical confidence region reducing the number of free parameters: all these sources are denoted with flag 5 (see Table 2).

4.1.2. Spectral models

We performed a full energy band spectral fit of the data to incorporate the constraint that the spectral shape should smoothly vary with energy. The 1AGL and 1AGLR catalogues considered only PL spectra; this was a simpler approach but not a good spectral representation for bright sources. With the exposure increasing, the discrepancies between PL and curved spectra could affect the global fit of the source, altering the spectra of nearby sources. Increasing the number of free parameters means that finding the true best fit is more difficult and, therefore, only spectra with one or two additional parameters were considered. The spectral representations used in the 2AGL catalogue are PL, exponential cut-off PL, super-exponential cut-off PL, and log parabola (LP).

The PL spectral model is used for all sources that are not significantly curved and have low exposure, i.e.

$$\frac{dN}{dE} = N_0 E^{-\alpha}, \quad (1)$$

where N_0 is the prefactor and α is the index explicitly evaluated by the MLE method. Our MLE spectral fitting does not explicitly output the prefactor value, which is internally calculated by the numerical procedure.

The majority of the 2AGL sources are described by a PL. With the exception of the brightest sources, the AGILE-GRID analysis may not be spectrally resolved because of low statistics. In this case the PL spectral model is assumed and in general, a fixed spectral index $\alpha = 2.1$ is adopted for the initial step of the MLE analysis. The exponential cut-off PL spectral model (PC) is

$$\frac{dN}{dE} = N_0 E^{-\alpha} \exp\left(-\frac{E}{E_c}\right), \quad (2)$$

where N_0 is the prefactor, α is the index, and E_c is the cut-off energy. The values E_c and α are explicitly provided by the MLE method. The super exponential cut-off PL spectral model (PS) is

$$\frac{dN}{dE} = N_0 E^{-\alpha} \exp\left(-\left(\frac{E}{E_c}\right)^{\beta}\right), \quad (3)$$

where N_0 is the prefactor, α is the first index, β the second index, and E_c is the cut-off energy. The parameters α, E_c, and β are explicitly provided by the MLE method.

The LP spectral model is

$$\frac{dN}{dE} = N_0 E^{-\alpha-\beta \ln(E/E_c)}, \quad (4)$$

where N_0 is the prefactor, E_c is the pivot energy, α is the first index, β the curvature. The parameters α, E_c, and β are explicitly provided by the MLE method.

In order to select the best spectral shape for every source, we performed a full spectral fit of the data with the spectral representations listed in this section. The MLE estimator does not converge with all spectral shapes: this can be due to poor statistics or to the presence of too many parameters in the spectral model. Another common problem is that, even if there is a fit convergence, the estimated parameters are too close to their limits or their errors are greater than the values of the parameters themselves: in these cases the fit is discarded. Our selection of curved spectra followed the acceptance criteria described in (Nolan et al. 2012). Briefly, a source is considered significantly curved if $TS_{\rm curved} > 16$, where $TS_{\rm curved} = 2 \times (\log L(curved\ spectrum) - \log L(power\ law)$, where L is the likelihood function obtained changing only the spectral representation of that source and refitting all free parameters.

4.1.3. Upper limit calculation

Upper limits were calculated using the same technique used for the asymmetrical errors for detected sources. We find the point-like source flux which maximises the likelihood.

The calculated upper limit is a conservative value guaranteed to be at or above the upper limit of the confidence interval. We calculated this upper limit using the following simple formula: $UL = \Delta F_+ + |F|$, where ΔF_+ is the positive error in the flux and $|F|$ is the absolute value of the flux. In the 2AGL catalogue we report the 2σ upper limits.

For very faint sources (in a single energy band or for the full energy band during the variability analysis) when $TS < 1$ we used a Bayesian method (Helene 1983). The upper limit is found by integrating the likelihood from 0 up to the flux that encompasses 95% of the posterior probability: in this way the upper limits calculated with both methods are similar for sources with $TS = 1$.

4.2. Binned sky maps preparation

In order to merge the data from different observing periods over the whole sky, we produced sets of sky maps in the ARC projection (Calabretta & Greisen 2002) in Galactic coordinates. Catalogued sources are detected by merging all the available data over the entire time period.

Different sets of counts and exposure maps were produced with the AGILE-GRID standard software package. We report a choice of parameters for maps generation of all sets, reporting in parenthesis the parameters values to be used in the software package distributed to AGILE guest observers.

To reduce the particle background contamination, only events tagged as confirmed γ-ray events were selected ($filtercode = 5$). The South Atlantic Anomaly data were excluded ($phasecode = 6$) and all γ-ray events whose reconstructed directions with respect to the satellite-Earth vector is smaller than 80° ($albrad = 80$) were also rejected to eliminate the Earth albedo contamination.

The considered energy range for the 2AGL source analysis is 100 MeV – 10 GeV. To reduce the uncertainty in the reconstruction of events, we selected only photons with a reconstructed direction within 50° from the boresight ($fovradmax = 50$).

4.3. Determination of seeds

The detection and localisation procedure is basically iterative, starting from a list of seeds. The seeds are the initial sky positions of the candidate point-like sources. The process starts without any set of input sources to avoid any kind of biases from different data sets.

We created a tiling of the sky called pixelisation. For each region of the sky, the initial set of candidate sources was determined using blind search techniques as a wavelet-based method ("wavelet algorithm") and generating significance maps (TS maps) iteratively. Each region was optimised independently. At the end of this step we obtained an independent list of seeds for each region of the sky.

Pixelisation. To create a tile of the sky with a sufficient resolution, we used 3072 circular regions (hereafter called rings) centred on points defined by HEALPix (Hierarchical Equal Area isoLatitude Pixelisation) (Górski et al. 2005) tessellation with $N_{\rm side} = 16$. We produced binned maps of 0.5° (used only for test) and 0.1° bin size with a side of 30° for each tile in Galactic coordinates, whose centres lay at constant latitude, with a unique energy bin of 100 MeV – 10 GeV. The tiles are discrete, overlapping, and not independent. The HEALPix algorithm produces a subdivision of a spherical surface in which each pixel covers the same surface area as every other pixel. We note, however, that we did not use the HEALPix projection but only a property of its grid; the pixel centres occur on a discrete number of rings of constant latitude to represent all-sky binned γ-ray data.

Wavelet algorithm. A continuous wavelet transform (CWT) was used to determine the first list of seeds. The CWT analyses a signal at different scales and is computed convolving the signal under investigation with the dilated and translated version of a wavelet function. When the support of the wavelet is small the CWT reacts mainly to high frequencies while, as the dilation increases, the wavelet support increases and the CWT is able to detect the lower frequency components of the signal (Louis et al. 1997). In this work we used the negative of the Laplacian of the Gaussian, called Marr or Mexican Hat wavelet, i.e.

$$\psi(x) = (2 - \|x\|^2) \exp\left(2 - \frac{\|x\|^2}{2}\right). \quad (5)$$

This wavelet has a positive kernel surrounded by a negative annulus. Its positive kernel has a Gaussian-like shape very similar to the AGILE-GRID PSF, hence it is effective in detecting point-like sources. It has a limited extent both in spatial and Fourier domains, which guarantees good localisation performance and limited aliasing effects (Freeman et al. 2002).

We used binned maps of $0.1° \times 0.1°$. The CWT of these maps consists of a 3D grid of pixels with the third dimension corresponding to the scales at which the transform is computed. We used a dyadic scale starting from one pixel up to the map size. The CWT at scales between 1 to 5 pixels provides evidence of point-like sources, some extended sources or clusters of sources are evident at scales between 5 and 10 pixels, while at higher scales the background is clearly identified.

The detection of sources is related to the probability of correctly classifying each pixel of the CWT as belonging to a source or to the cosmic background. The source detection threshold of each pixel is derived simulating several background sky maps and computing the CWT. In general, if a group of pixel is selected at any given scale then a similar group exists both at a finer and at a coarser scale. Each connected region of CWT pixels in a given range of scales can be considered as a putative source characterised by its centroid (spatial position) and scale extension. An example of 4 scales applied to the Cygnus region is shown in Fig. 4.

Iterative procedure on significance TS maps. The second list of seeds was determined to compute the significance TS map for each ring with an iterative procedure.

The first step starts without sources and, for each bin of the map, we performed a MLE, adding a point-like source in the ensemble of models at the centre of the bin under evaluation; the flux parameter was kept free, assuming a PL spectral index $\alpha = 2.1$. We used binned maps of $0.1° \times 0.1°$ and a radius of search of 5°. For each iteraction we may obtain a set of neighbouring bins with high significance. We selected a new candidate seed selecting the bin with the maximum TS value and only if $TS > 9$: the position of the seed is in the centre of the bin. This seed is added to the ensemble of models for the next iteration with the list of seeds identified in the previous steps. The seeds are kept with flux and position parameters fixed. The iterative procedure stops if no detection is found with $TS > 9$ or if the maximum allowed number of iterations is reached. At the end all seeds are merged, combining in one single seed the overlapping ones. Seeds close to the boundary of the circle of search in are removed, but the seeds can still survive because they are found in the neighbouring and overlapping rings with a position closest to the centre of the ring. An example of this iterative procedure on Cygnus region is shown in Fig. 5.

Final list of seeds. We added the list of seeds obtained from the iterative procedure on the significance TS to the list of seeds obtained with the wavelet technique. We checked the detections present only in the wavelet list with a manual analysis and added these to the final list if the detection has $\sqrt{TS} \geq 3$. The final list of seeds results in 912 candidate point-like sources.

4.4. Iterative analysis of seeds

The main purpose of this step is to reduce the number of seeds obtaining, at the end, a list of candidate sources for a refined analysis.

Pixelisation. We created a tiling of the sky for this step of analysis using 192 rings centred on points defined by HEALPix tessellation with $N_{\rm side} = 4$. We produced binned maps of 0.1° bin size with a side of 50° for each tile orientated with the north Galactic pole facing upward, whose centres are at a constant latitude with a single energy bin 100 MeV – 10 GeV. We used a lower number of rings for this step to reduce the border effects of the rings.

Iterative automated analysis of seeds. This stage starts from the list of seeds, ordered according to the estimated flux. For each iteration, an automated procedure selects one seed and the best ring for analysis, adding to the ensemble of models the seeds obtained with the previous iterations of this procedure and within 25° from the centre of the selected ring. The seeds within 5° from the selected seed under analysis are kept with flux free, and the seed under analysis is kept with position and flux free. The MLE method interactively optimises the position and flux of all the seeds of the region at the same time, with a radius of analysis of 10°. The localisation procedure of point-like sources provides the position, the 95% elliptical confidence region, and the best evaluation of the significance, using for all sources a PL spectral shape with $\alpha = 2.1$.

At the end of each iteration the flux and position of a single seed were optimised and the list of seeds was updated with the new flux and position if the detection has $TS > 9$, otherwise the seed was removed from the list. Since neighbouring regions are coupled, sharing data and sources, we repeated this step until the likelihoods were jointly optimised. With this procedure detections above $TS > 9$ significance are considered during the analysis.

4.5. Manual analysis

For the most complex and crowded regions of the sky, we performed additional manual analysis to add new candidate sources or to verify the results obtained with the previous step. We then updated the list of candidate 2AGL sources with new 16 candidate point-like sources obtained with this step. The final list of candidate 2AGL sources results in 318 candidate point-like sources with $TS > 9$.

4.6. Refined analysis

The main purpose of this step is to confirm candidate sources identified in the last step, obtaining the final list of 2AGL sources. The 2AGL catalogue includes sources above $TS > 16$ significance (corresponding to 4σ with one free parameter).

Pixelisation. We tiled the sky using a refined HEALPix tessellation used for the seeds with $N_{\rm side} = 16$, corresponding to 3072 pixel with a mean spacing of 3.6645°. We produced binned maps of $0.1° \times 0.1°$ bin size with a radius of 15° and with the following energy bins: 100 – 300, 300 – 1000, 1000 – 3000, 3000 – 10000 MeV. Additional bins of 30 – 50 and 50 – 100 MeV were produced by the same procedure.

Best position, spectral determination, and significance thresholding. We analysed the list of candidate sources obtained with the previous steps as follows:

1. This stage starts from the list of candidate sources, ordered according to the estimated flux.

2. Extraction of the first candidate source, keeping free all its parameters (flux, position, spectral shape parameters), keeping free the flux and fixed the position of the sources that are

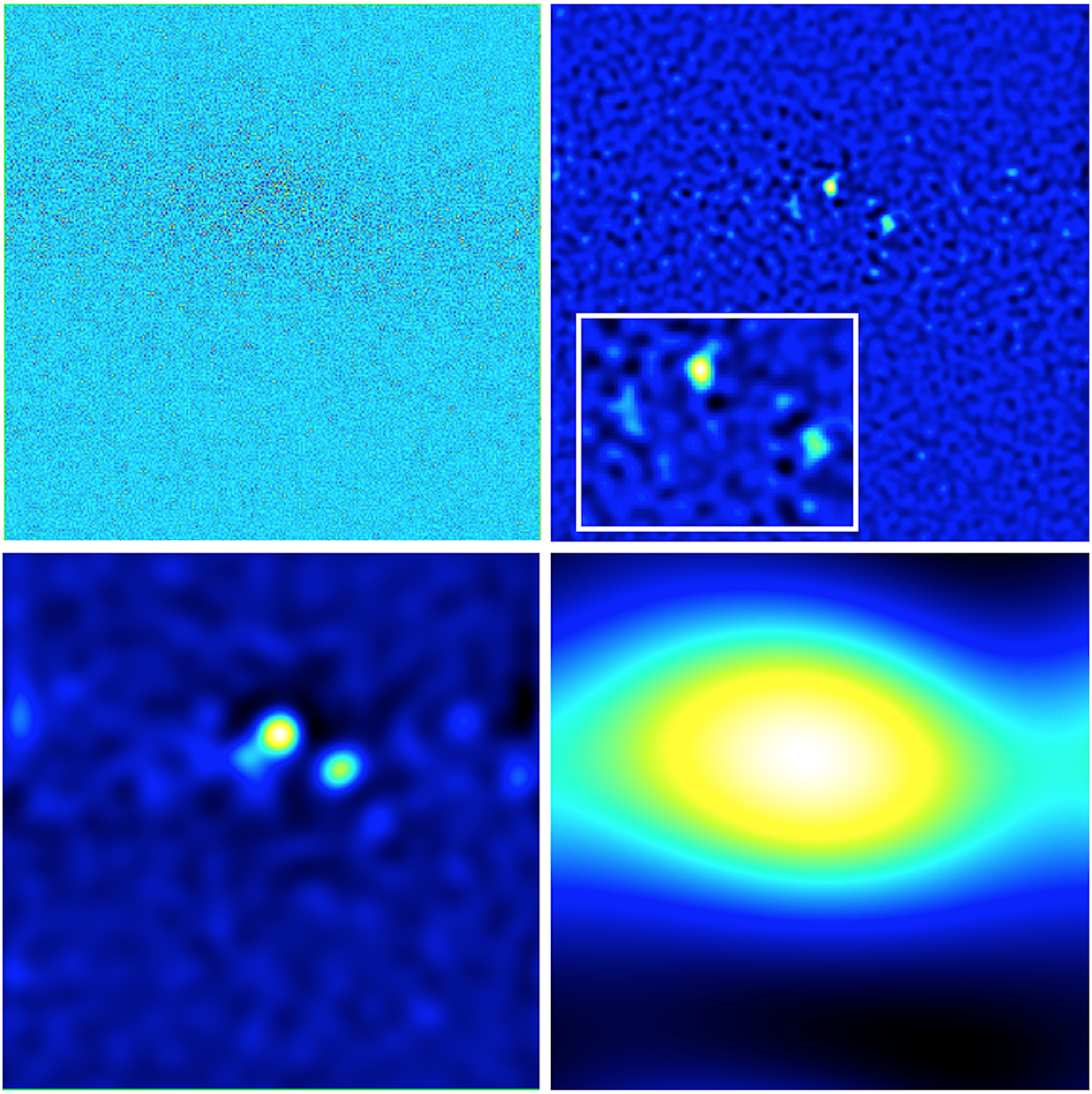

Fig. 4: Scales 10, 20, 25, and 35 of the wavelet algorithm applied on the Cygnus region from top to bottom and left to right. The maps of scale 20 (top, right) contains a zoom of the Cygnus region.

within 3° from the source under analysis, and fixing flux and position of the remaining sources within the sky map. The spectral shape is evaluated trying all available spectral models and selecting the best fit based on the $TS_{\rm curved}$. In some cases the PL index could result close to the boundaries: in this case, we fixed the index $\alpha = 2.1$. An analysis flag (see Sect. 5.4) is specified for this problem.

3. Update of the list of candidate sources with new position, flux, and spectral model. A final run with all parameters fixed except the flux was performed and a significance threshold $TS \geq 16$ was then applied for the final selection of candidate sources. We then restarted these steps with the next source on the list.

The source photon fluxes are reported in four energy bands: 100 – 300 MeV, 300 – 1000 MeV, 1 – 3 GeV, and 3 – 10 GeV. We performed a global fit over the full range, as described in Sect. 4.1.2. The fluxes in each band were obtained by freezing the spectral shape parameters to those obtained in the fit over the full range and adjusting the normalisation in each spectral band. If in any band $\sqrt{(TS)} < 3$, the upper limit was selected. Fig. 6 reports a comparison between the energy flux estimated in the energy range 100 MeV – 10 GeV from the sum of bands and that

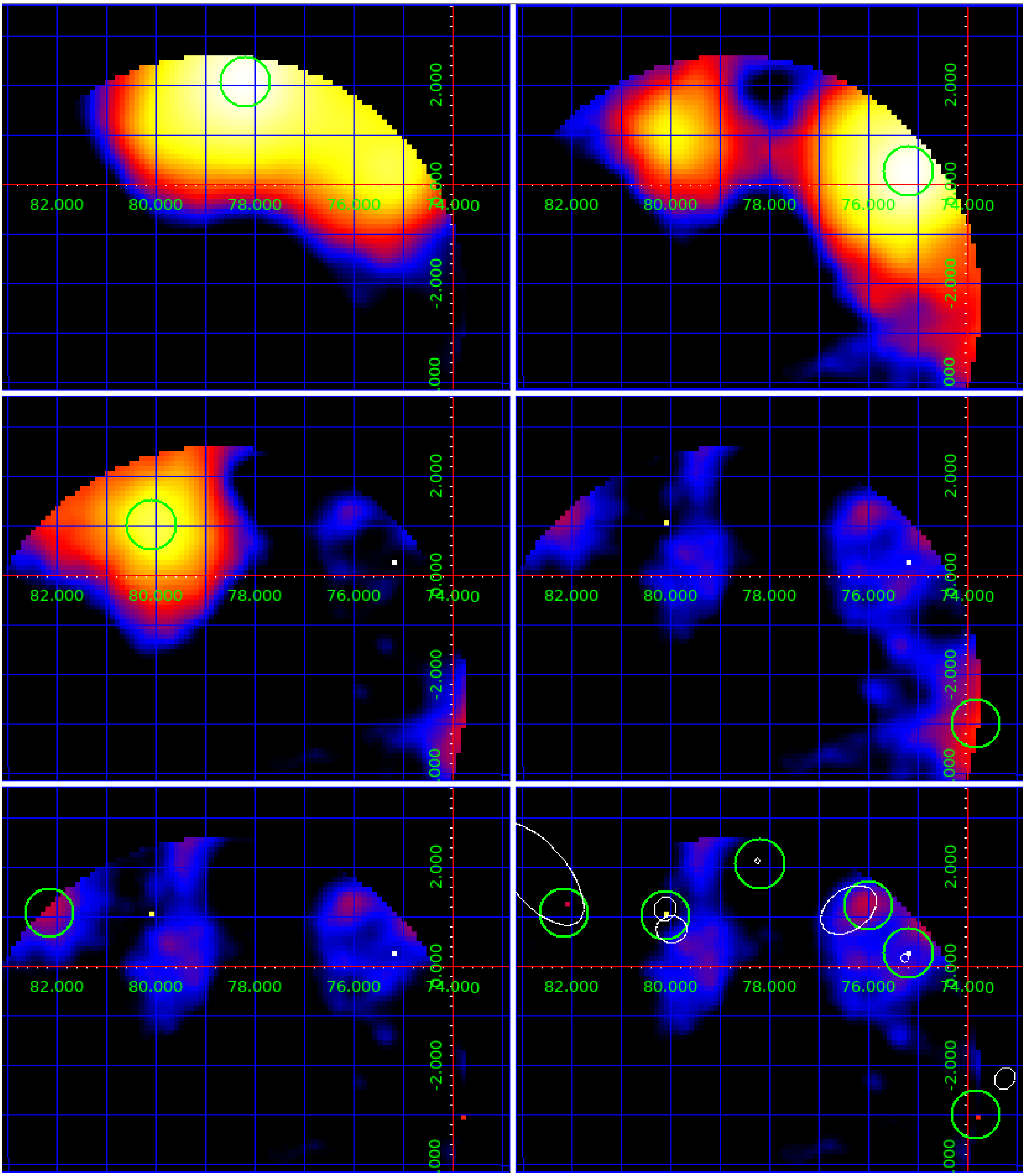

Fig. 5: First six steps of the iterative procedure on the significance TS maps described in Sect. 4.3 applied to the Cygnus region (panels from top to bottom and left to right). Green circles are centred on the pixels with the maximum TS found in each step. The last map (bottom right) contains all the green circles of the first six steps and the final 95% confidence region of the 2AGL sources. Even if border seeds are removed (see seeds found in panels 4 and 5), they are still present in the final version of the catalogue because they may be located in the overlapping nearby rings with a position closer to the centre, and sometimes the final position could slightly change (see seed found in panel 4).

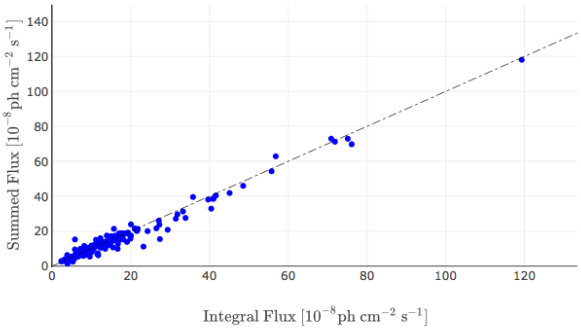

Fig. 6: Comparison of the energy flux in the energy range 100 MeV – 10 GeV estimated from the sum of bands (ordinate) and the fit to the full band (abscissa) for all 2AGL sources, in 10^{-8} ph cm^{-2}s^{-1}. No obvious bias can be observed.

estimated from the fit to the full range for all 2AGL sources. No obvious bias can be observed.

4.7. Residual TS significance maps.

The TS significance maps are used to compute the residual significance maps at the end of the analysis procedure to search for missing point-like sources. Each residual TS found in this way was evaluated with an additional step of the refined analysis. Five new sources were found and added, and neighbouring sources within a radius of 5° re-evaluated.

4.8. Variability

We performed a temporal variability analysis on the 2AGL catalogue sources. Temporal variability is common to different classes of γ-ray sources and it is important to determine a variability index. For each source we split the AGILE-GRID data in four-day time intervals: this is a compromise between the duration of an observation (see Table 1) and a useful exposure time. For each time interval we produced sky maps of 0.5° bin size and of 50° diameter, centred in the position of the source under analysis.

We produced a light curve for each source in the catalogue. Because of the already mentioned observation constraints of the pointing mode, the number of bins for each light curve could be different. To define a variability index, first we analysed each time bin keeping free only the flux of the source under analysis, adding the neighbouring 2AGL sources within the sky map. To avoid large error bars, the position and spectral parameters of the source were frozen, assuming spectral variability to be negligible; in addition we evaluated the diffuse γ-ray background emission and the isotropic background over the entire OB.

Let TS_1^i be the value of the TS obtained optimising the flux in each period of time i and TS_0 the value of TS estimated evaluating all the time bins at the same time but considering a constant flux, $TS_{\rm var}$ is described by the following relation:

$$TS_{\rm var} = \sum_{i=1}^{N} TS_1^i - TS_0. \quad (6)$$

If the null hypothesis is correct (the source has a constant flux) $TS_{\rm var}$ is distributed as χ^2 with N-1 degrees of freedom, and a value of $TS_{\rm var} > h(N-1)$ is used to identify variable sources at 99% confidence level, where $h(N)$ gives the threshold corresponding to a 99% confidence level in a χ^2 distribution with N degrees of freedom.

It is possible to introduce a corrective factor (similar to (Nolan et al. 2012)) to take into account the systematic error,

$$TS_i^{\rm corr} = F_{\sigma_i}^2/(F_{\sigma_i}^2 + f^2 * F_0^2). \quad (7)$$

The value F_{σ_i} is the error on the flux in each period of time i and F_0 is the flux estimated evaluating all the time bins at the same time but considering a constant flux. We consider $f = 0.02$ in our analysis (2% of systematic error). This value was found sufficient such that no AGILE-GRID pulsars are above threshold excluding the Crab, which has a highly variable nebular component at AGILE-GRID energies (Tavani et al. 2011; Abdo et al. 2011). The corrected $TS_{\rm var}$ is

$$TS_{\rm var}^* = \sum_{i=1}^{N} (TS_i^{\rm corr} * TS_1^i) - TS_0. \quad (8)$$

The variability index VI assumes the value 1 if $TS_{\rm var}^* > h(N-1)$. Upper limits calculated through the MLE method are handled by the procedure described above. In this procedure, all the upper limits are those obtained with the MLE method; no Bayesian procedure was used.

To be conservative, we evaluated the VI if $N > 12$. Some variable light curves (based on VI) are reported in Fig. 11 to Fig. 13.

4.9. Extended sources

The procedure described in the previous sections is related to point-like sources. We modelled a list of sources as spatially extended sources, using a 2D Gaussian model. Nearby point-like sources were fixed in position and spectral shape, keeping only the flux free for sources within 3° from the extended source under analysis and removing only sources inside the extended template that have no association with known point-like sources.

The list of analysed sources is reported in Table 3. The first column reports the region name, the second and third report the Galactic coordinates of the centre of the region, l_e and b_e, the fourth and the fifth report the two radii, r_1 and r_2, used for the analysis, which indicate the dispersion for 2D Gaussian sources. The value r_1 is chosen considering the observed extension at GeV and TeV energies (or considering a mean value if the shape of the extended region is not circular), r_2 is usually the double of r_1 with some exceptions (i.e. difference in radius between GeV and TeV energies or very eccentric shape). In particular, 3FGL (Acero et al. 2015) and TeVCat catalogues have been used for the selection of the two values. The online TeVCat catalog[4] is continuously updated with new sources detected by TeV experiments. At the time of writing (January 2019), the TeVCat catalogue contains a total of 219 TeV sources.

4.10. Exposure uniformity within the region of the MLE analysis

Owing to the non-homogeneous sky coverage of the AGILE observations during the first 2.3 years, it is possible that some can-

[4] http://tevcat.uchicago.edu/ (Wakely, S., and Horan, D.)

Table 2: Definitions of the analysis flags

Flag	Description
1	α fixed to 2.1
2	2 upper limits over 4 in the energy bands 100–300, 300–1000, 1000–3000, 3000–10000 MeV
3	3 upper limits over 4 in the energy bands 100–300, 300–1000, 1000–3000, 3000–10000 MeV
4	4 upper limits over 4 in the energy bands 100–300, 300–1000, 1000–3000, 3000–10000 MeV
5	Optimisation of position and spectral shape in two different steps

didate sources lie near the borders of certain pointings. In order to have an unbiased estimate of the coefficients of the Galactic diffuse emission and isotropic background that could lead to to an incorrect evaluation of the flux and position of the source, exposure uniformity within the region of the analysis is required.

We applied a specific check to verify the uniformity of the exposure within the 10-degree radius of the AGILE MLE analysis centred at each source candidate position, over the considered timescale. The fraction of pixels of the exposure map within the region of analysis having a value below a pre-defined threshold was calculated, and if it was more than 10% the region was considered unreliable and the candidate was discarded. The exposure threshold value is evaluated by calculating the mean exposure of the observation over the full FoV area and comparing this exposure with the values of some reference good exposures.

5. Limitations and systematic uncertainties

5.1. Instrument response functions systematic uncertainties

5.1.1. Systematic uncertainties on flux

In order to estimate systematic effects due to changes in instrument characteristics, inaccuracies in the IRFs, and uncertainties in the galactic diffuse model, we compared the behaviour of the residual for 100 MeV - 10 GeV near the peak of the Vela pulsar as a function of OBs (see Table 1). For each OB we constructed a model consisting of three components: the PSF at the position of Vela with the flux and super exponential cut-off PL spectral model listed in the 2AGL catalogue, an isotropic component of 5.9×10^{-5} ph cm^{-2}s^{-1}, and a galactic diffuse component with coefficient 0.5, evaluated during the 2AGL catalogue analysis. We then calculated the $residual = (model - counts)/exposure$ and the residual error $residual_{error} = \sqrt{2 \times model}/exposure$. We then binned the residual in annuli of 0.5° and observed the behaviour of the residual in the innermost ring as a function of OB. For most of the OBs the residual is consistent with a value slightly less than $1{\times}10^{-8}$ ph cm^{-2}s^{-1} but there is one OB, the OB 4100, where the residual is in the opposite direction and slightly higher. In any case the errors are very small compared to the statistical errors in the flux even for Vela, the brightest point source in the catalogue.

5.1.2. Systematic uncertainties on spectral index

In addition to the effect on the source flux the systematic uncertainties on the IRFs affect also the source spectral index. There are two relevant sources of systematic uncertainties: the shape of $A_{\rm eff}(E_\gamma)$ and the EDP. The former is shown in Fig.1 of Chen et al. (2013) and is obtained by simulation. Estimating the systematic errors from the simulation alone is unreliable, while in Cattaneo et al. (2018) the unreliability of the experimental estimation by the calibration under beam is discussed. An alternative approach is generating Monte Carlo spectra with a given shape of $A_{\rm eff}(E_\gamma)$ and index equal to -2.10, and fit the spectra with another shape. The most conservative choice is to use the $A_{\rm eff}(E_\gamma)$ from Chen et al. (2013) and fit assuming a flat $A_{\rm eff}(E_\gamma)$ and vice versa; that is much larger than any possible error and we can estimate covering a variation of the index of no less than $\pm 2\sigma_\alpha^{A_{\rm eff}}$. Out of 100 Monte Carlo experiments, the average index from the fit is -2.01 in the first case and -2.25 in the second. Therefore the systematic error can be estimated as $\sigma_\alpha^{A_{\rm eff}} = 0.24/4 = 0.06$.
The latter systematic uncertainty from EDP can be estimated analogously generating Monte Carlo spectra with EDP and fitting the index without and vice versa. That is a very conservative estimation because the calibration under beam Cattaneo et al. (2018) provides a measure of the EDP consistent with expectations and therefore any possible systematic error can be only a fraction of the EDP itself. Following the previous approach the systematic error due to EDP can be estimated as $\sigma_\alpha^{\rm EDP} = 0.07$.
Finally, the Monte Carlo spectra can be generated with $A_{\rm eff}(E_\gamma)$ and EDP and fitted without either and vice versa. The overall systematic errors is $\sigma_\alpha = 0.10$ consistent with the quadratic sum of the separate contributions.

5.2. Limitations on extended source analysis

There are some limitations in the analysis of extended regions that reduce the number of extended sources of the 2AGL catalogue. (i) Only a 2D Gaussian model is used as spatially extended sources model: this is not true for all extended shapes. (ii) Owing to limitations of the analysis tools, the analysis is performed with only a unique sky map integrated in the energy range 100 MeV – 10 GeV: this strongly limits the identification of extended sources for which the emission peaks at higher energies. (iii) Only the PL spectral model with a fixed spectral index $\alpha = 2.1$ is used.

5.3. Limitations of the variability index

The variability index VI is described in Sect. 4.8. The main limitation of this index is in the reduced number of temporal bins for each light curve, with a number of upper limits that is not negligible in many cases (even if the procedure handles this). The last limitation is that the variability index is not provided for light curves with less than 12 temporal bins. For these reasons, this index is not included in the identification criteria of counterparts.

5.4. Analysis flags

Some peculiar conditions that require caution to assess the confidence of a source are described in Table 2. Flag=1 indicates when, keeping the spectral index of the PL free, the value moves close to the boundaries of the search space of the spectral parameters. In this case a PL with fixed $\alpha = 2.1$ is assumed. This happens during step 2 of the refined analysis (Sect. 4.6). Only 4 sources have this flag.

Flags from 2 to 4 indicate that there are 2, 3, or 4 upper limits over four energy bins (100-300, 300-1000, 1000-3000, 3000-10000 MeV). The upper limits are usually in the highest energy bands. Sixty-one sources have flag=2, 51 sources have flag=3, and only 5 sources have flag=4.

Flag=5 indicates that AGILE Science Tools are not able to optimise the position and spectral shape parameters of the source at the same time during step 2 of the refined analysis; 33 sources have this flag.

6. Second AGILE-GRID γ-ray sources list

The second AGILE catalogue of γ-ray sources (2AGL) includes 175 high-confidence sources detected using the AGILE-GRID data during the pointing mode period; the methods and criteria are described in Sect. 4. An interactive web page of the 2AGL catalogue and its FITS file version are publicly available at SSDC[5].

In this section we present a description of the 2AGL catalogue, the criteria used for association and identification of sources with known counterparts, the content of the main tables, and a comparison with previous AGILE catalgues. Sect. 7 reports notes on individual 2AGL sources, where details used for associations and identifications are also described.

6.1. Catalogue description

The validated sources in the catalogue are listed in Table 10, including both confirmed and possible associations, and plotted in Fig. 7 in Galactic sky coordinates. Table 4 reports the description of the columns of Table 10.

The source designation is *2AGL JHHMM+DDMM[c/e]* where the *2* indicates that this is the second AGILE-GRID catalogue, *AGL* represents the AGILE-GRID. The name of the sources potentially confused with the Galactic diffuse emission or with a large uncertainty on its location is appended with *c*, and caution should be used in interpreting these sources; an appended *e* indicates sources associated with a spatially extended emission.

It is important to note that each source is observed for a different number of days, much smaller than the 2.3 years of the pointing mode. The column 'Exp' of Table 10 reports a rough estimate of days of observations, obtained dividing exposure by a mean $A_{\rm eff} = 300$ cm^2 and 86400 seconds. Association and identification of 2AGL sources are described in Sect. 6.2.

Figure 8 reports some distributions of 2AGL source parameters (spectral indexes, fluxes, 95% elliptical confidence regions, parameters distributions, and distances from known counterparts). The most important classes of the 2AGL catalogue are AGNs and pulsars. The median value of the spectral index for AGN classes is $\alpha = 2.10 \pm 0.30$, and for pulsar class is $\alpha = 1.98 \pm 0.30$; the two distributions are compatible. The distributions of distances of 2AGL from 3FGL counterparts for the two different classes are shown in the bottom figures together with fits to the Rayleigh function. This fit assumes implicitly that the errors on the source positions are constant. In reality we expect that the position error on each source depends on the statistical and systematic errors of AGILE-GRID and FERMI-LAT, which vary from source to source, and therefore that a single Rayleigh function is not fully adequate. Nevertheless the values of χ^2/ndf close to one demonstrate that, under the simplified assumption of constant errors, the two distributions are consistent.

[5] https://www.ssdc.asi.it/agile2agl

6.2. Source association and identification

In the 2AGL catalogue we define three different classes of identified, associated, and unidentified sources. Table 5 reports a summary of the 2AGL classes. Designations shown in capital letters are firm identifications; lower case letters indicate associations. Fig. 9 reports a full sky map showing sources labelled by source class. A blow-up of the inner Galactic region is reported in the bottom of Fig. 9.

Associations are defined using a spatial cross-correlations procedure based on spatial coincidence of the 95% confidence region with various updated public catalogues of specific mission or of specific source classes known to be potential γ-ray emitters. The list of catalogues used for association is reported in Table 6. Two sources are considered associated if there is a partial or total overlapping between the 95% elliptical confidence regions, taking into account the statistical error plus a systematic error of 0.1° (Chen et al. 2013).

We used different criteria to establish a firm identification of a 2AGL source with a known counterpart.

AGN of the blazar type dominate the extragalactic γ-ray sky and are known to be highly variable in γ-rays, not always showing simultaneous correlated variability at other wavelengths. So positional consistency plus γ-ray variability were used for the identification of 2AGL sources with AGN counterparts. Identification with AGNs is established if at least one flaring episode with a significance $> 4\sigma$ and with a peak flux at least three times the average flux is found on a four-day timescale in the energy range 100 MeV – 10 GeV, or at OB level (the full list of OBs is reported in Table 1). Target of opportunity observations on the source could strongly influence the average flux; in that case, only detections with a significance $> 4\sigma$ are considered. The light curves are determined with the flux and position parameters allowed to vary, where the position of the 2AGL source is used as the starting position. Section 7.1 reports a discussion about the association or identification of some AGNs.

We introduce the special subclass of 'AGILE-only' sources, i.e. unidentified source that are only present in this γ-ray catalogue but not positionally consistent with sources in 1FGL, 2FGL, or 3FGL catalogsue; details are reported in Sect. 7.2.

The 'γ-ray unidentified' sources are a subclass of sources detected in γ-ray by the AGILE-GRID and the Fermi-LAT but that are unidentified in other wavelengths; details are reported in Sect. 7.3.

Regarding candidate AGN sources, 'AGILE-only' sources, and 'γ-ray unidentified' sources, are also identified with the VOU-BLAZAR tool (hereafter VOUblaz) specifically designed to identify blazar sources based on a multi-frequency study in large error regions, and through time resolved spectral energy distribution (SED) creation and analysis. This tool is developed within the Italian Space Agency (ASI) web portal for the "Open Universe" initiative[6] (Giommi et al. 2018; Padovani et al. 2018), an initiative under the auspices of the United Nations Committee On the Peaceful Uses of Outer Space (COPUOS). The

[6] http://www.openuniverse.asi.it/

Table 3: List of extended sources analysed for 2AGL catalogue.

Region name	l_e	b_e	r_1	r_2	Region name	l_e	b_e	r_1	r_2
Boomerang	106.57	2.91	1.00	2.00	HESS J1834-087	23.24	-0.33	0.09	0.18
CTA1	119.60	10.40	0.30	0.60	HESS J1837-069 (PWN)	25.18	-0.12	0.12	0.33
CTB37A	348.38	0.10	0.07	0.14	HESS J1841-055 (PWN)	25.87	-0.36	0.40	0.62
CTB37B	348.63	0.38	0.06	0.12	HESS J1843-033	29.03	0.36	1.00	2.00
CenA Lobes	309.17	18.98	1.25	2.50	HESS J1848-018	31.00	-0.17	0.32	0.64
Cygnus Cocoon	80.95	1.80	1.80	3.00	HESS J1857+026	36.00	-0.07	0.20	0.40
Cygnus Loop	73.98	-8.56	3.00	10.00	HESS J1858+020	35.57	-0.59	0.08	0.16
G106.3+2.7	106.34	2.71	0.27	0.52	HESS J1912+101	44.39	-0.08	0.27	0.52
G327.1-1.1	327.15	-1.08	0.03	0.06	IC 443	189.07	2.92	0.16	0.27
Galactic Center Ridge	359.94	-0.05	2.00	4.00	IGR J18490-0000	32.63	0.52	1.00	2.00
Geminga	195.33	3.77	1.30	2.60	Kookaburra-Pulsar	313.55	0.26	0.06	0.11
HB 21	88.75	4.67	0.59	1.19	Kookaburra-Rabbit	313.24	0.14	0.08	0.16
HESS J1018-589B	284.11	-1.90	0.15	0.30	LMC	279.55	-31.75	0.14	1.87
HESS J1026-582	284.79	-0.53	0.14	0.28	MGRO J1908+06	40.28	-0.69	0.44	0.88
HESS J1303-631 (PWN)	304.21	-0.33	0.19	0.24	MGRO J2019+37	74.82	0.41	0.75	1.50
HESS J1356-645	309.81	-2.50	0.20	0.40	MGRO J2031+41	79.53	0.63	1.80	3.60
HESS J1427-608	314.40	-0.15	0.04	0.08	MSH 15-52	320.33	-1.19	0.11	0.25
HESS J1457-593	318.36	-0.44	0.31	0.62	Puppis A	260.32	-3.28	0.16	0.37
HESS J1458-608	317.74	-1.71	0.17	0.34	RCW 86	315.41	-2.31	0.41	0.82
HESS J1503-582	319.61	0.29	0.26	0.52	RX J1713.7-3946	347.34	-0.47	0.56	0.65
HESS J1507-622	317.94	-3.50	0.15	0.30	S 147	180.24	-1.50	0.75	1.50
HESS J1614-518	331.52	-0.58	0.23	0.42	SMC	302.14	-44.42	0.67	1.35
HESS J1616-508 (PWN)	332.39	-0.14	0.18	0.32	SN 1006-NE	327.84	14.56	0.12	0.24
HESS J1626-490	334.77	0.04	0.10	0.20	SN 1006-SW	327.86	15.34	0.13	0.26
HESS J1632-478 (PWN)	336.38	0.19	0.21	0.35	SNR G292.2-00.5	292.10	-0.49	0.10	0.20
HESS J1634-472	337.10	0.21	0.11	0.22	TeVJ2032+4130	80.24	1.17	0.16	0.32
HESS J1640-465	338.31	-0.03	0.01	0.04	Terzan 5	3.78	1.72	0.16	0.32
HESS J1702-420	344.30	-0.19	0.30	0.60	VELA Jr	266.28	-1.24	1.00	1.12
HESS J1708-410	345.68	-0.48	0.08	0.16	VELAPS	263.58	-2.84	0.10	
HESS J1708-443	343.05	-2.38	0.29	0.60	VELAX	263.86	-3.09	0.48	0.91
HESS J1718-385	348.83	-0.49	0.15	0.30	VER J2019+368	75.04	0.28	0.34	0.68
HESS J1729-345	353.44	-0.13	0.12	0.24	VER J2019+407	78.33	2.49	0.23	0.46
HESS J1731-347	353.54	-0.68	0.27	0.34	W28-HESS J1800-240ABC	5.96	-0.39	0.32	0.64
HESS J1745-303	358.70	-0.65	0.21	0.42	W44	34.65	-0.39	0.15	0.30
HESS J1804-216	8.35	-0.01	0.27	0.35	W30	8.40	-0.03	0.27	0.37
HESS J1808-204	9.95	-0.25	0.14	0.28	W51C	49.12	-0.36	0.12	0.38
HESS J1809-193	11.18	-0.09	0.53	1.06	Westerlund 1	339.54	-0.36	1.10	2.20
HESS J1825-137	17.71	-0.70	0.13	0.16	Westerlund 2	284.21	-0.41	0.18	0.36
HESS J1813-178	12.81	-0.03	0.04	0.08	gammaCygni	78.33	2.49	0.23	0.63
HESS J1831-098	21.85	-0.11	0.15	0.30					

The first column reports the region name, the second and third columns report the Galactic coordinates of the centre of the region, the fourth and the fifth columns report the two radii, r_1 and r_2, used for the analysis indicating the dispersion for 2D Gaussian sources.

multiwavelength information used by the VOUblaz tool, both in the phase of the identification of blazar candidates and for the construction of the SED of a given candidate, is generally non-simultaneous as it is obtained through VO queries to a large number (> 50) of catalogues and archival spectral data. A blazar found within the error region is considered as a viable counterpart of an AGILE source when the ratio of the low- to high-energy humps (Compton dominance) is well within the range observed in previous γ-ray catalogues. Details of the analysis with this tool are reported in the discussion of each source.

Pulsars are firmly identified if pulsation is found in the AGILE-GRID data; details are reported in Sect. 7.4.

As a general rule for all classes, for "firmly identified" counterparts we have included γ-ray sources for which there are peer reviewed publications demonstrating high-confidence associations with refined analysis methods. In the SNR class we have IC 443, W28, W44, and Gamma Cygni (Sect. 7.8 for more details), Crab nebula as pulsars wind nebula (PWN; Sect. 7.7 for more details), and Cygnus X-3 as an HMXB (Sect. 7.9 for more details). Also some AGNs have been identified in this way.

6.3. Extended sources

We report in Table 7 some details for 2AGL sources that are also classified as extended γ-ray emission; they are denoted with an 'e' appended to the 2AGL name. We note that there could be a difference in positioning of the same source if evaluated as extended (as reported in Table 7) or point-like (as reported in Table 10).

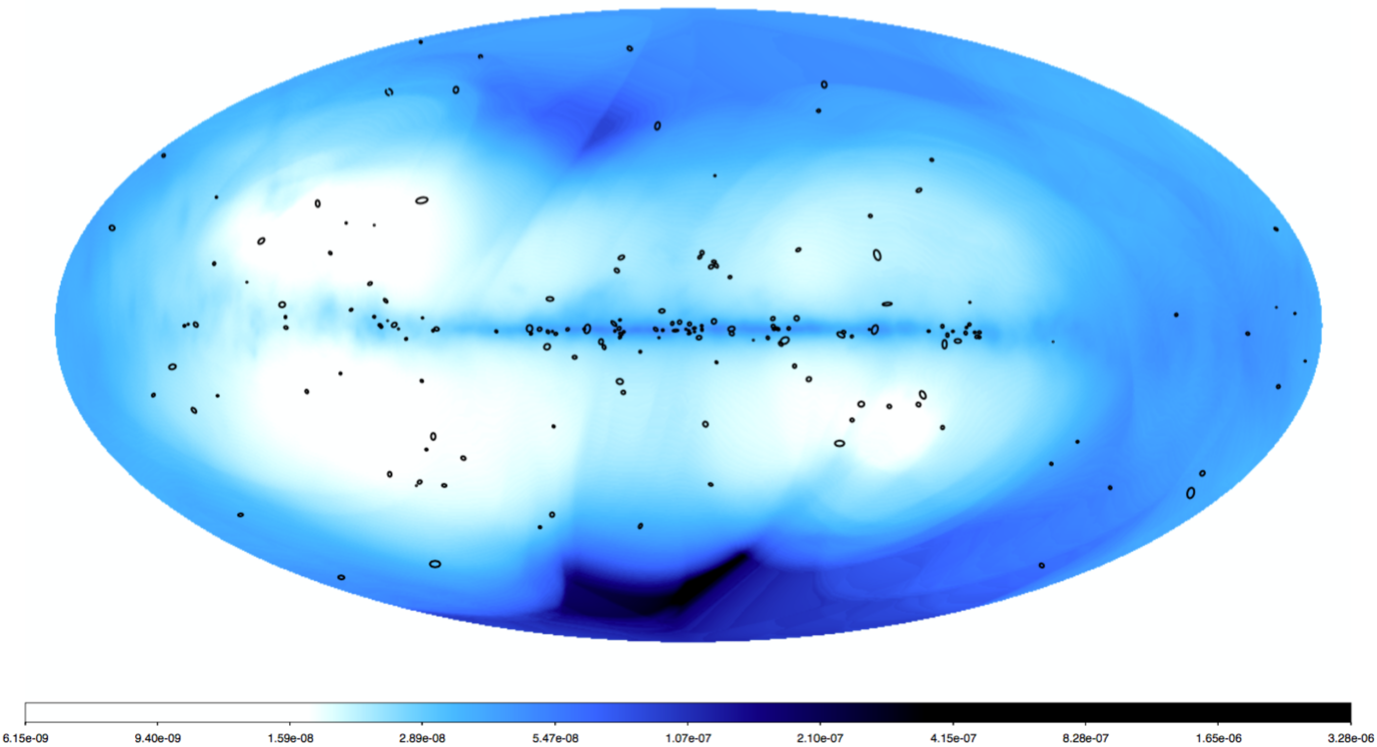

Fig. 7: Sky map of 4σ sensitivity in the energy range 100 MeV – 10 GeV in Galactic coordinates and Hammer-Aitoff projection; the hypothesis of a PL spectral model with $\alpha = 2.1$, in ph cm^{-2}s^{-1}. The 95% elliptical confidence regions of the 2AGL sources are superimposed in black.

6.4. Spectral models

Each source is analysed fitting the data with the four spectral models described in Sect. 4.1.2. The final selection is based on the $TS_{\rm curved}$ criteria described in the same section. The 2AGL sources with curved spectra are listed in Table 8. Table 9 reports a description of the columns of Table 11, which presents the fluxes in individual bands as defined in Sect. 4.6.

6.5. Comparison with the AGILE Astronomer's Telegrams

The list of Astronomer's Telegrams in pointing mode, obtained during the γ-ray flare monitoring programme (see Sect. 2.4) and associated with 2AGL source are reported in Table 12.

6.6. Comparison with 1AGL and 1AGLR catalogues

Three of the 47 1AGL catalogue sources are not present in the 2AGL catalogue: 1AGL J1222+2851, 1AGL J1238+0406, and 1AGL J1815-1732. We note that 1AGL J1222+2851 is associated with WComae (ON+231) (with an associated Astronomer's Telegram; see Table 12) but due to the longer integration time of the 2AGL catalogue this source goes below the significance threshold.

Four of the 54 1AGLR catalogue sources are not present in the 2AGL catalogue: 1AGL J1238+0406, 1AGLR J1807-2103, 1AGLR J2016+3644, and 1AGLR J2030-0617. These differences are mainly due to a different integration time or to splitting a 1AGL/1AGLR sources in different 2AGL sources.

6.7. Comparison with AGILE TeVCat

Thirteen of the 52 sources of the AGILE TeVCat (Rappoldi et al. 2016) are not present in the 2AGL catalogue. These sources are not confirmed due to a different analysis procedure, different Science Tools, different background cuts ($albrad = 85$, $fovradmax = 60$) and improved IRFs, or to splitting the source in different 2AGL sources. The AGILE TeVCat sources not present in the 2AGL catalogue are: (1) TeVJ0232+202, associated with 1ES 0229+200, below the 2AGL catalogue threshold, (2) TeVJ0521+211 (VER J0521+211), (3) TeVJ0835-455 (Vela X), (4) TeVJ0852-463 (RX J0852.0-4622), (5) TeVJ1729-345 (HESS J1729-345), (6) TeVJ1732-347 (HESS J1731-347), (7) TeVJ1745-303 (HESS J1745-303), (8) TeVJ1813-178 (HESS J1813-178), (9) TeVJ1825-137 (HESS J1825-137), (10) TeVJ1841-055 (HESS J1841-055), (11) TeVJ1912+101 (HESS J1912+101), (12) TeVJ2323+588 (Cassiopeia A), (13) TeVJ2359-306 (HESS J2359-306).

7. Notes on individual sources

In this section we comment on some specific 2AGL sources, divided by classes or sky regions, including AGILE-GRID identifications or associations for individual sources based on criteria described in Section 6.2.

Sect. 7.1 reports a description of associated or identified AGNs, Sect. 7.2 on AGILE-only sources, Sect. 7.3 on γ-ray only sources, Sect. 7.4 on pulsars, Sect. 7.5 reports a discussion on the Cygnus region, Sect. 7.6 on the Carina region, Sect. 7.7 on PWNs, Sect. 7.8 on SNRs, Sect. 7.9 on binaries, and Sect. 7.10 on confused sources.

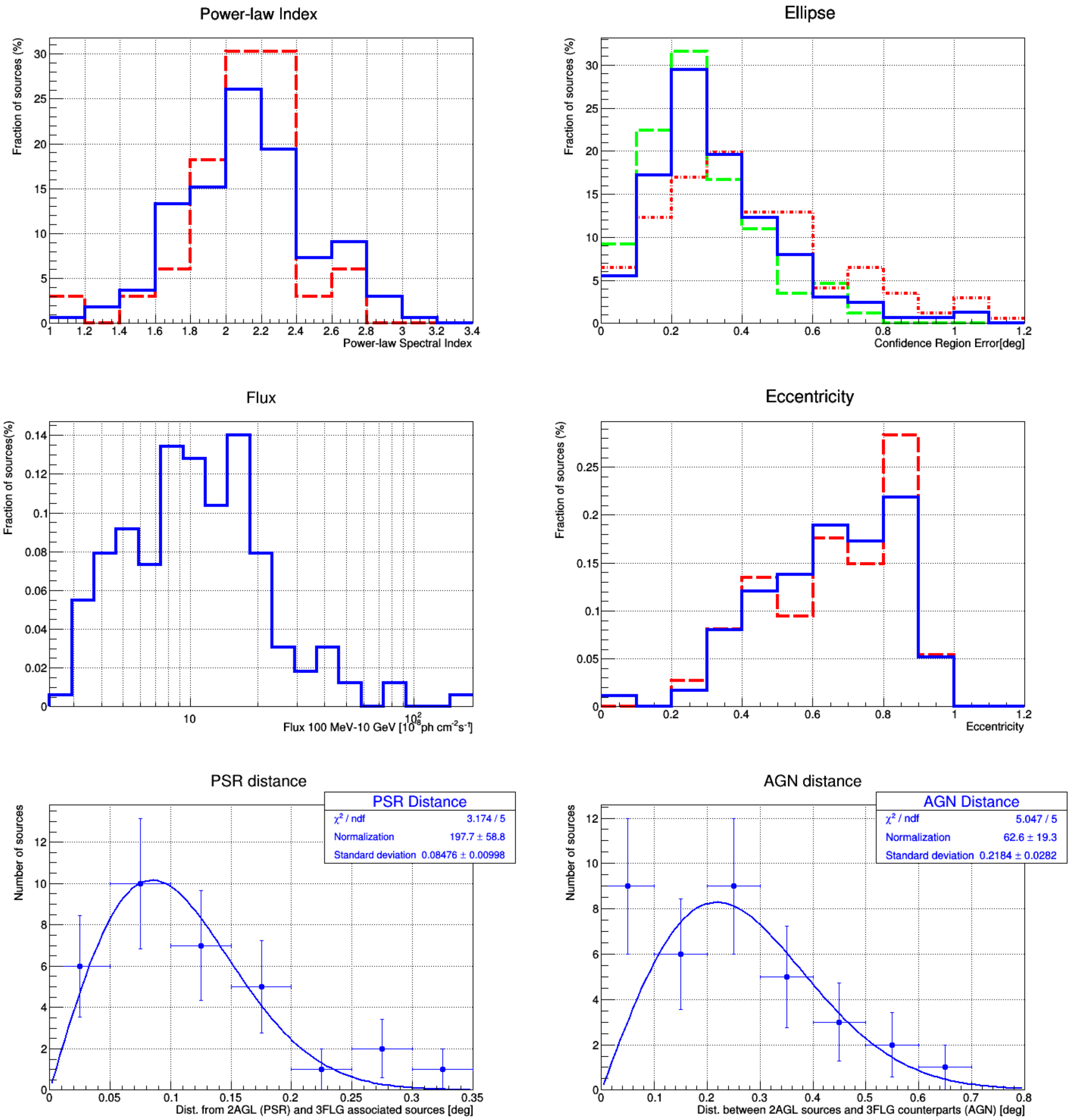

Fig. 8: Some distributions of 2AGL source parameters. Top left figure shows the spectral index distributions for sources with PL spectral model, all sources (blue), and only for sources with high latitude ($|b| > 10$) (red). The top right figure shows the 95% confidence region error radius (blue), the semi-major axes of 95% elliptical confidence region (red), and the semi-minor axes (green). The middle left figure shows the integral flux in the energy range 100 MeV – 10 GeV, for sources with PL spectral model. The middle right figure shows the eccentricity of the 95% elliptical confidence region for all sources (blue) and for high latitude sources ($|b| > 10$) (red). The bottom left figure shows the distance between the 2AGL sources classified as pulsars and their 3FGL counterparts for sources with $\sqrt{TS} \geq 5$. The bottom right figure shows the distance between 2AGL sources classified as AGN and their 3FGL counterparts, for sources with $\sqrt{TS} \geq 5$. In the latter two figures the data are fit with a Rayleigh function.

Table 4: AGILE-GRID second catalogue column descriptions of Table 10, Table 13, and Table 14

Column	Units	Description
Name		2AGL JHHMM+DDMM[c/e] constructed according to IAU Specifications for Nomenclature; in the name, R.A. and Decl. are truncated at 0.1′ and 1′, respectively; 'c' indicates that based on the region of the sky the source is potentially confused with Galactic diffuse emission; 'e' indicates a source modelled as spatially extended
R.A.	deg	Right Ascension, J2000
Dec.	deg	Declination, J2000
l	deg	Galactic Longitude
b	deg	Galactic Latitude
r	deg	Radius of 95% c.l. circular confidence region, deg. Statistical error only
θ_a	deg	Semi-major axis of 95% c.l. elliptical confidence region, deg. Statistical error only
θ_b	deg	Semi-minor axis of 95% c.l. elliptical confidence region, deg. Statistical error only
ϕ	deg	Position angle of 95% confidence region, clockwise
SM		Spectral model. PL indicates power-law fit to the energy spectrum; PC indicates power-law with exponential cut-off fit to the energy spectrum; PS indicates power-law with super exponential cut-off fit to the energy spectrum; LP indicates log-parabola fit to the energy spectrum
$\sqrt{TS}$		Significance derived from likelihood test statistic in the energy range 100 MeV – 10 GeV
α		Spectral index for PL, PC, and PS spectral models, first index for LP spectral model, in the energy range 100 MeV – 10 GeV; see Sect. 4.1.2 for the definition of α
$\Delta\alpha$		Statistical 1σ uncertainty of α, in the energy range 100 MeV – 10 GeV
F_γ	10^{-8} ph cm^{-2}s^{-1}	Photon flux in the energy range 100 MeV – 10 GeV, summed over 4 bands, for the pointing mode period
δF_γ	10^{-8} ph cm^{-2}s^{-1}	Statistical 1σ uncertainty of F_γ
F_e	10^{-9} erg cm^{-2}s^{-1}	Integrated energy flux in the energy range 100 MeV – 10 GeV, for the pointing mode period
δF_e	10^{-9} erg cm^{-2}s^{-1}	Statistical 1σ uncertainty of F_e
VI		Variability index equal to 1 indicates < 1% chance of being a steady source. No value indicates that there are not enough 4-day time periods to calculate the index. See Sect. 4.8 for more details.
Exp	cm^{2}Ms [days]	Exposure in cm^{2}Ms and days. Days are obtained dividing exposure by the mean $A_{\rm eff}$ = 300 cm^2 and 86400 s
Flag		Flag (see Table 2)
AGL assoc.		Positional associations with sources from AGILE catalogues listed in Table 6. For AGILE-TeVCat we added the AGL prefix to the catalogue name
γ-ray assoc.		Positional associations with sources not from AGILE catalogues listed in Table 6. For the same source in the FGL catalogues, we kept the association with the last FGL catalogue
ID or assoc.		Designator of identified or associated source. A * indicates a possible marginal positional association
Class		Class (see Table 5)

7.1. Notes on AGN sources

In the following we report identifications or associations for AGNs. In particular, we report the flaring episodes detected with our variability analysis used to establish an identification between the 2AGL source and a known counterpart, and/or the reference to multiwavelength (MW) information obtained by the use of the VOUblaz tool demonstrating high-confidence identifications.

2AGL J0135+4754 Integrating in the time interval MJD 55037.5-55041.5, a MLE analysis yields a detection of 4.6σ and a flux $F = (55 \pm 17) \times 10^{-8}$ph cm^{-2}s^{-1}, establishing a firm identification of 2AGL J0135+4754 source with OC 457.

2AGL J0252+5038 Integrating in the time interval MJD 54813.5-54817.5 a MLE analysis yields a detection of 4.0σ and a flux $F = (70 \pm 21) \times 10^{-8}$ph cm^{-2}s^{-1}, positionally consistent with the flat spectrum radio quasar (FSRQ) NVSS J025357+510256, establishing a firm identification with 2AGL J0252+5038.

2AGL J0221+4250 The 95% elliptical confidence region contains two sources, i.e. 3C 66A and PSR J0218+4232, but the variability analysis excludes the PSR. Integrating in the OB 5820 (MJD 54632.5-54647.5), a MLE analysis yields a detection of 4.3σ and a flux $F = (32 \pm 8) \times 10^{-8}$ph cm^{-2}s^{-1}. The best detection in the OB 5820 is in the time interval MJD 54641.5-54645.5, with a detection of 4.0σ and a flux $F(E > 100\,\mathrm{MeV}) = (50 \pm 15) \times 10^{-8}$ph cm^{-2}s^{-1}, with a statistical 95% c.l. elliptical confidence region that includes only 3C 66A, establishing a firm identification of 2AGL J0221+4250 source with this BLL.

2AGL J0429-3755. Integrating in the time interval MJD 54497.5-54501.5 MJD, a MLE analysis yields a detection of 4.9σ and a flux $F = (50 \pm 15) \times 10^{-8}$ph cm^{-2}s^{-1}, positionally consistent with the BLL PKS 0426-380, establishing a firm identification with 2AGL J0429-3755 source.

2AGL J0531+1334. A low level significance 2AGL source with a positional association with the FSRQ PKS 0528+134, which could be promoted to firm identification via the VOUblaz tool thanks to MW information.

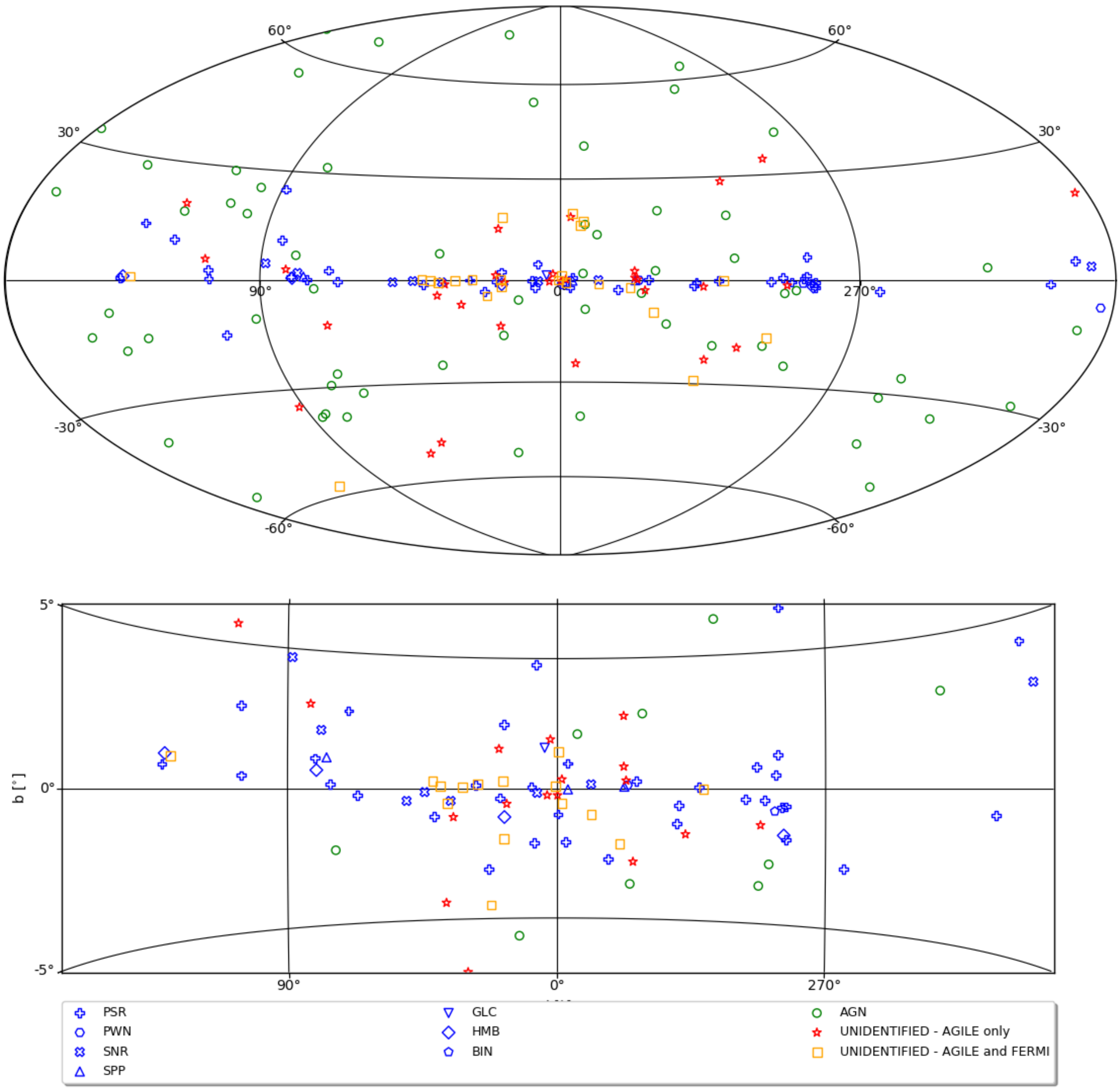

Fig. 9: Positions, in Galactic coordinates, of the 2AGL sources labelled by different symbols according to their class for the full sky (top) and a blow-up of the inner Galactic region (bottom). All AGN classes are plotted with the same symbol.

2AGL J0538-4401. Integrating in the OB 6210 (MJD 54749.5-54756.5), a MLE analysis yields a detection of 5.4σ and a mean flux $F = (35 \pm 9) \times 10^{-8}$ph cm^{-2}s^{-1}, positionally consistent with PKS 0537-441, establishing a firm identification of this AGN with 2AGL J0538-4401 source. The source PKS 0537-441 has an high average flux value in the 2AGL catalogue because it has mainly been observed in a ToO pointing during a flaring state.

2AGL J0723+7122. The 2AGL J0723+7122 source is firmly identified with BLL S5 0716+714. The highest detection of 2AGL J0723+7122 with a time resolution of four days is during the time interval MJD 54349.5-54353.5: an MLE analysis yields a detection of 6σ and a flux $F(E > 100$ MeV$) = (70 \pm 17) \times 10^{-8}$ph cm^{-2}s^{-1}. Additional observations are reported in (Giommi et al. 2008; Chen et al. 2008; Vittorini at al. 2009). In particular Chen et al. (2008) report a peak level of $F(E > 100$ MeV$) = (193 \pm 42) \times 10^{-8}$ph cm^{-2}s^{-1} in MJD 54353.5-54354.5 (one-day timescale), and show an increase in flux by a factor of four in three days. An astronomer's telegrams (ATEL) is reported for this source (see Table 12) during the pointing mode.

2AGL J1052-6234. We detect a flare during the time interval MJD 54649.5-54653.5: a MLE analysis yields a detection of 4σ and a flux $F = (40 \pm 12) \times 10^{-8}$ph cm^{-2}s^{-1}, identifying the PMN J1047-6217 (that is inside the 95% c.l. elliptical confidence region) with the 2AGL J1052-6234 source.

2AGL J1228+4910. The 2AGL J1228+4910 is identified with FSRQ TXS 1226+492 (also known as BZQ J1228+4858) because it shows a γ-ray flare during the period 54461.5-54465.5: an MLE analysis yields a detection of 4.0σ and a flux

Table 5: 2AGL source classes.

Description	Identified		Associated	
	Designator	Number	Designator	Number
Pulsars, identified by pulsations	PSR	7	...	...
Pulsars, no pulsations seen yet	...	...	psr	34
Pulsars wind nebula	PWN	1	pwn	1
Supernova remnants	SNR	4	snr	4
Supernova remnants / Pulsars wind nebula	...	...	spp	3
Globular clusters	GLC	0	glc	1
High-mass X-ray binaries	HMXB	1	hmxb	3
Binaries	BIN	0	bin	1
BL Lac type of blazars	BLL	6	bll	13
FSRQ type of blazars	FSRQ	15	fsrq	18
Radio galaxies	RDG	0	rdg	2
Blazars candidate of uncertain type	BCU	2	bcu	6
Total	...	36	...	85
Unidentified	...	...	unid	31
Gamma Unidentified	...	...	gunid	22
Total Sources	...	...	...	175
Total AGILE only sources	...	...	...	29

Designations shown in capital letters are firm identifications; lower case letters indicate associations. The designation spp indicates potential association with SNR or PWN.

$F = (103 \pm 37) \times 10^{-8}$ph cm^{-2}s^{-1}. In addition, during the OB 6710 (MJD 54850.75-54890.5) an MLE analysis yields a detection of 4.6σ and a mean flux $F = (89 \pm 23) \times 10^{-8}$ph cm^{-2}s^{-1}.

2AGL J1228+0154. The 2AGL J1228+0154 source is identified with FSRQ 3C 273; γ-ray activity is reported in Pacciani et al. (2009).

2AGL J1255-0543. The 2AGL J1255-0543 source is identified with FSRQ 3C 279 (Giuliani et al. 2009; Pittori et al. 2018). In the automated analysis we detect 2AGL J1255-0543 during the time interval OB 5010 (MJD 54450.5-54473.5): an MLE analysis yields a detection of 4.9σ and a flux $F = (26 \pm 6) \times 10^{-8}$ph cm^{-2}s^{-1}. The γ-ray emission exhibited the largest amplitude variability on both long (months) and short (days) timescales. The source 3C 279 has a high average flux value in the 2AGL catalogue because it has been mainly observed in ToO pointings during flaring states.

2AGL J1507+1019. This source is identified with PKS 1502+106. We detect 2AGL J1507+1019 during the OB 6800 (MJD 54890.5-54921.5): an MLE analysis yields a detection of 6.1σ and a flux $F = (60 \pm 12) \times 10^{-8}$ph cm^{-2}s^{-1}.

2AGL J1513-0905. The 2AGL J1513-0905 is identified with PKS 1510-089. This FSRQ shows a strong variability during the AGILE pointing mode (Pucella at al. 2008; D'Ammando et al. 2009, 2011a,b). The 2AGL catalogue light curve is reported in Fig. 11. Many ATELs are reported for this source (see Table 12).

2AGL J1626-2943. The 2AGL J1626-2943 source is identified with PKS 1622-29. We detect the 2AGL J1626-2943 during the time interval MJD 54329.5-54333.5: an MLE analysis yields a detection of 5σ and a flux $F = (95 \pm 26) \times 10^{-8}$ph cm^{-2}s^{-1}. Another detection of 3.8σ with a flux of $F = (117 \pm 35) \times 10^{-8}$ph cm^{-2}s^{-1} is detected in MJD 54517.5-54521.5.

2AGL J1741+5126. The 95% c.l. elliptical confidence region is marginally compatible with FSRQ 4C +51.37. The association can be promoted to identification via the VOUblaz tool thanks to MW information.

2AGL J1803-3935. The 2AGL J1803-3935 source is identified with FSRQ PMN J1802-3940. We detect 2AGL J1803-3935 during the time interval MJD 55077.5-55081.5; a MLE analysis yields a detection of 4.5σ and a flux $F = (46 \pm 14) \times 10^{-8}$ph cm^{-2}s^{-1}.

Table 6: Association with γ-ray catalogues

Catalogue name	Source number	Paper references
0FGL	205	Abdo et al. (2009b)
1AGL	47	Pittori et al. (2009)
1AGLR	54	Verrecchia et al. (2013)
1FGL	1450	Abdo et al. (2010b)
2FGL	1872	Nolan et al. (2012)
3EG	267	Hartman et al. (1999)
3FGL	3033	Acero et al. (2015)
3FHL	1556	Ajello et al. (2017)
AGILE-TEVCAT	52	Rappoldi et al. (2016)
TeGeV	168	Carosi et al. (2015)

Table 7: Extended sources

AGILE name	$\sqrt{TS}$	l_e	b_e	r	Counterp.
2AGL J0617+2239e	9.7	189.07	2.92	0.27	IC 443
2AGL J1856+0119e	10.2	34.65	-0.39	0.30	W44
2AGL J1634-4734e	10.2	336.38	0.19	0.35	HESS J1632-478
2AGL J2044+5012e	4.5	88.75	4.67	0.59	HB 21

Extended sources modelled as 2D Gaussian in the 2AGL analysis. The values l_e and b_e are the centre of the extended region, in Galactic coordinates, which could be slightly different from the point-like source position. The r column indicates the dispersion for Gaussian sources. The $\sqrt{TS}$ in the table is related to the result of the fitting with the extended shape with a PL spectral model with $\alpha = 2.1$. Fluxes and spectra are reported in Table 10 and Table 11.

2AGL J1833-2104. The 2AGL J1833-2104 source is identified with FSRQ PKS 1830-211 (Donnarumma et al. 2011). We detect 2AGL J1833-2104 during many time intervals in the four-day timescale light curve. The two main flares are; MJD 54529.5-54533.5, where a MLE analysis yields a detection of 4.0σ and a flux $F = (48 \pm 15) \times 10^{-8}$ph cm^{-2}s^{-1}; and MJD 55113.5-55117.5, where a MLE analysis yields a detection of 5.5σ and a flux $F = (50 \pm 12) \times 10^{-8}$ph cm^{-2}s^{-1}. An ATEL is reported for this source (see Table 12) during the pointing mode.

2AGL J1849+6706. The 2AGL J1849+6706 source is identified with FSRQ S4 1849+67. We detect 2AGL J1849+6706 during many time intervals in the four-day timescale light curve. The two main flares are: MJD 54637.5-54641.5, where a MLE analysis yields a detection of 4.2σ and a flux $F = (42 \pm 14) \times 10^{-8}$ph cm^{-2}s^{-1}; and MJD 54853.5-54857.5 , where a MLE analysis yields a detection of 4.5σ and a flux $F = (44 \pm 14) \times 10^{-8}$ph cm^{-2}s^{-1}.

2AGL J1913-1928. We found two interesting sources within the 2AGL J1913-1928 95% c.l. elliptical confidence region: PMN J1911-1908 (an already known γ-ray emitter present in the 3FGL catalogue - 3FGL J1911.4-1908) and PKS B1908-201 (3FGL J1911.2-2006). We detect 2AGL J1913-1928 during the OB 4800 (MJD 54406.5-54435.5); a MLE analysis yields a detection of 5.7σ and a flux $F = (80 \pm 16) \times 10^{-8}$ph cm^{-2}s^{-1}, but this detection still excludes the two sources. Another detection is reported during the time interval MJD 54725.5-54729.5; a MLE analysis yields a detection of 4.0σ and a flux $F = (40 \pm 12) \times 10^{-8}$ph cm^{-2}s^{-1} that is associable only with the PMN J1911-1908. Using the VOUblaz tool, thanks to spectral MW information, the most probable association would be with the PKS B1908-201. In any case, owing to the uncertainties this source is classified as unidentified.

2AGL J2025+3352. The 2AGLJ2025+3352 source is identified with BCU B2 2023+33. We detect 2AGL J2025+3352 during the time interval MJD 54425.5-54429.5; a MLE analysis yields a detection of 5.6σ and a flux $F = (109 \pm 25) \times 10^{-8}$ph cm^{-2}s^{-1}.

2AGL J2027-0740. The 2AGL J2027-0740 source is identified with PKS 2023-07. We detect 2AGL J2027-0740 during many time intervals (see Fig. 12): (i) MJD 54389.5-54393.5 with a detection of 6σ and a flux $F = (60 \pm 13) \times 10^{-8}$ph cm^{-2}s^{-1}; (ii) MJD 54417.5-54421.5 with a detection of 7.6σ and a flux $F = (113 \pm 21) \times 10^{-8}$ph cm^{-2}s^{-1}; and (iii) MJD 54425.5-54429.5 with a detection of 5.4σ and a flux $F = (80 \pm 19) \times 10^{-8}$ph cm^{-2}s^{-1}.

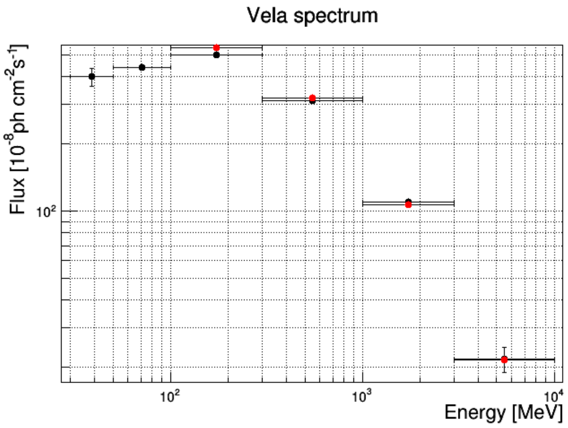

(a) Vela pulsar

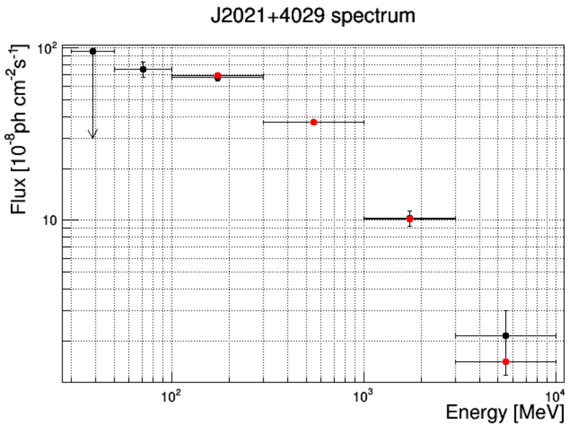

(b) 2AGL J2021+4029 (Gamma Cygni and LAT PSR J2021+4026)

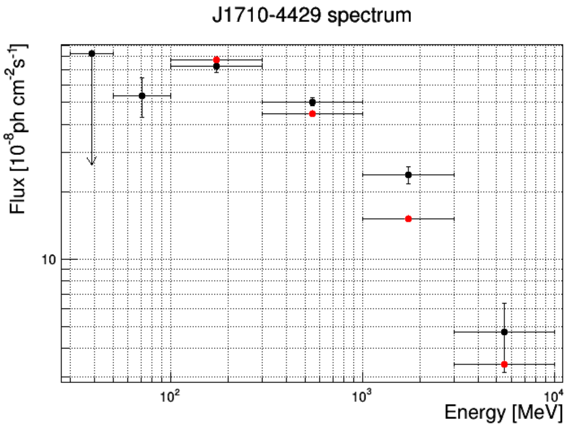

(c) 2AGL J1710-4429

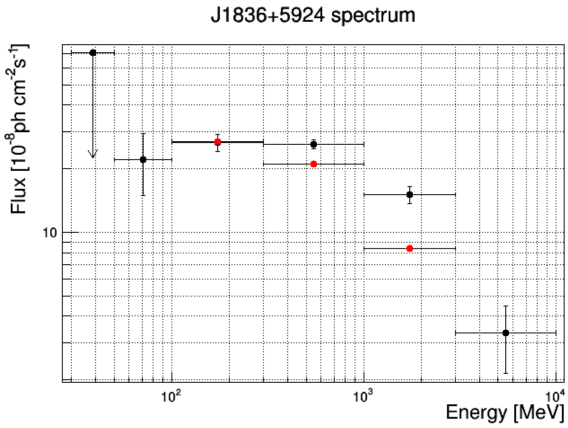

(d) 2AGL J1836+5924 (PSR J1836+5925)

Fig. 10: Comparison between the 2AGL (black spectra; 30 MeV – 10 GeV) and 3FGL (red spectra; 100 MeV – 10 GeV) spectra for some of the most highly exposed AGILE-GRID sources. Error bars are 1σ statistical error; upper limits are 2σ. Different values in flux at the highest energy bands depend on the evaluation of the cut-off energies due to the statistics.

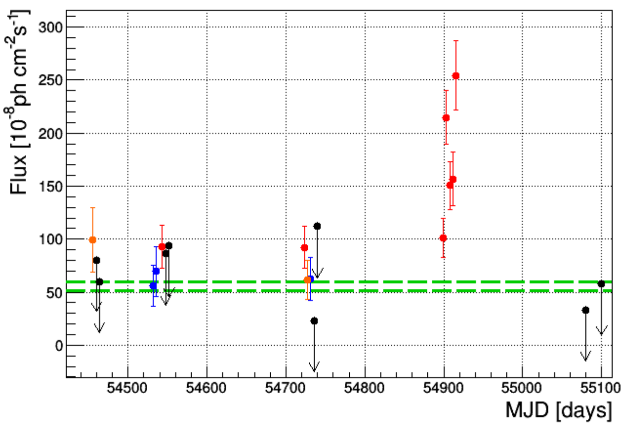

Fig. 11: Light curve of PKS 1510-089 in the energy range 100 MeV – 10 GeV with a four-day resolution. The black downward arrows represent 2σ upper limits. The blue, orange, and red circles refer to a $\sqrt{TS} \geq 3, \geq 4$, and ≥ 5 respectively. The green dashed lines indicate the average flux plus/minus the error from Table 10.

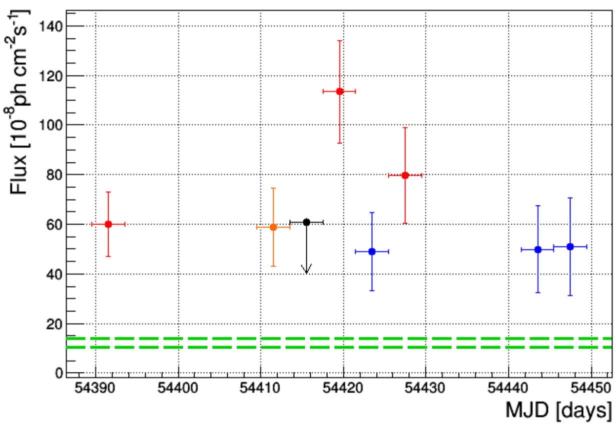

Fig. 12: Light curve of PKS 2023-07 in energy range 100 MeV – 10 GeV, with a four-day resolution. The black downward arrows represent 2σ upper limits. The blue, orange, and red circles refer to a $\sqrt{TS} \geq 3, \geq 4$, and ≥ 5 ,respectively. The green dashed lines indicate the average flux plus/minus the error from Table 10

2AGL J2202+4214. This source is firmly identified with BL Lacertae. Firm identification of this source has been established via the VOUblaz tool thanks to MW information.

2AGL J2254+1609. This source is firmly identified with 3C454.3. Fig. 13 reports the light curve in the pointing period. Firm identification of this source has been established thanks to

Table 8: 2AGL sources with curved spectra.

2AGL name	F_γ	ΔF_γ	$\sqrt{TS}$	SM	α	$\Delta\alpha$	E_c	ΔE_c	β	$\Delta\beta$	TS_{curved}	Counterpart
J0835-4514	969.5	13.8	168.9	PS	1.71	0.04	3913.1	533.6	1.35	0.30	127.8	PSR J0835-4510
J0634+1749	426.1	9.8	76.4	PS	1.71	0.09	1232.0	69.1	0.50	0.20	82.2	PSR J0633+1746
J1710-4429	154.0	8.4	43.5	PC	1.51	0.10	3025.2	957.4			16.0	PSR J1709-4429
J1836+5924	71.8	5.2	41.3	PC	1.21	0.16	1988.4	662.3			30.4	LAT PSR J1836+5925
J2021+4029	119.3	5.9	43.8	PC	1.76	0.09	3307.6	1335.7			16.0	LAT PSR J2021+4026
J2021+3654	70.9	7.9	21.3	PC	1.38	0.30	960.6	361.1			17.4	PSR J2021+3651
J0007+7308	41.6	4.2	26.2	PC	1.29	0.22	2003.9	1010.3			16.0	PSR J0007+7303
J1856+0119e	58.8	8.1	13.2	LP	2.54	0.30	1018.7	59.0	1.00	0.10	15.9	SNR W44
J1801-2334	35.8	10.2	7.5	LP	3.38	0.46	2935.1	543.3	0.68	0.20	21.6	SNR W28

2AGL sources with curved spectra. The parameters F_γ and ΔF_γ are the photon flux in 10^{-8} ph cm^{-2}s^{-1} and related 1σ statistical error in the energy range 100 MeV – 10 GeV (summed over 4 bands); $\sqrt{TS}$ is the significance derived from likelihood test statistic in the same energy band. The value *SM* is the best-fit spectral model (see also Sect. 4.1.2): PC indicates PL with exponential cut-off fit to the energy spectrum and PS indicates PL with super exponential cut-off. For these models α, β, and E_c are the indexes and the cut-off energies expressed in MeV with related 1σ errors. The parameter LP indicates log-parabola fit to the energy spectrum, in this case E_c is the pivot energy in MeV, α is the first index, and β the curvature. TS_{curved} is the test statistic used for selection of curved spectral shape. The last column reports the association with known counterparts.

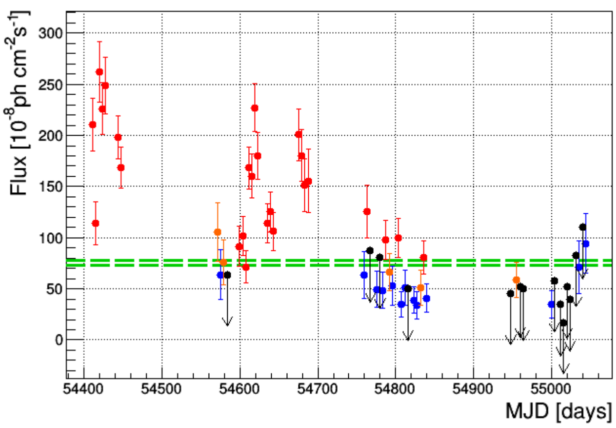

Fig. 13: Light curve of 3C454.3 in the energy range 100 MeV – 10 GeV, with a four-day resolution. The black downward arrows represent 2σ upper limits. The blue, orange, and red circles refer to a $\sqrt{TS}$ value ≥ 3, ≥ 4, and ≥ 5, respectively. The green dashed lines indicate the average flux plus/minus the error from Table 10

different MW campaigns (Vercellone et al. 2008a; Vercellone at al. 2008b; Donnarumma et al. 2009; Vercellone at al. 2010; Pacciani et al. 2010; Striani et al. 2010; Vercellone at al. 2011). Many ATELs are reported for this source (see Table 12).

7.2. AGILE-only sources

In Table 13 we report the full list of AGILE-only sources, i.e. 2AGL sources that do not have any counterpart on 1FGL, 2FGL, or 3FGL catalogues. For AGILE-only sources, the light curves over one-, four-, and seven- day timescales were calculated, in addition to the light curves estimated over OB timescales. All the γ-ray fluxes reported below for each source are estimated through the AGILE-GRID MLE analysis in the energy range 100 MeV – 10 GeV. Some detections with a significance of less than 4σ are also reported for a possible identification.

2AGL J0714+3318. This source is already part of 1AGL and 1AGLR catalogues (based on single OB data analysis); we have a detection in the OB 4200 (MJD 54377.5-54385.5), as in 1AGLR: a MLE analysis over this period yields a detection of 4.0σ and a flux $F = (30 \pm 9) \times 10^{-8}$ph cm^{-2}s^{-1}. Just outside the 95% c.l. elliptical confidence region we note the 5BZQ J0719+3307/B2 0716+33 classified as a FSRQ and associated with the Fermi-LAT source 3FGL J0719.3+3307. Using the VOUblaz tool, we investigated some candidate associations in other wavelengths: just outside the 95% error ellipse, there is the 3HSP J071223.5+331333 that has a SED compatible with the AGILE-GRID sensitivity.

2AGL J1120-6222. The 2AGL J1120-6222 shows a high-confidence detection over the period MJD 55055.5-55062.5 (seven days); a MLE analysis yields a detection of 4.6σ and a flux $F = (67 \pm 18) \times 10^{-8}$ph cm^{-2}s^{-1}. Interestingly, we note that just inside the 95% c.l. elliptical confidence region it is located the HMXB 1A 1118-615 (WRAY 15-793), a Be X-ray binary system included in the INTEGRAL General Reference Catalog (INTREFCAT; version 41 of the 22 June 2018; (Ebisawa et al. 2003)).

2AGL J1138-1724. The 2AGL J1138-1724 source is identified with the BL Lac 5BZB J1137-1710, also associated with 2FHL J1137.9-1710. We detect a γ-ray flare during the time interval MJD 54968.5-54969.5 (one-day timescale): an MLE analysis yields a detection of 4σ and a flux $F = (130 \pm 50) \times 10^{-8}$ph cm^{-2}s^{-1}.

2AGL J1203-2701c. This source is denoted with 'c' because the position could be influenced by another γ-ray excess just outside the 95% c.l. elliptical confidence region. No candidate source within the ellipse is present from flat spectrum radio source of other catalogs of interest. The VOUblaz tool allows us to find some candidate sources to be associated with this 2AGL, of which 5BZQ J1205-2634, a low-energy cutoff BL Lacs (LBL,

Table 9: Spectral information for the 2AGL catalogue columns description of Table 11 and Table 15.

Column	Units	Description
Name		See Table 4 for a detailed description. The full list of 2AGL sources is reported in Table 10
$\sqrt{TS}$		Significance derived from likelihood test statistic in the energy range 100 MeV – 10 GeV
SM		Spectral model. PL indicates power-law fit to the energy spectrum; PC indicates power-law with exponential cutoff fit to the energy spectrum; PS indicates power-law with super exponential cut-off fit to the energy spectrum; LP indicates log-parabola fit to the energy spectrum
α		Spectral index for PL, PC, and PS spectral models, first index for LP spectral model, in the energy range 100 MeV – 10 GeV; see Sect. 4.1.2 for the definition of α
$\Delta\alpha$		Statistical 1σ uncertainty of α, in the energy range 100 MeV – 10 GeV
E_c	MeV	Cut-off energy for PC and PS spectral models, pivot energy for LP spectral model, in the energy range 100 MeV – 10 GeV; see Sect. 4.1.2 for the definition of E_c
ΔE_c	MeV	Statistical 1σ uncertainty of E_c, in the energy range 100 MeV – 10 GeV
β		Second index for PS spectral models, curvature for LP spectral model, in the energy range 100 MeV – 10 GeV; see Sect. 4.1.2 for the definition of β
$\Delta\beta$		Statistical 1σ uncertainty of β, in the energy range 100 MeV – 10 GeV
F_a	10^{-8} ph cm^{-2}s^{-1}	Photon flux in the 30 MeV - 50 MeV energy band, with asymmetric errors
σ_a		Significance derived from likelihood test statistic in the 30 MeV - 50 MeV energy band. If $\sigma_a < 3$ the 2σ the upper limit is selected
F_b	10^{-8} ph cm^{-2}s^{-1}	Photon flux in the 50 MeV - 100 MeV energy band, with asymmetric errors
σ_b		Significance derived from likelihood test statistic in the 50 MeV - 100 MeV energy band. If $\sigma_b < 3$ the 2σ the upper limit is selected
F_1	10^{-8} ph cm^{-2}s^{-1}	Photon flux in the 100 MeV - 300 MeV energy band, with asymmetric errors
σ_1		Significance derived from likelihood test statistic in the 100 MeV - 300 MeV energy band. If $\sigma_1 < 3$ the 2σ the upper limit is selected
F_2	10^{-8} ph cm^{-2}s^{-1}	Photon flux in the 300 MeV – 1000 MeV energy band, with asymmetric errors
σ_2		Significance derived from likelihood test statistic in the 300 MeV – 1000 MeV energy band. If $\sigma_2 < 3$ the 2σ the upper limit is selected
F_3	10^{-8} ph cm^{-2}s^{-1}	Photon flux in the 1000 MeV – 3000 MeV energy band, with asymmetric errors
σ_3		Significance derived from likelihood test statistic in the 1000 MeV – 3000 MeV energy band. If $\sigma_3 < 3$ the 2σ the upper limit is selected
F_4	10^{-8} ph cm^{-2}s^{-1}	Photon flux in the 3000 MeV – 10000 MeV energy band, with asymmetric errors
σ_4		Significance derived from likelihood test statistic in the 3000 MeV – 10000 MeV energy band. If $\sigma_4 < 3$ the 2σ the upper limit is selected
ID or ass.		Designator of identified or associated source. A * indicates a possible marginal positional association
Flag		Flag (see Table 2)
Class		Class (see Table 5)

defined by (Padovani and Giommi 1995)) just outside the 95% error ellipse, is the most probable counterpart.

2AGL J1312-3403. We note that outside the AGILE 95% error ellipse of this AGILE-only source at about 0.46°is 3FGL J1311.8-3430, which is a LAT PSR J1311-3430 (associated with 0FGL J1311.9-3419 and 3EG J1314-3431). In MJD 54699.5-54701.5 time interval (two-day timescale) we detect a spatially coincident event at 4.0σ with a flux of $F = (97 \pm 38) \times 10^{-8}$ph cm^{-2}s^{-1}. The VOUblaz tool also shows an intermediate synchrotron peaked BL Lacs (IBL) candidate just outside the 95% error ellipse that has a single radio point in the SED, weak XMM X-ray data, and no γ-rays; extrapolation from X-ray to γ-ray in the AGILE-GRID range is difficult.

2AGL J1402-8142. This source has no known candidate counterparts within the 95% elliptical confidence region: either radio or from specific source classes. In MJD 54751.5-54753.5 time interval (two-day timescale) we detect an event at 3.9σ with a flux of $F = (56 \pm 20) \times 10^{-8}$ph cm^{-2}s^{-1}. Just outside the ellipse at $\sim 1°$, there is the 4U 1450-80 X-ray source of the INTREFCAT.

2AGL J1628-4448. Low latitude source without any known γ-ray source within its elliptical confidence region. A detection appears in the OB 6200 (MJD 54719.5-54749.5) at 3.6σ and a flux $F = (121 \pm 35) \times 10^{-8}$ph cm^{-2}s^{-1}. Fermi-LAT (which was running during the OB 6200) did not report the detection of the source because it was just for a 14% of the time below 50° off-axis; more details in Appendix A.

2AGL J1631-2039. This is a high latitude source whose elongated ellipse does not include any known γ-ray source. We detect this source as active over the OB 6800 period (MJD 54890.5-54921.5), at 3.6σ, and a flux $F = (16 \pm 5) \times 10^{-8}$ph cm^{-2}s^{-1}. Using the VOUblaz tool an interesting 408 mJy (1.4 GHz) NVSS radio source, PMN J1629-2039, is found at 13′ (R.A.,Dec.: 247.26267,-20.44881), but the possible extrapolated γ-ray emission into the AGILE-GRID range for a possible LBL (Padovani and Giommi 1995) blazar is too weak for the AGILE-GRID sensitivity.

2AGL J1636-4610 Low latitude source with a detection at 4.1σ and a flux $F = (16 \pm 4) \times 10^{-8}$ph cm^{-2}s^{-1} appears over the OB 6800 period (MJD 54890.5-54921.5).

2AGL J1640-5050c. Low latitude source showing a very soft spectral index of 2.84 ± 0.17. Two detections appear from the OB timescale light curve: one at 3.9σ and a flux $F = (19.2 \pm 5.2)\times10^{-8}$ph cm^{-2}s^{-1} on MJD 54647.5-54672.75 (OB 5900) and the other at 3.4σ and a flux $F = (12.4 \pm 3.8) \times 10^{-8}$ph cm^{-2}s^{-1} on MJD 55055.5-55074.5 (OB 7800). Its large elliptical confidence location region partially overlaps with the unassociated 3FGL J1643.6-5002 error ellipse. Another Fermi-LAT unassociated source, 3FGL J1639.4-5146, appears at around 1° from the source centroid. This source is denoted with 'c' owing to the large source confidence location region.

2AGL J1731-0527. High latitude source without any known γ-ray source within its elliptical confidence region. It shows a detection at 3.7σ and flux $F = (27.6 \pm 8.7) \times 10^{-8}$ph cm^{-2}s^{-1} over the OB period MJD 55104.5-55119.5 (OB 8300), plus other detections over two-, four-, and seven-day timescales. Within the confidence location region, at 15′ from the source centroid, lies the flat-spectrum radio source CRATES J173032-051505.

2AGL J1736-7819. Low latitude source with no known γ-ray source within its elliptical confidence region. Partially overlapping with the 95% confidence contour of the EGRET source 3EG J1720-7820. The source is also detected on a four-day integration starting at MJD=54653.5 at 3.1σ, with a flux $F = (21 \pm 8) \times 10^{-8}$ph cm^{-2}s^{-1}. At 19′ from the 2AGL J1736-7819 centroid lies the radio source PKS 1723-78.

2AGL J1740-3013. This is a Galactic centre region source, positionally consistent with TeVJ1741-302 (HESS J1741-302). Despite several attempts to constrain its nature, no plausible counterpart has been found (Abdalla et al. 2018). We note an increasing flux from this source during the seven-day time interval MJD 54740.5-54747.5; a MLE analysis yields a detection of 4.3σ and a flux $F = (86 \pm 23) \times 10^{-8}$ph cm^{-2}s^{-1}.

2AGL J1743-2613c. The 2AGL J1743-2613c is an unidentified source of the Galactic centre region. Within 0.8° we found 3FGL J1740.5-2642, and 3FGL J1741.9-2539 associated with the BCU NVSS J174154-253743. This source is denoted with 'c' owing to the complexity of the region.

2AGL J1746-2921. The 2AGL J1746-2921 is a flaring source of the Galactic centre. The source had shown a increasing γ-ray emission in the OB 6200 (MJD 54719.5-54749.5). More refined light curves of one-, four-, and seven- day timescales showed flaring activities in these periods: 54719.5-54726.5 (seven days), 54730.5-54731.5 (one day), 54737.5-54741.5 (four days).

2AGL J1754-2626.The 2AGL J1754-2626 is an unidentified source near the Galactic centre. At about 11′ appears the high-mass X-ray binary IGR J17544-2619 (Liu et al. 2006), seen by INTEGRAL (Ebisawa et al. 2003) and also by Swift-BAT (Oh et al. 2018). The source shows two flaring episodes on the OB 5600 (MJD 54566.5/54586.5) and OB 6200 (MJD 54719.5-54749.5), both with a significance above 5σ and a flux $F = (58 \pm 12) \times 10^{-8}$ph cm^{-2}s^{-1} and $F = (23\pm5)\times10^{-8}$ph cm^{-2}s^{-1}, respectively.

2AGL J1820-1150c. Low latitude source with no known γ-ray source within its elliptical confidence region. It shows a strong flaring episode at 6.1σ and a flux $F = (85 \pm 16) \times 10^{-8}$ph cm^{-2}s^{-1} over the OB 4800 period (MJD 54406.5-54435.5). No clear possible association has been identified. This source is denoted with 'c' owing to the large uncertainty on its location.

2AGL J1823-1504. The 2AGL J1823-1504 is an unidentified source of the Galactic plane. The 3EG J1824-1514 was partially inside the 95% elliptical confidence region. We detect a γ-ray flare from 2AGL J1823-1504 region in the time interval MJD 54552.5-54553.5; a MLE analysis yields a detection of 4.1σ and a flux $F = (281 \pm 86) \times 10^{-8}$ph cm^{-2}s^{-1}.

2AGL J1857+0015. Low latitude source without any known γ-ray source within its elliptical confidence region, close to the W44 region. It shows only a detection at 3.4σ and a flux $F = (105 \pm 39) \times 10^{-8}$ph cm^{-2}s^{-1} over the four-day timescale MJD 54773.5-54777.5. At 46′ from the source centroid lays the pulsar PSR B1853+00.

2AGL J1910-0637. This source is just outside the Galactic plane and we have two detections on a one-week timescale, the most significant at 3.6σ in MJD 54572.5-54579.5 time interval. No γ-ray source neither flat spectrum radio source are within the 95% elliptical confidence region.

2AGL J1913+0050. This AGILE-GRID-only source appears just below the Galactic plane. It shows two detections over OB 6400 (MJD 54770.5-54800.5): one at 3.5σ and flux $F = (8.0 \pm 2.5) \times 10^{-8}$ph cm^{-2}s^{-1}, and the other at 3.2σ and flux $F = (14.0 \pm 4.6) \times 10^{-8}$ph cm^{-2}s^{-1} on OB 6500 (MJD 54800.5-54820.5). Interestingly, within the 95% elliptical confidence location region, at 27′ from the source centroid, appears the low-mass X-ray binary Aql X-1 (also known 4U 1908+005), which has also been seen by SWIFT-BAT (SWIFT J1911.2+0036 (Oh et al. 2018)).

2AGL J1927-4318. High latitude source without any known γ-ray source within its elliptical confidence region. It shows a detection at 3.3σ and a flux $F = (17.2 \pm 6.0) \times 10^{-8}$ph cm^{-2}s^{-1} over the OB 6200 period (MJD 54719.5-54749.5) plus a detection at 3.1σ over a short timescale of four days on MJD 54533.5-54537.5. Within the AGILE-GRID elliptical source contour, there is the radio source PKS B1922-430 (at 25′ from the source centroid).

2AGL J2029+4403. Low latitude source in the complex Cygnus region without any known γ-ray source within its elliptical confidence location region. We note that the LAT pulsar 3FGL J2030.8+4416 is at about 28′.

2AGL J2055+2521. The PSR 3FGL J2055.8+2539 is at 22′ from the source centroid, just outside the 95% elliptical confidence region. It shows a detections in MJD 54426.5-54427.5 (one-day timescale) at 4.1σ and flux $F = (191 \pm 71) \times 10^{-8}$ph cm^{-2}s^{-1}.

2AGL J2206-1044. We have a γ-ray detection on OB 8300 (MJD 55104.5-55111.5) at 4.7σ and a flux $F = (63 \pm 16) \times 10^{-8}$ph cm^{-2}s^{-1}. A 390 mJy NVSS (1.4GHz) radio source is just outside the 95% c.l. elliptical confidence region. The source has a $VI = 1$ at a four-day timescale.

2AGL J2227+6418. We detect a γ-ray flare from 2AGL J2227+6418 region over the time interval MJD 54425.5-54429.5 (four days). An MLE analysis yields a detection of 4.9σ and a flux $F = (32 \pm 8) \times 10^{-8}$ph cm^{-2}s^{-1}.

2AGL J2228-0818. The 2AGL J2228-0818 source is a high latitude AGILE-only source with a variable behaviour. We detect 2AGL J2228-0818 during the time interval MJD 54425.5-54429.5 (four days); a MLE analysis yields a detection of 4.2σ and a flux $F = (61 \pm 18) \times 10^{-8}$ph cm^{-2}s^{-1}. Another interesting episode is in the time interval MJD 54573.5-54577.5: a MLE analysis yields a detection of 4.1σ and a flux $F = (80 \pm 22) \times 10^{-8}$ph cm^{-2}s^{-1}. The source has a $VI = 1$ at a four-day timescale.

2AGL J2303+2120. This high latitude weak source, with a large error ellipse, has been detected in a single two-days integration on MJD 54571.5-54573.5 time interval at 3.7σ and a flux $F = (150\pm50)\times10^{-8}$ph cm^{-2}s^{-1} and at 3σ on a single one-week exposure.

2AGL J2332+8215c. We find a marginal overlap of 2AGL J2332+8215c 95% c.l. elliptical confidence region with FSRQ S5 2353+81. We detect a γ-ray flare from 2AGL J2332+8215c region on the time interval MJD 54425.5-54429.5 (four days): an MLE analysis yields a detection of 5σ and a flux $F = (37 \pm 8) \times 10^{-8}$ph cm^{-2}s^{-1}. No firm association can be established and the source is denoted as 'c' since the region appears noisy.

7.3. γ-ray only sources

In this section we report notes for some γ-ray only sources. Table 14 reports the full list.

2AGL 0032+0512c. This source is marginally spatially coincident with 3FGL J0030.4+0451, associated with the PSR J0030+0451. This source is denoted with 'c' because the evaluation of its position is strongly influenced by the spectral index α. For this reason we keep this source as γ-ray only without association with the PSR. The VOUblaz tool allows us to find some possible blazar candidates among which: (i) 5BZQ J0029+0554 (CRATES J002945+055443), a possible LBL. The SED created with the tool shows a hint of synchrotron bump but the extrapolated γ-ray emission is too weak for the AGILE-GRID sensitivity; (ii) a candidate NVSS radio source (NVSS J003047+044038). Again considering the source SED the possible synchrotron peak is too low for the extrapolated γ-ray emission in the AGILE-GRID band.

2AGL J0221+6208c. The region of 2AGL J0221+6208c includes 3FGL J0217.3+6209 (TXS 0213+619), 3FGL J0220.1+6202c, 3FGL J0223.6+6204 (unass.), and partially 3FGL J0224.0+6235. Integrating in the time interval MJD 54641.5-54645.5 (four-day timescale), a MLE analysis yields a detection of 4.1σ and a flux $F = (45 \pm 13) \times 10^{-8}$ph cm^{-2}s^{-1} in the energy range 100 MeV – 10 GeV, but the 95% confidence region already includes the mentioned 3FGL sources. For this reason we classify this source as γ-ray only but without association with a specific 3FGL source.

2AGL J1103-7747. This source is spatially associated with the unclassified γ-ray source 3FGL J1104.3-7736c. Using the VOUblaz tool at least three candidate radio source are found, among which CRATES J105731-772424 at 4.9′ from the Fermi-LAT source: the SED seems compatible with a weak γ-ray emission in the AGILE-GRID range.

2AGL J1718-0432. The 2AGL J1718-0432 source is spatially associated with the unclassified γ-ray source 3FGL J1720.3-0428, and shows a detection at 4.0σ and a flux $F = (35 \pm 10) \times 10^{-8}$ph cm^{-2}s^{-1} in MJD 54897.5-54899.5. The VOUblaz tool shows a known blazar with which no radio/X-ray could be associated; this blazar is 5BZQ J1716-0452 at a distance of 27.316′, which is a probable FSRQ; the SED shows a clear synchrotron bump, but without X-ray or γ-ray counterparts.

2AGL J1737-3206. The 2AGL J1737-3206 shows a full overlapping with 3FGL J1737.3-3214c.

2AGL J1847-0157 The 2AGL J1847-0157 shows a full overlapping with 3FGL J1848.4-0141. We note the source TeV J1848-017 (HESS J1848-018) inside the 95% c.l. elliptical confidence region, already present in the AGILE TeVCat (Rappoldi et al. 2016).

7.4. Pulsars

Forty-one pulsars are associated with 2AGL sources. Thirteen pulsars have been identified with pulsed timing analysis on AGILE data, but only seven of these are included in the 2AGL catalogue because for these we also obtained spatial identification using the MLE analysis.

PSR J2021+3651 (2AGL J2021+3654) was the first pulsar identified by pulsation in the AGILE-GRID γ-ray data (Halpern et al. 2008). In (Pellizzoni et al. 2009) the pulsation of Vela (2AGL J0835-4514), Geminga (2AGL J0634+1749; Fig. 10 shows the spectra), Crab (2AGL J0534+2205), and PSR B1706-44 (2AGL J1710-4429) have been reported.

In (Pellizzoni et al. 2009b) the detection of pulsation for seven additional pulsars has been reported: first, four pulsars have been identified only by pulsation because no spatial identification using the MLE analysis is possible, i.e. PSR J1357-6429, PSR J1524-5625, PSR J1824-2452, and PSR J2043+2740; second, PSR J1016-5857 (2AGL J1015-5852), PSR J1513-5908 (2AGL J1517-5909), and PSR J2229+6114 (2AGL J2230+6113) have been identified with both pulsed emission and MLE analysis. An additional comment about PSR J1824-2452 is necessary because (Pellizzoni et al. 2009b) also reported a MLE identification of this source; PSR J1824-2452, inside the globular cluster M28, was observed by the AGILE-GRID with good significance ($> 4\sigma$) but only within a time interval of five days during a targeted pointing (for details see (Pellizzoni et al. 2009b)). No increase in significance of the detection was obtained with the addition of more data. The source was also detected in the imaging data relative to the same time interval. The apparent single burst of emission observed by the AGILE-GRID might be related to the fact that this millisecond pulsar is known to experience variability episodes (Cognard & Backer 2004). The pulsation of PSR J2021+4026, that is part of the extended source pulsar + nebula 2AGL J2021+4029, has been identified.

To summarise, the seven pulsars with identified pulsed emission that are firmly identified as 2AGL sources are PSR J2021+3651, Vela, Geminga, PSR B1706-44, PSR J1016-5857, PSR J1513-5908, and PSR J2229+6114. The PSR J2021+4026 is classified as a SNR and the Crab region is classified as PWN (see Sect. 7.7) because the analysis considers the integrated flux of the regions.

In the following we report additional notes.

2AGL J1029-5834. The source is associated with PSR J1028-5819 but there is only a partial overlap of the 95% elliptical confidence region.

2AGL J1458-6055. The 95% elliptical confidence region of 2AGL J1458-6055 source partially overlaps the 95% elliptical confidence region of LAT PSR J1459-6053 and 3FGL J1456.7-6046. It is not possible to establish a direct association with the pulsar.

2AGL J1517-5909. PSR J1513-5908 (Pellizzoni et al. 2009b; Pilia et al. 2010(@) is included in the 2AGL J1517-5909 95% elliptical confidence region. In the same region the associated extended source PWN MSH 15-12 is not detected by the AGILE-GRID.

2AGL J1710-4429. PSR J1709-4429 (PSR B1706-44) (Pellizzoni et al. 2009) is firmly identified with 2AGL J1710-4429. Fig. 10 reports the spectra of this 2AGL source.

2AGL J1836+5924. The 2AGL J1836+5924 (Bulgarelli et al. 2008a) is associated with LAT PSR J1836+5925 and shows an exponential cut-off PL spectral shape.

7.5. Cygnus region

The Cygnus region (Fig. 14) is a site of bright diffuse emission, transient, and persistent point-like and extended sources in γ-ray . The most prominent persistent γ-ray point-like sources are the three pulsars: PSR J2021+3651 (2AGL J2021+3654; see Sect. 7.4), PSR J2021+4026 (2AGL J2021+4029; see Sect. 7.8), PSR J2032+4127 (2AGL J2032+4135). Furthermore, three microquasars were detected in this region with variable γ-ray emission: Cygnus X-1 (Sabatini et al. 2010, 2013), Cygnus X-3 (2AGL J2033+4060; Tavani et al. 2009b; Abdo et al. 2009c; Bulgarelli et al. 2012b; Piano et al. 2012), and V404 Cygni (Piano et al. 2017). Cygnus X-1 and V404 Cygni are not part of this catalogue. Many Astronomer's Telegrams are associated with sources of the Cygnus region, in particular with PSR J2021+4026 and Cygnus X-3 (see Table 12).

Two main extended γ-ray sources are present in this region but not present in the 2AGL catalogue because not detected with extended model: the Cygnus cocoon (Ackermann et al. 2011) and the SNR Gamma Cygni (G78.2+2.1, Fraija & Araya 2016).

7.6. Carina region

The Carina region is shown in Fig. 15. We have detected some remarkable sources. We detect η-Carinae (2AGL J1045-5954) binary system, the HMXB 1FLG J1018.6-5856 (Ackermann et al. 2012) (2AGL J1020-5906), eight pulsars, i.e. PSR J1016-5857 (2AGL J1015-5852; see Sect. 7.4), PSR J1019-5749 (2AGL J1020-5752), PSR J1028-5819 (2AGL J1029-5834), LAT PSR J1044-5737 (2AGL J1045-5735), PSR J1048-5832 (2AGL J1048-5836), PSR J1112-6103 (2AGL J1111-6060), LAT PSR J1135-6055 (2AGL J1136-6045), PSR J1203-63 (2AGL J1204-6247), a marginal association with the PSR J1028-581 (2AGL J1029-5834; see Sect. 7.4), and two AGNs ATG20G J112319-641735 (associated with 2AGL J1119-6443) and PMN J1047-6217 (identified with 2AGL J1052-6234, see Sect. 7.1).

η-Carinae (2AGL J1045-5954) is a colliding wind binary in the same Galactic region of the Carina nebula. The system was observed from radio to X-ray and, in 2009, the AGILE-GRID detected for the first time γ-ray emission correspondent to η-Carinae (Tavani et al. 2009c; Sabatini et al. 2011). The source was also then detected by Fermi-LAT (Abdo et al. 2009b, 2010a) with a flux consistent with the AGILE-GRID estimation. The absence of γ-ray emission variation correlated with the X-ray variability cannot provide an unambiguous identification of the detected source with η-Carinae. However, the AGILE-GRID revealed a flare activity that could be associated with particle acceleration and, in recent months, a Nustar observation has detected non-thermal variable X-ray emission with the same spectral index 1.65 as in the γ-ray band (Hamaguchi et al. 2018). This could be the first evidence that η-Carinae is emitting high-energy photons (in both hard X-ray and γ-ray bands) likely from particle acceleration.

7.7. Pulsar wind nebulae (PWN)

2AGL J0534+2205. The Crab pulsar has been identified by pulsation in Pellizzoni et al. (2009). Crab is the most prominent PWN of the 2AGL catalogue. The anti-centre region (including Crab and Geminga) was observed for ~ 45 days, mostly in 2007 September and in 2008 April (during AO1) with the addition of other sparse short Crab pointings for SuperAGILE calibration purpose during the science verification phase. Fig. 16 shows the light curve with one-day resolution, where the first recorded γ-ray flare from the Crab nebula is evident (Tavani et al. 2011; Vittorini at al. 2011; Striani et al. 2011, 2013). The flux reported in the 2AGL catalogue includes the contribution from both pulsar and nebula, excluding the first γ-ray flare from the Crab nebula, and no separate analysis is made for this catalogue because we rely on the already cited papers.

2AGL J0835-4514. In the 2AGL catalogue the Vela region is reported as a pulsar (see Sect. 7.4). The detection of the Vela PWN with the AGILE-GRID was reported in (Pellizzoni et al. 2010).

2AGL J1634-4734e. HESS J1632-478 (Balbo et al. 2010), associated with 2AGL J1634-4734e, is an energetic pulsar wind nebula with an age of the order of 10^4 years in the Norma region. The nebula has a size of 1 pc and is modelled as an extended source in the 2AGL catalogue.

7.8. Supernova remnants

The AGILE-GRID has detected many confirmed γ-ray SNRs, all middle-aged and very bright in the radio band.

2AGL J0617+2239e. This source is associated with the SNR IC 443. In angular size, it is the largest SNR detected in the Galaxy in the radio band. Its radio morphology is composed of two interacting synchrotron emitting shells. The AGILE-GRID detects γ-ray emission from IC 443 in correspondence of the more external radio shell (Tavani et al. 2010a). In 2013, Fermi-LAT published a γ-ray spectrum down to energies below 200 MeV, confirming the presence of high-energy CR at the SNR shock (Ackermann et al. 2013). TeV γ-ray emission was detected at the centre of the radio shell, in correspondence of a likely associated molecular cloud (MC) (Acciari et al. 2009). The spectral index of the remnant is steeper than 2.0 and the cut-off is at energies below 100 TeV.

2AGL J1715-3815. This extended source is associated with the TeV emitting SNR CTB 37A (Aharonian et al. 2008b, HESS J1714-385) located at a distance of ~ 13 kpc. The TeV emission is correlated with detected MCs (Maxted et al. 2013) and could be associated with the non-thermal X-ray source CXOU J171419.8-383023. The detection of this SNR with Fermi-LAT in 2013 (Brandt et al. 2013) in the GeV band is correlated with TeV and X-ray emissions, supporting the likely hypothesis of the presence of energised particles in the SNR shock with surrounding MCs.

2AGL J1801-2334. This source is associated with the SNR W28, another mixed morphology SNR with a shell radio structure described by a set of large, coherent arcs running along the edge of the remnant. The AGILE-GRID detected γ-ray emission from two different regions of this remnant, correlated with two MCs at different distances and with an anti-correlation in brightness with the TeV emission (Giulani et al. 2010; Aharonian et al. 2008a). In 2014, Fermi-LAT confirmed the AGILE-GRID detection (Hanabata et al. 2014). The γ-ray emission is interpreted as accelerated CR interacting with two distant MCs. The parameters in this catalogue are found assuming a LP shape for the spectrum (see Table 8), with a very steep spectral index. We are unable to detect W28 with an extended model; only the point-like model provides a detection.

2AGL J1856+0119e. This source is associated with the very radio-bright, middle-aged SNR W44. The AGILE-GRID detects a γ-ray spectrum down to energies below 200 MeV, confirming for the first time the presence of energised CRs in correspondence of a SNR/MC interaction shock (Giuliani et al. 2011; Cardillo et al. 2014). This spectrum was confirmed by Fermi-LAT in 2013 (Ackermann et al. 2013). No TeV emission has been detected from this source. The parameters in this catalogue are found assuming a LP shape for the spectrum with a steep spectral index (see Sect. 8).

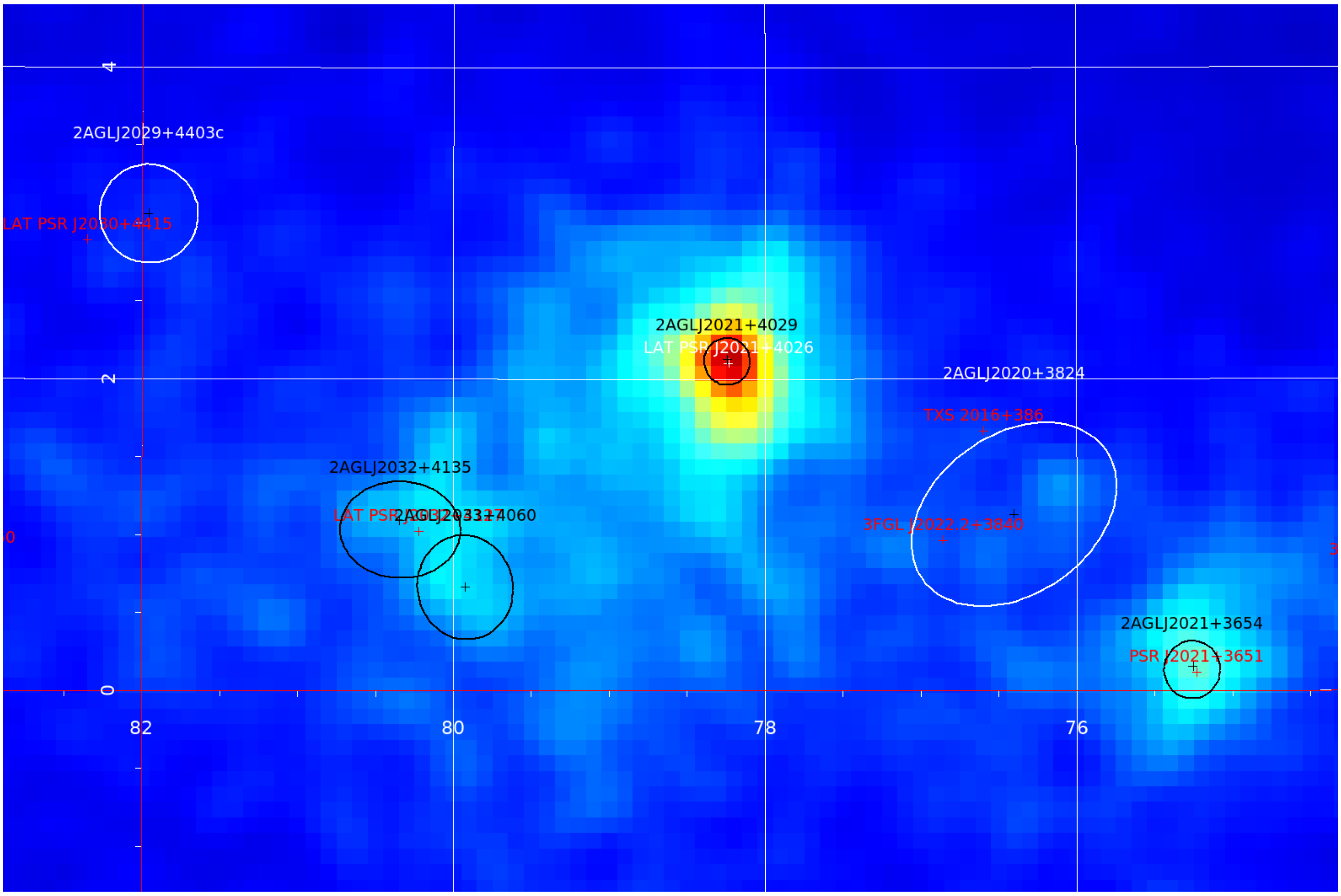

Fig. 14: Count map of the Cygnus region in Galactic coordinates with superimposed the 2AGL catalogue 95% c.l. elliptical confidence regions. We report also some associations and 3FGL catalogue 95% c.l. elliptical confidence regions inside the 2AGL regions.

2AGL J1911+0907. This source is in correspondence of the TeV J1911+0905/SNR W49B. The VHE γ-ray emission is found to be point-like and this source is found in the AGILE-GRID data. The SNR originated from a core-collapse supernova that occurred between one and four thousand years ago, and has evolved into a mixed morphology remnant that is interacting with MCs (Abdalla et al. 2018).

2AGL J1924+1416. This source is associated with the SNR W51c, a component of the MC complex W51, together with the two star-forming regions, W51A and W51B. W51C shows a thick incomplete shell-like structure in the radio band, explained by electron synchrotron emission. Fermi-LAT detected γ-ray emission from this remnant, for the first time, in 2009 (Abdo et al. 2009a) and then, thanks to the improvement of the analysis software, the satellite data were re-analysed showing a spectrum down to energies below 200 MeV for this source as well (Jogler et al. 2016). The Major Atmospheric Gamma Imaging Cherenkov telescope (MAGIC) also detected TeV emission from W51c (Aleksic et al. 2012) but, as in all the other γ-ray detected SNRs, the spectrum has a spectral index steeper than the theoretical value of 2 and has a cut-off energy below 100 TeV.

2AGL J2021+4029. The radio source G78.2+2.1 (Gamma Cygni) is a typical shell-type SNR located within the extended emission of the Cygnus X region and it has the pulsar PSR J2021+4026 at its centre. The 2AGL J2021+4029 includes both the SNR Gamma Cygni and the PSR J2021+4026. Fig. 10 reports the spectra in the energy range 100 MeV – 10 GeV. PSR J2021+4026 is found to be variable in γ-ray (Chen et al. 2011; Allafort et al. 2013); many ATELs are associated with this source (see Table 12). Work is ongoing on the analysis of non-pulsed γ-ray emission to separate the pulsar contribution from that due to the SNR (Piano et al. 2019).

2AGL J2044+5012e. This source is associated with the mixed morphology SNR HB 21, located in a dense environment with a radio shape suggesting interaction with a MC. Its γ-ray emission was detected by Fermi-LAT in 2013 (Pivato et al. 2013) but there are no other detection in the γ-ray band. However, the behaviour of the remnant seems to be the same as all the other middle-aged SNRs detected at high energies. We detect HB 21 as an extended source (see Table 7).

7.9. Binaries

The 2AGL catalogue contains the detection of four High Mass X-ray Binaries (HMXB): LSI +61 303 (2AGL J0239+6120; which shows variability), Cygnus X-3 (2AGL J2033+4060; see Sect. 7.5), LS 5039 (2AGL J1826-1438), and 1FGL J1018.6-5856 (2AGL J1020-5906; see Sect. 7.6). Two other TeV emitters, HESS J0632+057 and PSR B1259-63, do not have persistent counterparts in the 2AGL catalogue. Cygnus X-1, which has shown a flaring activity during the pointing mode (see Sect. 7.5),

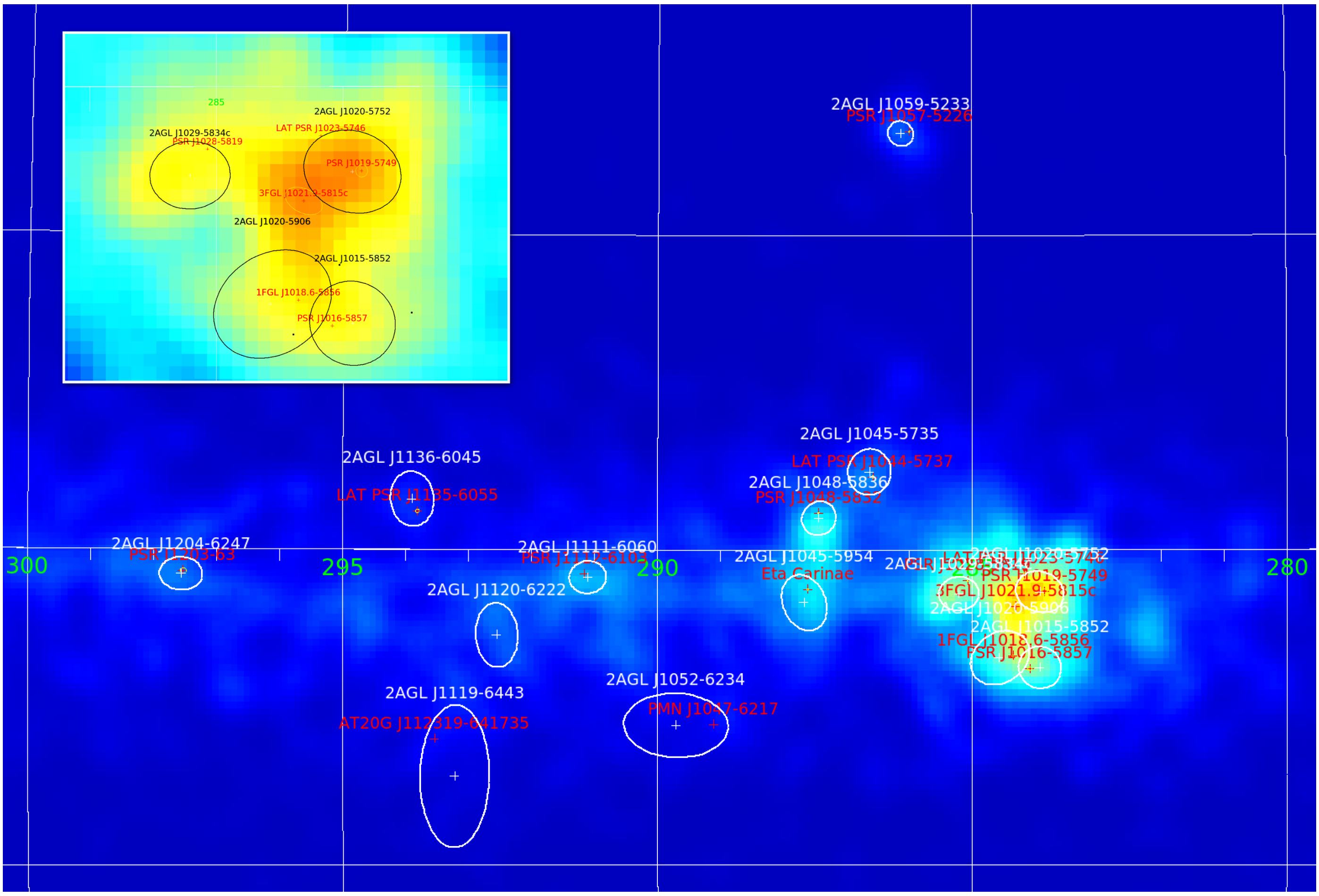

Fig. 15: Count map of the Carina region in Galactic coordinates with superimposed the 2AGL catalogue 95% c.l. elliptical confidence regions. We also report some associations and 3FGL catalogue 95% c.l. elliptical confidence regions inside the 2AGL regions. On top and left there is a zoom of the region around $(l, b) = (285°, 0°)$.

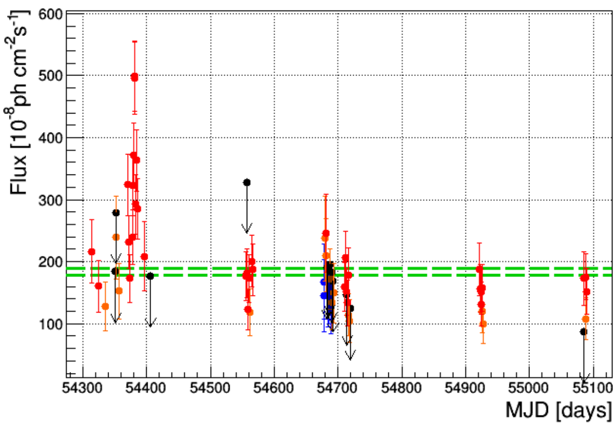

Fig. 16: Light curve of the Crab pulsar+nebula in the energy range 100 MeV – 10 GeV, with a one-day resolution. The black downward arrows represent 2σ upper limits. The blue, orange, and red circles refer to a $\sqrt{TS} \geq 3$, ≥ 4 and ≥ 5, respectively. The green dashed lines indicate the average flux plus/minus the error from Table 10

has no 2AGL counterpart. η-Carinae, identified as a binary system, is included as 2AGL J1045-5954 (see Sect. 7.6).

7.10. Confused sources

In this section we comment on some confused sources (see Sect. 6.1). The sources 2AGL J1203-2701c, 2AGL J1640-5050c, 2AGL J1743-2613c, 2AGL J1820-1150c, and 2AGL J2332+8215c are discussed in Sect. 7.2. The sources 2AGL 0032+0512c and 2AGL J0221+6208c are discussed in Sect. 7.3.

2AGL J1407-6136c. The 95% elliptical confidence region of this 2AGL source partially overlaps the 95% elliptical confidence region of 3FGL J1405.4-6119 and 3FGL J1409.7-6132 (PSR J1410-6132). In the 1AGL catalogue a source was centred at a distance of 1.21° from the current position of this 2AGL source. An ATEL is reported for this source (see Table 12) during the pointing mode.

2AGL J1838-0623c. This is a Galactic plane source with a large 95% c.l. elliptical confidence region, which leads to multiple spatial coincidences. A refined analysis is not able to reduce the c.l. confidence region.

8. 2AGL γ-ray sources list detected below 100 MeV

Table 15 reports an extension of the 2AGL catalogue, which lists the sources also detected in the energy range 50 – 100 MeV. The spectral model is the same as in the 2AGL catalogue and the flux is calculated fixing all the spectral model parameters. Galactic and diffuse emission model parameters are determined independently for each energy band. In addition, the low-confidence extension in the energy range 30 – 50 MeV is also reported in the same table with the same assumptions.

9. Conclusions

This paper presents an exhaustive report of the results obtained by the AGILE-GRID during the pointing mode period of operations starting in mid-2007 and ending in October 2009 (2.3 years). The AGILE-GRID turns out to be very effective in studying γ-ray sources above 100 MeV. The AGILE mission has been the first to operate in 2007 after the end of operations in 1996 of the EGRET γ-ray instrument on board the Compton Gamma-Ray Observatory. The AGILE-GRID was the first γ-ray detector capable of obtaining an unprecedentedly large FoV of 2.5 sr with much improved angular resolution compared with the previous generation of instruments. The pointing capability and observation strategy during the pointing phase of operations provided an excellent exposure of γ-ray sources for each individual pointing period.

The detector optimisation in the energy range 100 MeV to a few hundreds MeV (with significant capability in the energy range 50-100 MeV) is among the most relevant assets of the AGILE-GRID. Despite its relatively small size, the AGILE-GRID turns out to be very effective in detecting both short-lived and persistent γ-ray sources. This paper presents the 2AGL catalogue of persistent γ-ray sources detected by the AGILE-GRID during the pointing phase, which includes 175 high-confidence sources of both Galactic and extragalactic origin. Many source classes are represented: pulsars, PWNe, SNRs, compact objects, and blazars. In addition to confirming previously known relatively strong γ-ray sources, the 2AGL catalogue includes a substantial number of new sources compared to EGRET and 29 sources that are detected only by the AGILE-GRID.

A comparison with the Fermi-LAT instrument (operating since 2008 and overlapping in time during the second half of the pointing period considered in this work) has been performed. Different observing strategy, effective area, sky region exposures, and viewing angle during gamma-ray transient episodes may account for different results; see Appendix A for a direct comparison between the AGILE-GRID and Fermi-LAT visibility of some of the 2AGL sources detected only by AGILE-GRID.

Starting in 2010, AGILE has continued operations in orbit in spinning mode, therefore changing several important details concerning the exposure of γ-ray observations. An account of the γ-ray sources detected by the AGILE-GRID in spinning mode will be presented elsewhere.

Acknowledgements. The AGILE Mission is funded by the Italian Space Agency (ASI) with scientific and programmatic participation by the Italian Institute of Astrophysics (INAF) and the Italian Institute of Nuclear Physics (INFN). Investigation supported by the ASI grant I/089/06/2. We thank the ASI management for unfailing support during AGILE operations. We acknowledge the effort of ASI and industry personnel in operating the ASI ground station in Malindi (Kenya), and the data processing done at the ASI/SSDC in Rome: the success of AGILE scientific operations depend on the effectiveness of the data flow from Kenya to SSDC and on the data analysis and software management. We also acknowledge the use of innovative tools that are under development within the United Nations "Open Universe" initiative.

References

Abdalla, H., et al. 2018, A&A, 612, A13

Abdo, A. A., Ackermann, M., Ajello, M. et al. 2009, ApJ, 706, L1-L6

Abdo, A. A., Ackermann, M., Ajello, M. et al. 2009, ApJS, 183, 46-66

Abdo, A. A., Ackermann, M., et al. 2009, Science, 326, 1512

Abdo, A.A., Ackermann, M., Ajello, M. et al. 2010, ApJ, 723, 649-657

Abdo, A.A., Ackermann, M., Ajello, M. et al. 2010, ApJS, 188, 405-436

Abdo, A.A., Ackermann, M., Ajello, M. et al. 2011, Science, 331, 6018, 739-742

Acciari, V.A., Aliu, E., Arlen, T. et al. 2009, ApJ, 698, 133-137

Acciari, V.A., Aliu, E., Arlen, T. et al. 2009, ApJ, 707, 612-620

Acero, F., Ackermann, M., Ajello, M., Albert, A. et al. 2015, ApJS, 218, 2

Ackermann, M., Ajello, M., Allafort, A. et al. 2011, Science, 334, 1103

Ackermann, M., Ajello, M., Ballet, J. et al. 2012, Science, 335, 189

Ackermann, M., Ajello, M., Allafort, A. et al. 2013, Science, 339, 807-811

Ackermann, M., Ajello, M., Allafort, A. et al. 2013, ApJS, 209, 34

Ackermann, M., Ajello, M., Albert, A. et al. 2015, ApJ, 799, 86

Ajello, M., Atwood, W.B., Baldini, L. et al. 2017, ApJS, 232, 18

Aleksic, J., et al., 2012, A&A, 541, A13

Allafort, A., Baldini, L., Ballet, J., et al. 2013, ApJ, 777, L2

Aharonian, F., Akhperjanian, A., Bazer-Bachi, A. et al. 2008, A&A, 481, 401-410

Aharonian, F., Akhperjanian, A., Barres de Almeida, U. et al. 2008, A&A, 486, 829

Argan, A. et al. 2004, in Science Symposium Conference Record, Vol. 375, NSS-MIC IEEE, 371-375

Atwood, W. B., et al. 2009, ApJ, 697, 1071

Balbo, M., et al., 2010, A&A, 520, 111

Barbiellini, G., Bordignon, G., Fedel, G., et al. 2001, in American Institute of Physics Conference Series, Vol. 587, Gamma 2001: Gamma-Ray Astrophysics, ed. S. Ritz, N. Gehrels, & C. R. Shrader, 754

Brandt, T.J. fot the Fermi Collaboration 2013, AdSpR, 51, 247

Bulgarelli, A., et al. 2008, A&A, 489, L17-L20

Bulgarelli., A., et al. 2010, NIM A, 614, 213-226

Bulgarelli., A., Chen, A.W., et al. 2012, A&A, 540, A79

Bulgarelli, A., Tavani, M., Chen, A. W., et al. 2012, A&A, 538, A63

Bulgarelli., A., et al. 2014, ApJ, 781, 19

Calabretta, M. R., & Greisen, E. W. 2002, A&A, 395, 1077

Cardillo, M., Tavani, M., Giuliani, A. et al. 2014, A&A, 565, 74

Carosi, A., Antonelli, L.A., Giommi, P., Lucarelli, F. et al. 2015, ICRC, 34, 757

Cattaneo P.W., et al. 2011, NIMA, 630, 251-257

Cattaneo P.W., et al. 2018, ApJ, 861, 2

Chen, A.W., et al. 2008, A&A, 489, L37-L40

Chen, A. W., Piano, G., Tavani, M., et al. 2011, A&A, 525, A33

Chen, A.W., Argan, A., Bulgarelli, A. et al. 2013, A&A, 558, A37

Chi, X., Wolfendale, A.W., 1991, J. Phys. G, Vol. 17, No. 6, 987 - 998

, Clemens, D.P. 1985, ApJ, 295, 422

Cognard, I. and Backer, D. C. 2004, ApJ, 612, 125

Dame, T.M., Hartmann, D., Thaddeus, P. 2001 ApJ, 547, Issue 2, 792-813.

D'Ammando, F., et al. 2009, A&A, 508, 181-189

D'Ammando, F., et al. 2011, Advance in Space Research, 48, 76-87

D'Ammando, F., et al. 2011 A&A, 2011, 529, A145

Donnarumma, I., et al. 2009, ApJ707, 2

Donnarumma, I., et al., 2011, ApJ, 736, 2

Ebisawa, K., Bourban, G., Bodaghee, A., Mowlavi, N., Courvoisier, T.J.-L. 2003, A&A, 411, L59

Feroci, M., Costa, E., Soffitta, P., et al. 2007, NIM A, 581, 728

Fraija, N., & Araya, M. 2016, ApJ, 826, 31

P.E. Freeman, V. Kashyap, R. Rosner, D.Q. Lamb 2002, ApJS, 138, Issue 1, 185-218

Giuliani, A., Chen, A. W., Mereghetti, S., Pellizzoni, A., Tavani, M., Vercellone, S. 2004, Mem. SAIt Suppl., 5, 135

Giuliani, A., Cocco, V., Mereghetti, S., et al. 2006, NIM A, 568, 692

Giuliani, A., et al., 2009, A&A, 494, 509-513

Giuliani A., Tavani, M, Bulgarelli, A. et al. 2010, A&A, 516, 11-13

Giuliani, A., Cardillo, M., Tavani, M., et al. 2011, ApJ. 742, 30-34

Giommi, P., et al. 2008, A&A, 487, L49-L52

Giommi, P., et al. 2018, Proc. of the ESPI-UNISPACE+50 Conference, 2018 (arXiv:1805.08505)

Górski, K. M., Hivon, E., Banday, A. J., et al. 2005, ApJ, 622, 759

Hartman, R. C., Bertsch, D. L., Bloom, S. D., Chen, A. W., et al. 1999, ApJS, 123, 79H

Halpern, J. P. et al. 2008, ApJ, 688, L33-L36

Hamaguchi, K., Corcoran, M.F., Pittard, J.M. et al. 2018, Nature Astronomy, 2, 731-736

Hanabata, Y, Katagiri, H., Hewitt, J.W. et al. 2014, ApJ, 786, 145

Helene, O. 1983, NIM A, 212, 319

Jogler, T. & Funk, S. 2016, ApJ, 816, 100

Oh, K., Koss, M., Markwardt, C. B. et al. 2018, , ApJ, 235, 1

Kalberla, P.M.W., Burton, W.B., Hartmann, D., et al. 2005, A&A, 440, Issue 2, 775-782

Labanti, C. et al. 2009, NIM A, 598, 470-479

Liu, Q. Z., van Paradijs, J., van den Heuvel, E. P. J. 2006, A&A, 455, 1165-1168

Louis, A.K., Maas, D., Rieder, A. 1997, Wiley, ISBN 0471967920

Maxted, N.I., Rowell, G.P., Dawson, B.R. et al. 2013 MNRAS, 434, 2188-2201

Mattox, J. R., Bertsch, D. L., Chiang, J., et al. 1996, ApJ, 461, 396

Michelson, P. F., 2008, APS Meeting Abstracts, TSSP, L2002

Nolan, P.L., et al. 2012, ApJS, 199, 31

Pacciani, L., et al. 2009, A&A, 494, 49-61

Pacciani, L., et al., 2010, ApJ, 716, 2

Padovani, P. and Giommi, P., 1995, MNRAS, 277, 1477

Padovani, P. et al., 2018, MNRAS, 480, 192

Perotti, F., Fiorini, M., Incorvaia, S., Mattaini, E., & Sant Ambrogio, E. 2006, NIM A, 556, 228

Pellizzoni, A., Pilia, M., Possenti, A. et al. 2009, ApJ, 691, 2

Pellizzoni, A., Pilia, M., Possenti, A. et al. 2009, ApJ, 695, 1

Pellizzoni, A., Trois, A., et al. 2010, Science, 327, 5966, 663-665

Piano, G., Tavani, M., Vittorini, V., et al. 2012, A&A, 545, A110

Piano, G., Munar-Adrover, P., Verrecchia, F., Tavani, M., & Trushkin, S. A. 2017, ApJ, 839, 84

Piano, G., Cardillo, M., Pilia, M. et al., accepted to ApJ, 2019

Pilia, M., et al. 2010, ApJ, 723, 1

Pittori, C., Verrecchia, F., Chen, A.W., et al. 2009, A&A, 506, 1563

Pittori, C., 2013, NuPhS, 239, 104

Pittori, C., et al. 2018, ApJ, 856, 2

Pivato, G., Hewitt, J. W.; L. Tibaldo et al. 2013, ApJ, 779, 179

Pucella, G., et al. 2008, A&A, 491, L21-L24

Prest, M., Barbiellini, G., Bordignon, G., et al. 2003, NIM A, 501, 280

Rappoldi, A., Lucarelli, F., Pittori, C., et al. 2016, A&A, 587, A93

Sabatini, S., Tavani, M., Striani, E., et al. 2010, ApJ, 712, L10

Sabatini, S., Tavani, M., Pian, E. et al. 2011, NIM A, 630, 1

Sabatini, S., Tavani, M., Coppi, P., et al. 2013, ApJ, 766, 83

Sabatini, S., et al. 2015, ApJ, 809, 60

Striani, E., et al., 2010, ApJ, 718, 1

Striani, E., et al., 2011, ApJ, 741, 1

Striani, E., et al., 2013, ApJ, 765, 1

Strong, A.W., Moskalenko, I.V., Reimer, O. 2000, ApJ, 537, Issue 2, 763-784

Strong, A.W., et al. 2004, A&A, 422, L47

Tavani, M., Barbiellini, G., Argan, A. et al. 2008, NIM A, 588, 52

Tavani, M., Barbiellini, G., Argan, A. et al. 2009, A&A, 502, 995-1013

Tavani, M., Bulgarelli, A., Piano, G., et al. 2009, Nature, 462, 620

Tavani, M., et al. 2009, ApJ, 698, L142

Tavani, M., Giuliani, A., Chen, A.W. et al. 2010, Astrophys. J., 710, 151-155

Tavani, M., Bulgarelli, et al. 2011, Science, 331, 6018, 736-739

Vercellone, S., et al. 2008, ApJ, 676

Vercellone, S., et al. 2008, ApJ, 690, 1

Vercellone, S., et al., 2010, ApJ, 712, 1

Vercellone, S., et al., 2011, ApJ, 736, 2

Verrecchia, F., Pittori, C., Chen, A.W., et al. 2013, A&A, 558, A137

Vittorini, V., et al., 2009, ApJ, 706, 2

Vittorini, V., et al., 2011, ApJ, 732, 2

Wilks, S.S., 1938, Ann. Math. Stat., 9, 60-62

Yang, H.-J., et al., 2005, NIMA, 555, 370-385

Table 10: 2AGL catalogue sources. See Table 4 for a description of the columns

Name 2AGL	R.A.	Dec.	l	b	r	θ_a	θ_b	ϕ	SM	$\sqrt{TS}$	α	$\Delta\alpha$	F_γ	δF_γ	F_e	δF_e	VI	Exp	$Flag$	AGL assoc.	γ-ray assoc.	ID or assoc.	$Class$
J0007+7308	1.77	73.13	119.68	10.54	0.07	0.07	0.06	2.98	PC	26.2	1.29	0.22	41.6	4.2	67.2	6.9	0	6954 [268]		1AGL J0006+7311 1AGLR J0007+7307 AGL TeV J0006+727	TeV J0006+7259 3EG J0010+7309 3FGL J0007.0+7302 3FHL J0007.0+7303	LAT PSR J0007+7303	psr
J0032+0512c	8.09	5.21	114.11	-57.34	1.09	1.20	0.72	0.77	PL	4.0	2.18	0.27	6.6	1.9	10.7	3.0	0	1561 [60]	3,5		3FGL J0030.4+0451	PSR J0030+0451	psr
J0135+4754	23.72	47.90	130.43	-14.34	0.16	0.17	0.14	14.28	PL	10.7	1.98	0.11	12.1	2.1	19.5	3.4	0	4278 [165]		1AGLR J0135+4759	0FGL J0137.1+4751 3FHL J0136.9+4751	OC 457	FSRQ
J0217+0127	34.29	1.46	162.19	-54.74	0.59	0.68	0.39	6.79	PL	4.7	1.85	0.20	17.0	6.7	27.4	10.8		680 [26]	3		3FGL J0217.8+0143 3FHL J0217.8+0143	PKS 0215+015	fsrq
J0221+4250	35.17	42.84	139.86	-17.08	0.50	0.31	0.72	-39.70	PL	9.8	2.20	0.13	10.5	1.9	17.0	3.1	0	3499 [135]		1AGLR J0222+4305 AGL TeV J0222+430	TeV J0222+4302 TeV J0223+4259 3EG J0222+4253 3FGL J0218.1+4233 3FGL J0222.6+4301 3FHL J0218.3+4230 3FHL J0222.6+4302	3C 66A	BLL
J0221+6208c	35.20	62.13	133.17	1.05	0.45	0.36	0.57	-36.16	PL	7.6	2.33	0.14	9.4	1.8	15.2	3.0	0	4343 [168]			3FGL J0217.3+6209 3FGL J0220.1+6202c 3FGL J0221.8+6138c 3FGL J0223.6+6204 3FGL J0224.0+6235 3FGL J0225.8+6159		gunid
J0237+1653	39.29	16.88	156.21	-39.06	0.41	0.54	0.27	-6.12	PL	6.9	2.26	0.16	12.7	2.9	20.6	4.7		1303 [50]	2		3EG J0237+1635 3FGL J0238.6+1636 3FHL J0238.6+1637	AO 0235+164	bll
J0239+6120	39.85	61.34	135.51	1.13	0.09	0.09	0.09	61.28	PL	22.9	2.02	0.05	40.8	3.1	66.0	5.1	1	4189 [162]		1AGL J0242+6111 1AGLR J0240+6115 AGL TeV J0240+612	TeV J0240+6115 3FGL J0240.5+6113 3FHL J0240.5+6113	LS I +61 303	hmxb
J0247+6033	41.70	60.55	136.65	0.79	0.20	0.21	0.19	-14.72	PL	5.0	1.65	0.25	7.2	3.5	11.6	5.6	0	4106 [158]	3	1AGL J0242+6111	3FGL J0248.5+6022	PSR J0248+6021	psr
J0252+5038	43.02	50.63	141.69	-7.79	0.66	0.51	0.79	74.13	PL	6.1	2.45	0.19	5.6	1.4	9.1	2.3	0	3410 [132]	2		3FGL J0253.8+5104	NVSS J025357+510256	FSRQ
J0305+7452	46.26	74.87	131.46	14.25	0.25	0.20	0.32	17.00	PL	4.0	1.60	0.19	3.6	1.5	5.8	2.4	0	4596 [177]	3		3FGL J0308.0+7442	PSR J0307+7443	psr
J0320+4124	49.98	41.40	150.66	-13.34	0.29	0.22	0.37	34.48	PL	6.3	1.77	0.18	9.3	2.8	15.0	4.4	0	2908 [112]	2	1AGLR J0321+4137 AGL TeV J0319+415	TeV J0319+4130 3FGL J0319.8+4130	NGC 1275	rdg
J0328-1645	51.97	-16.75	205.17	-52.44	0.49	0.38	0.50	-43.56	PL	4.0	1.79	0.36	15.4	5.2	24.9	13.3		413 [16]	4		3FGL J0325.6-1648	RBS 0421	bll
J0429-3755	67.25	-37.92	240.69	-43.56	0.63	0.84	0.24	0.35	PL	4.7	1.92	0.28	15.9	6.7	25.7	10.8		509 [20]	3		3FGL J0428.6-3756	PKS 0426-380	BLL
J0442+0046	70.44	-0.77	197.53	-28.89	0.51	0.58	0.43	-54.59	PL	4.2	2.35	0.21	7.7	2.1	12.5	3.3		1123 [43]	2		3EG J0442-0033 3FGL J0442.6-0017	PKS 0440-00	fsrq
J0458-2323	74.38	-23.38	223.71	-34.79	0.28	0.23	0.31	-21.32	PL	6.3	1.95	0.21	20.0	6.3	32.3	10.3		635 [25]	2		3EG J0456-2338 3FGL J0457.0-2324	PKS 0454-234	fsrq
J0531+1334	82.87	13.57	191.41	-10.88	0.31	0.27	0.35	30.63	PL	4.1	1.84	0.18	11.1	3.7	17.8	5.9		1084 [42]	3		3EG J0530+1323 3FGL J0530.8+1330	PKS 0528+134	FSRQ
J0534+2205	83.57	22.09	184.46	-5.79	0.07	0.07	0.06	10.50	PL	56.9	2.32	0.03	183.6	5.5	296.8	8.9		1178 [45]		1AGL J0535+2205 AGL TeV J0534+220	TeV J0534+2200 3EG J0534+2200 3FGL J0534.5+2201i 3FGL J0534.5+2201s	Crab	PWN

Table 10: 2AGL catalogue sources. See Table 4 for a description of the columns

Name 2AGL	R.A.	Dec.	l	b	r	θ_a	θ_b	ϕ	SM	$\sqrt{TS}$	α	$\Delta\alpha$	F_γ	δF_γ	F_e	δF_e	VI	Exp	$Flag$	AGL assoc.	γ-ray assoc.	ID or assoc.	$Class$
J0538-4401	84.60	-44.01	249.99	-31.16	0.25	0.22	0.27	-34.51	PL	9.5	2.23	0.14	19.2	3.5	31.1	5.6		1073 [41]	2	1AGL J0538-4424 1AGLR J0539-4358	3EG J0540-4402 3FGL J0538.8-4405	PKS 0537-441	BLL
J0604-4005	91.04	-40.08	246.74	-25.66	0.20	0.20	0.19	-13.08	PL	4.4	1.14	0.55	5.8	3.4	9.4	5.5		1048 [40]	3		3FGL J0602.8-4016	SUMSS J060251-401845	bcu
J0617+2239e	94.25	22.66	188.95	3.02	0.11	0.10	0.11	15.54	PL	14.8	1.74	0.10	48.5	6.3	78.4	10.2		1317 [51]		1AGL J0617+2236 AGL TeV J0616+225	TeV J0616+2230 3EG J0617+2238 3FGL J0617.2+2234e	IC 443	SNR
J0634+1749	98.46	17.82	195.09	4.28	0.03	0.04	0.03	12.63	PS	76.4	1.71	0.09	426.2	9.8	688.7	15.8		1255 [48]		1AGL J0634+1748	TeV J0632+1722 3EG J0633+1751 3FGL J0633.9+1746	Geminga	PSR
J0634+0633	98.56	6.54	205.15	-0.82	0.28	0.32	0.25	21.28	PL	5.4	1.98	0.27	16.5	6.6	26.7	10.7		1103 [43]	3		3EG J0631+0642 3FGL J0633.7+0632	LAT PSR J0633+0632	psr
J0654+4514	103.59	45.23	171.22	19.37	0.54	0.50	0.57	-60.17	PL	6.2	2.39	0.19	8.1	2.1	13.1	3.4		1674 [65]	2	1AGL J0657+4554	3FGL J0654.4+4514	B3 0650+453	fsrq
J0714+3318	108.42	33.30	184.44	18.81	0.28	0.17	0.45	-54.48	PL	7.3	2.16	0.18	12.6	3.2	20.3	5.1		1435 [55]		1AGL J0714+3340 1AGLR J0713+3324			unid
J0723+7122	110.70	71.37	143.95	28.09	0.14	0.13	0.13	-48.91	PL	14.0	1.92	0.09	21.0	2.8	33.9	4.6	1	2728 [105]		1AGL J0722+7125 1AGLR J0723+7121 AGL TeV J0721+713	TeV J0721+7120 3EG J0721+7120 3FGL J0721.9+7120	S5 0716+714	BLL
J0730-1130	112.49	-11.49	227.56	3.16	0.25	0.23	0.28	22.21	PL	5.2	1.76	0.25	13.5	5.3	21.8	8.6		1199 [46]	3,5		3FGL J0730.2-1141	PKS 0727-11	fsrq
J0733-7655	113.23	-76.92	288.82	-24.07	0.34	0.30	0.36	6.72	PL	4.3	2.10	0.19	4.4	1.1	7.0	1.9	0	4077 [157]	3		3FGL J0734.3-7709	PKS 0736-770	bcu
J0819+4237	124.75	42.62	177.96	33.57	0.29	0.25	0.32	38.99	PL	4.3	1.34	0.20	5.8	2.5	9.3	4.1		1302 [50]	2,5		3FGL J0818.2+4223	S4 0814+42	bll
J0835-4514	128.80	-45.24	263.59	-2.84	0.02	0.02	0.02	37.84	PS	168.9	1.71	0.04	969.5	13.8	1566.9	22.4	0	2502 [97]		1AGL J0835-4509	3EG J0834-4511 3FGL J0835.3-4510	Vela PSR	PSR
J1015-5852	153.84	-58.86	283.92	-1.87	0.24	0.24	0.23	33.39	PL	7.7	2.04	0.13	19.2	3.8	31.0	6.2	0	3029 [117]		1AGLR J1018-5852 1AGLR J1022-5825 AGL TeV J1018-589	TeV J1016-5858 3EG J1013-5915 3FGL J1016.3-5858	PSR J1016-5857	PSR
J1020-5906	155.06	-59.09	284.57	-1.72	0.35	0.40	0.29	-34.50	PL	5.3	1.78	0.22	13.9	4.8	22.4	7.8	0	3040 [117]	2,5	1AGL J1022-5822 1AGLR J1018-5852 1AGLR J1022-5825 AGL TeV J1018-589	TeV J1018-5856 3EG J1013-5915 1FGL J1018.6-5856 3FGL J1018.9-5856	1FGL J1018.6-5856	hmxb
J1020-5752	155.11	-57.86	283.92	-0.67	0.25	0.29	0.22	18.40	PL	10.9	2.13	0.09	27.2	3.6	44.0	5.9	0	3004 [116]	2	1AGL J1022-5822 1AGLR J1022-5751 1AGLR J1022-5825	TeV J1023-5747 3FGL J1020.0-5749 3FGL J1021.9-5815c 3FGL J1023.1-5745	PSR J1019-5749	psr
J1029-5834	157.15	-58.57	285.21	-0.70	0.19	0.22	0.17	-3.66	PL	9.1	1.91	0.11	26.5	5.0	42.8	8.1	0	3058 [118]	3		3EG J1027-5817 3FGL J1028.4-5819	PSR J1028-5819	psr
J1045-5954	161.18	-59.91	287.66	-0.84	0.29	0.24	0.36	-22.94	PL	7.8	2.04	0.13	18.1	3.6	29.2	5.8	0	3210 [124]		1AGL J1043-5936 1AGLR J1044-5944	3FGL J1045.1-5941 3FGL J1047.3-6005	Eta Carinae	bin
J1045-5735	161.29	-57.59	286.63	1.23	0.25	0.24	0.27	10.19	PL	9.0	2.26	0.13	16.5	2.9	26.7	4.7		3079 [119]	5	1AGL J1043-5749	3FGL J1044.5-5737	LAT PSR J1044-5737	psr
J1048-5836	161.99	-58.61	287.43	0.50	0.17	0.16	0.18	47.01	PL	6.8	2.00	0.10	15.5	2.6	25.0	4.2	0	3169 [122]	2,5	1AGL J1043-5749 1AGLR J1048-5843	3EG J1048-5840 3FGL J1048.2-5832	PSR J1048-5832	psr
J1049-8010	162.32	-80.16	297.68	-18.56	0.43	0.40	0.47	-39.36	PL	5.5	2.15	0.21	5.1	1.6	8.2	2.6	0	4865 [188]	2		3FGL J1058.5-8003	PKS 1057-79	bll

Table 10: 2AGL catalogue sources. See Table 4 for a description of the columns

Name 2AGL	R.A.	Dec.	l	b	r	θ_a	θ_b	ϕ	SM	$\sqrt{TS}$	α	$\Delta\alpha$	F_γ	δF_γ	F_e	δF_e	VI	Exp	$Flag$	AGL assoc.	γ-ray assoc.	ID or assoc.	$Class$
J1052-6234	163.10	-62.57	289.70	-2.80	0.56	0.73	0.41	2.28	PL	6.3	2.40	0.18	8.7	2.1	14.0	3.4	0	3316 [128]	2		3FGL J1047.8-6216	PMN J1047-6217	BCU
J1059-5233	164.68	-52.54	286.13	6.61	0.10	0.11	0.09	39.05	PL	17.0	1.78	0.08	31.4	3.4	50.8	5.6	0	2972 [115]		1AGL J1058-5239	3EG J1058-5234 3FGL J1057.9-5227	PSR J1057-5226	psr
J1103-7747	165.71	-77.78	297.16	-16.14	0.74	0.54	0.98	-27.99	PL	4.4	2.01	0.24	5.6	2.2	9.1	3.6	0	4019 [155]	3		3FGL J1104.3-7736c	3FGL J1104.3-7736c	gunid
J1105+3813	166.21	38.21	179.76	65.10	0.25	0.19	0.22	-23.14	PL	6.1	1.57	0.27	13.5	5.6	21.8	9.0		891 [34]	2	1AGL J1104+3754 1AGLR J1105+3818 AGL TeV J1104+382	TeV J1104+3811 3EG J1104+3809 3FGL J1104.4+3812	Mkn 421	bll
J1111-6060	167.84	-61.00	291.10	-0.44	0.17	0.19	0.16	-7.15	PL	8.9	1.99	0.12	19.9	3.7	32.2	6.0	0	3355 [129]		1AGL J1108-6103 1AGLR J1107-6115 1AGLR J1112-6104	3FGL J1111.9-6058	PSR J1112-6103	psr
J1119-6443	169.64	-64.71	293.22	-3.61	0.73	0.45	1.03	0.66	PL	5.0	2.11	0.21	8.6	2.9	13.9	4.6	0	3451 [133]	3		3FGL J1123.2-6415	AT20G J112319-641735	bcu
J1120-6222	169.98	-62.37	292.54	-1.36	0.31	0.23	0.41	-3.77	PL	4.9	1.85	0.25	10.6	4.3	17.1	7.0	0	3394 [131]	2				unid
J1136-6045	174.10	-60.75	293.89	0.80	0.29	0.24	0.34	-5.30	PL	4.8	1.58	0.30	8.7	4.0	14.0	6.5	0	3293 [127]	2,5		3FGL J1135.2-6054	LAT PSR J1135-6055	psr
J1138-1724	174.48	-17.39	279.03	42.04	0.29	0.32	0.23	24.24	PL	5.7	2.05	0.22	10.5	3.6	17.0	5.7		1637 [63]	2			2FHL J1137.9-1710 5BZB J1137-1710	BLL
J1158+6009	179.51	60.15	134.71	55.74	0.85	0.81	0.64	48.02	PL	4.0	2.36	0.21	6.0	1.7	9.8	2.8		1249 [48]	3,5		3FGL J1154.3+6023	RX J1154.0+6022	fsrq
J1203-2701c	180.85	-27.02	289.91	34.63	0.44	0.59	0.31	-25.51	PL	4.6	2.36	0.26	5.1	1.9	8.3	3.0	0	2439 [94]	2,5				unid
J1204-6247	181.04	-62.78	297.56	-0.40	0.20	0.24	0.16	3.18	PL	5.3	1.38	0.28	9.4	3.7	15.2	6.0	0	3275 [126]	3		3FGL J1203.9-6243	PSR J1203-63	psr
J1228+4910	187.06	49.17	132.88	67.51	0.39	0.32	0.30	43.09	PL	4.0	1.30	0.60	5.2	4.0	8.4	6.5		859 [33]	3,5		3FGL J1228.7+4857	TXS 1226+492	FSRQ
J1228+0154	187.10	1.90	289.63	64.18	0.74	0.73	0.49	80.99	PL	5.0	2.32	0.24	11.3	3.6	18.2	5.8		669 [26]	2	1AGL J1228+0142	3EG J1229+0210 3FGL J1229.1+0202	3C 273	FSRQ
J1255-0543	193.86	-5.72	304.76	57.14	0.34	0.30	0.27	-15.97	PL	7.5	2.18	0.16	17.9	4.0	28.9	6.4		929 [36]	2	1AGL J1256-0549 AGL TeV J1256-057	TeV J1256-0547 3EG J1255-0549 3FGL J1256.1-0547	3C 279	FSRQ
J1312-3403	198.09	-34.05	307.87	28.62	0.30	0.31	0.27	15.07	PL	6.6	2.24	0.17	7.6	1.9	12.3	3.1	0	3032 [117]	2		3EG J1314-3431 0FGL J1311.9-3419		unid
J1324-4348	200.88	-43.80	309.04	18.69	0.93	0.65	1.27	-19.10	PL	5.4	2.69	0.25	3.9	1.3	6.3	2.1	0	3222 [124]	2	AGL TeV J1325-430	TeV J1325-4300 3EG J1324-4314 3FGL J1324.0-4330e 3FGL J1325.4-4301	Cen A	rdg
J1330-5606	202.41	-56.11	308.27	6.37	0.60	1.09	0.27	-4.81	PL	4.4	2.40	0.18	4.9	1.2	7.9	1.9	0	3418 [132]	3,5		3FGL J1328.9-5607	PMN J1329-5608	bcu
J1350+3037	207.47	30.62	51.67	76.75	0.65	0.53	0.38	43.71	PL	4.0	2.07	0.31	8.7	4.2	14.1	6.8		831 [32]	4		3FGL J1350.8+3035	B2 1348+30B	fsrq
J1402-8142	210.49	-81.70	305.58	-19.20	0.41	0.41	0.36	25.06	PL	4.4	2.20	0.26	4.3	1.7	7.0	2.7	0	4518 [174]	4				unid
J1407-6136c	211.69	-61.59	311.77	-0.02	0.83	0.62	1.10	18.72	PL	4.8	1.72	0.18	23.2	5.0	37.5	8.1	0	3757 [145]	2	1AGL J1412-6149	3EG J1410-6147 3FGL J1405.4-6119 3FGL J1409.7-6132 3FGL J1413.4-6205	3FGL J1405.4-6119 PSR J1410-6132 LAT PSR J1413-6205	gunid
J1418-6106	214.48	-61.10	313.19	0.03	0.09	0.09	0.09	-28.90	PL	14.7	1.83	0.07	45.1	5.2	72.9	8.4	0	3911 [151]		1AGL J1419-6055 1AGLR J1417-6108 AGL TeV J1418-609	TeV J1418-6058 3FGL J1418.6-6058	LAT PSR J1418-6058	psr

Table 10: 2AGL catalogue sources. See Table 4 for a description of the columns

Name 2AGL	R.A.	Dec.	l	b	r	θ_a	θ_b	ϕ	SM	$\sqrt{TS}$	α	$\Delta\alpha$	F_γ	δF_γ	F_e	δF_e	VI	Exp	$Flag$	AGL assoc.	γ-ray assoc.	ID or assoc.	$Class$
J1458-6055	224.57	-60.91	317.74	-1.74	0.23	0.21	0.25	36.49	PL	7.5	2.31	0.18	11.6	2.8	18.8	4.5	0	4226 [163]	2	AGL TeV J1459-608	TeV J1458-6052 3FGL J1456.7-6046 3FGL J1459.4-6053	LAT PSR J1459-6053 3FGL J1456.7-6046	unid
J1459-3542	224.70	-35.70	330.13	20.36	0.39	0.26	0.52	60.12	PL	5.6	2.09	0.18	6.3	1.9	10.2	3.1	1	3868 [149]	3		3EG J1500-3509 3FGL J1457.4-3539	PKS 1454-354	fsrq
J1507+1019	226.69	10.31	11.65	54.00	0.82	0.48	0.90	13.91	PL	5.4	2.15	0.20	18.3	5.5	29.7	8.9		520 [20]	2		3FGL J1504.4+1029	PKS 1502+106	FSRQ
J1509-5854	227.24	-58.90	319.89	-0.64	0.32	0.37	0.28	10.70	PL	6.5	2.21	0.18	12.7	3.2	20.6	5.2	0	4346 [168]	2	1AGL J1506-5859	3FGL J1509.4-5850	PSR J1509-5850	psr
J1513-0905	228.29	-9.08	351.38	40.10	0.10	0.10	0.09	-13.02	PL	25.0	2.19	0.05	55.7	4.0	90.1	6.4	1	1516 [58]		1AGL J1511-0908 1AGLR J1513-0906 AGL TeV J1512-091	TeV J1512-0906 3EG J1512-0849 3FGL J1512.8-0906	PKS 1510-089	FSRQ
J1517-5909	229.14	-59.15	320.60	-1.35	0.70	0.92	0.46	29.52	PL	5.4	2.39	0.22	8.0	2.3	12.9	3.7	0	4349 [168]	2,5		TeV J1513-5914 3FGL J1513.9-5908 3FGL J1514.0-5915e	PSR J1513-5908	PSR
J1602-4859	240.46	-48.98	331.97	2.86	0.50	0.48	0.52	-13.14	PL	5.2	2.93	0.30	4.2	1.0	6.7	1.6	0	4245 [164]	3		3FGL J1603.9-4903	PMN J1603-4904	bll
J1616-7716	243.97	-77.26	313.37	-18.76	0.63	0.66	0.57	-6.40	PL	4.3	2.19	0.24	3.9	1.4	6.2	2.3		4694 [181]	3,5		3FGL J1617.7-7717	PKS 1610-77	fsrq
J1622-4926	245.48	-49.44	334.05	0.29	0.28	0.25	0.31	13.82	PL	7.0	2.14	0.22	18.3	2.7	29.6	4.4	0	4564 [176]	2,5	1AGL J1624-4946	3FGL J1620.8-4928	PSR J1620-4927	psr
J1624-2406	246.12	-24.10	353.00	17.45	0.33	0.43	0.24	3.50	PL	6.0	2.15	0.19	9.7	3.0	15.7	4.8	0	2919 [113]	3		3EG J1627-2419 0FGL J1625.9-2423 1FGL J1623.5-2345c	0FGL J1625.9-2423 1FGL J1623.5-2345c	gunid
J1625-2021	246.32	-20.35	356.11	19.77	0.39	0.34	0.43	-4.23	PL	5.2	2.08	0.17	10.5	3.3	16.9	5.3	0	2230 [86]	4		1FGL J1626.2-2038	1FGL J1626.2-2038	gunid
J1626-2943	246.48	-29.72	348.90	13.44	0.28	0.30	0.25	-19.08	PL	5.5	2.10	0.00	7.9	1.6	12.8	2.6	1	3331 [129]	1,2		3EG J1625-2955 3FGL J1626.0-2951	PKS 1622-29	FSRQ
J1626-2511	246.54	-25.19	352.41	16.44	0.39	0.28	0.55	-32.02	PL	11.7	2.49	0.10	13.3	1.7	21.5	2.7	0	2920 [113]		1AGLR J1625-2531	3EG J1626-2519 3EG J1627-2419 3FGL J1625.7-2527	PKS 1622-253	fsrq
J1628-4448	247.01	-44.80	338.09	2.78	0.39	0.43	0.35	-43.83	PL	7.7	2.68	0.15	8.1	1.5	13.1	2.4	0	4147 [160]	2				unid
J1631-2039	247.64	-20.64	356.71	18.64	0.41	0.24	0.45	41.00	PL	5.9	2.13	0.19	9.1	2.7	14.7	4.3	0	2814 [109]					unid
J1631-2425	247.74	-24.41	353.77	16.13	0.45	0.51	0.38	-27.45	PL	5.9	2.13	0.18	9.6	2.8	15.5	4.6	0	2943 [114]	3		3EG J1627-2419 3FGL J1628.2-2431c	3FGL J1628.2-2431c	gunid
J1634-4734e	248.52	-47.57	336.79	0.12	0.29	0.25	0.34	-47.30	PL	12.2	2.49	0.11	21.1	2.5	34.1	4.0	0	4358 [168]		AGL TeV J1632-478 AGL TeV J1634-472	TeV J1632-4749 TeV J1634-4716 3FGL J1633.0-4746e 3FGL J1636.2-4734	HESS J1632-478	pwn
J1635-4704	248.85	-47.07	337.31	0.30	0.28	0.22	0.34	-54.25	PL	23.2	2.93	0.06	20.0	1.0	32.3	1.6	0	4174 [161]	2,5	1AGL J1639-4702 AGL TeV J1634-472	TeV J1634-4716 3EG J1639-4702 3FGL J1636.2-4709c	TeV J1634-4716 3FGL J1636.2-4709c	unid
J1636-4610	249.00	-46.16	338.05	0.83	0.35	0.33	0.36	8.89	PL	9.4	2.73	0.15	10.7	1.6	17.3	2.6	0	4183 [161]	2,5	1AGL J1639-4702			unid
J1639-4647	249.68	-46.79	337.89	0.06	0.18	0.14	0.22	-53.66	PL	9.7	2.31	0.12	21.7	3.3	35.1	5.4	0	4353 [168]		1AGL J1639-4702 AGL TeV J1640-465	3EG J1639-4702 3FGL J1638.6-4654	3FGL J1638.6-4654	spp
J1640-5050c	250.06	-50.83	335.04	-2.81	0.84	1.02	0.70	-30.25	PL	6.8	2.84	0.17	5.7	1.0	9.3	1.6	0	4376 [169]	3		3EG J1638-5155 3FGL J1643.6-5002	*3FGL J1643.6-5002	unid

Table 10: 2AGL catalogue sources. See Table 4 for a description of the columns

Name 2AGL	R.A.	Dec.	l	b	r	θ_a	θ_b	ϕ	SM	$\sqrt{TS}$	α	$\Delta\alpha$	F_γ	δF_γ	F_e	δF_e	VI	Exp	$Flag$	AGL assoc.	γ-ray assoc.	ID or assoc.	$Class$
J1649-5037	252.14	-50.61	336.07	-3.66	0.38	0.27	0.53	-39.23	PL	8.4	2.76	0.16	7.1	1.2	11.4	1.9	0	4359 [168]	2		3FGL J1650.2-5044	PMN J1650-5044	bcu
J1654-4704c	253.54	-47.06	339.40	-2.12	0.28	0.23	0.33	-20.50	PL	5.3	1.98	0.19	11.5	3.9	18.6	6.3	0	4329 [167]	2		3FGL J1652.2-4649 3FGL J1655.1-4644 3FGL J1655.7-4712	3FGL J1652.2-4649 3FGL J1655.1-4644 3FGL J1655.7-4712	gunid
J1703-5705	255.63	-57.08	332.25	-9.29	0.37	0.33	0.41	2.49	PL	5.1	2.68	0.36	3.2	1.2	5.1	1.9	0	4565 [176]	3,5		3FGL J1702.8-5656	3FGL J1702.8-5656	gunid
J1706-6212	256.38	-62.20	328.25	-12.61	0.48	0.45	0.51	50.22	PL	5.1	2.48	0.24	3.8	1.2	6.2	1.9	0	4630 [179]	2		3EG J1659-6251 3FGL J1703.6-6211	MRC 1659-621	fsrq
J1710-4429	257.47	-44.48	343.12	-2.70	0.05	0.04	0.05	-44.57	PC	43.5	1.51	0.10	154.0	8.5	248.9	13.7	0	4210 [162]		1AGL J1709-4428 AGL TeV J1708-443	3EG J1710-4439 3FGL J1709.7-4429	PSR J1709-4429	PSR
J1715-3815	258.80	-38.25	348.75	0.16	0.62	0.74	0.51	-14.48	PL	4.0	2.20	0.29	9.2	3.8	14.9	6.1	0	3771 [145]	3,5	AGL TeV J1713-382 AGL TeV J1714-385 AGL TeV J1718-374 AGL TeV J1718-385	TeV J1713-3811 TeV J1714-3834 TeV J1718-3833 3EG J1714-3857 3FGL J1714.5-3832 3FGL J1718.1-3825	CTB 37A	snr
J1718-0432	259.43	-4.54	17.57	18.46	0.52	0.69	0.37	-26.05	PL	6.9	2.63	0.21	5.9	1.4	9.5	2.2	0	3011 [116]	2		3EG J1719-0430 3FGL J1720.3-0428	3FGL J1720.3-0428	gunid
J1720-3859	259.96	-38.99	348.67	-1.01	0.45	0.40	0.50	-45.57	PL	5.0	1.96	0.21	12.9	4.5	20.9	7.2	0	3810 [147]	3,5	AGL TeV J1718-385	TeV J1718-3833 3FGL J1721.8-3919	3FGL J1721.8-3919	gunid
J1720-3328	260.04	-33.47	353.23	2.09	0.52	0.49	0.55	14.79	PL	4.0	2.35	0.24	7.5	2.7	12.2	4.3	0	3416 [132]	3,5		3EG J1718-3313 3FGL J1717.8-3342	TXS 1714-336	bll
J1731-0527	262.80	-5.45	18.53	15.11	0.46	0.55	0.37	42.67	PL	6.0	2.09	0.18	8.6	2.7	13.9	4.3	0	3271 [126]	3				unid
J1733-3130	263.22	-31.50	356.37	0.96	0.18	0.17	0.20	-18.31	PL	9.4	2.12	0.10	16.6	2.2	42.3	6.9	0	3306 [128]	2		3FGL J1732.5-3130	LAT PSR J1732-3131	psr
J1736-7819	264.06	-78.32	314.94	-22.86	0.37	0.36	0.34	18.19	PL	5.1	2.40	0.26	3.7	1.3	6.0	2.1	0	4887 [189]	2		3EG J1720-7820	3EG J1720-7820	unid
J1737-3206	264.17	-32.10	356.30	-0.04	0.22	0.16	0.29	-3.96	PL	10.7	2.15	0.10	8.5	1.3	54.8	8.4	0	3335 [129]		1AGL J1736-3235	3EG J1734-3232 3FGL J1737.3-3214c	3FGL J1737.3-3214c	spp
J1739-2837	264.74	-28.62	359.50	1.41	0.35	0.34	0.37	8.81	PL	9.9	2.48	0.12	19.0	2.9	30.8	4.7	0	3139 [121]			3EG J1736-2908 3FGL J1736.5-2839 3FGL J1740.5-2843	3FGL J1736.5-2839 3FGL J1740.5-2843	gunid
J1740-3013	265.02	-30.22	358.28	0.35	0.25	0.34	0.18	-12.78	PL	8.1	1.97	0.13	27.4	5.6	44.2	9.1	0	3264 [126]	2	AGL TeV J1741-302	TeV J1741-3012	HESS J1741-302	unid
J1741+5126	265.23	51.43	78.67	31.64	0.96	1.38	0.62	-11.60	PL	4.4	2.52	0.23	3.1	1.1	5.0	1.7	0	3627 [140]	2		3EG J1738+5203 3FGL J1740.3+5211	4C +51.37	FSRQ
J1743-2051	265.71	-20.85	6.58	4.76	0.55	0.62	0.39	-4.54	PL	4.9	1.83	0.21	10.0	3.6	16.2	5.9	0	3214 [124]	3		3EG J1741-2050 3FGL J1741.9-2054	LAT PSR J1741-2054	psr
J1743-2613c	265.79	-26.22	2.03	1.88	0.39	0.36	0.43	25.58	PL	8.6	2.68	0.16	11.3	2.0	18.2	3.3		3091 [119]					unid
J1744-3045	265.89	-30.76	358.21	-0.57	0.12	0.13	0.11	-0.71	PL	12.0	1.96	0.08	40.4	5.4	65.3	8.8	0	3285 [127]	2	1AGL J1746-3017	3FGL J1744.7-3043	3FGL J1744.7-3043	gunid
J1746-2921	266.48	-29.35	359.68	-0.27	0.15	0.18	0.12	8.47	PL	6.2	1.49	0.15	24.2	6.1	39.2	9.9	0	3101 [120]	2,5	1AGL J1746-3017	0FGL J1746.0-2900		unid
J1746-2832	266.55	-28.54	0.41	0.10	0.10	0.11	0.09	-41.96	PL	21.6	2.12	0.05	76.1	5.3	123.0	8.5	0	3214 [124]			3FGL J1747.0-2828	3FGL J1747.0-2828	gunid
J1747-3232	266.68	-32.53	357.05	-2.07	0.47	0.40	0.54	76.99	PL	6.4	2.08	0.15	15.9	3.9	25.8	6.2	0	3350 [129]			3FGL J1746.8-3240	LAT PSR J1746-3239	psr

Table 10: 2AGL catalogue sources. See Table 4 for a description of the columns

Name 2AGL	R.A.	Dec.	l	b	r	θ_a	θ_b	ϕ	SM	$\sqrt{TS}$	α	$\Delta\alpha$	F_γ	δF_γ	F_e	δF_e	VI	Exp	$Flag$	AGL assoc.	γ-ray assoc.	ID or assoc.	$Class$
J1748-2950	267.11	-29.83	359.55	-0.99	0.24	0.16	0.35	72.05	PL	8.1	1.75	0.11	29.3	5.9	47.4	9.5	0	3220 [124]	2	1AGL J1746-3017	3FGL J1747.2-2958	PSR J1747-2958	psr
J1749-2448	267.16	-24.81	3.88	1.56	0.31	0.25	0.38	19.76	PL	7.5	2.35	0.14	15.0	3.0	24.2	4.8	0	3196 [123]	2	AGL TeV J1747-248	TeV J1747-2448 3FGL J1748.0-2447	Terzan 5	glc
J1754-2626	268.45	-26.44	3.07	-0.27	0.42	0.66	0.18	-3.44	PL	6.5	2.67	0.23	9.6	2.2	15.5	3.6	0	3142 [121]	2				unid
J1760+7821	269.97	78.36	109.92	29.12	0.58	0.77	0.39	84.71	PL	4.0	2.10	0.00	3.3	0.9	5.3	1.5	0	5622 [217]	1,4		3FGL J1800.5+7827	S5 1803+784	bll
J1801-2334	270.17	-23.57	6.34	-0.18	0.19	0.18	0.20	24.71	LP	7.5	3.38	0.46	35.8	10.2	57.8	16.5	0	3852 [149]	2	1AGL J1803-2258 1AGL J1801-2317 AGL TeV J1801-233	3EG J1800-2338 3FGL J1801.3-2326e	W28	SNR
J1803-3935	270.67	-39.59	352.52	-8.38	0.20	0.17	0.24	-36.81	PL	9.9	2.20	0.13	13.7	2.4	22.1	3.9	0	3629 [140]		1AGLR J1803-3941	3EG J1800-3955 3FGL J1802.6-3940	PMN J1802-3940	FSRQ
J1804-2153	270.91	-21.89	8.14	0.06	0.42	0.51	0.27	43.65	PL	5.6	2.10	0.00	17.6	3.3	28.5	5.3	0	3362 [130]	1,2	1AGL J1805-2143 1AGLR J1805-2149 AGL TeV J1804-216	TeV J1804-2143 3FGL J1803.1-2147	PSR J1803-2149	psr
J1810-2339	272.51	-23.65	7.31	-2.09	0.10	0.11	0.08	28.57	PL	14.4	1.80	0.09	41.0	5.4	66.3	8.8	0	3376 [130]		1AGL J1809-2332 1AGLR J1809-2333	3EG J1809-2328 3FGL J1809.8-2332	PSR J1809-2332	psr
J1813-1245	273.36	-12.75	17.26	2.44	0.16	0.20	0.13	-13.23	PL	12.6	2.25	0.09	27.1	3.5	43.8	5.6	0	3399 [131]			3EG J1812-1316 3FGL J1813.4-1246	LAT PSR J1813-1246	psr
J1820-1150c	274.95	-11.83	18.81	1.51	0.66	0.79	0.26	44.49	PL	6.1	2.55	0.26	10.0	3.8	16.2	6.2	0	3383 [131]	2				unid
J1822-1336	275.42	-13.61	17.46	0.27	0.34	0.39	0.30	-48.47	PL	5.0	2.33	0.38	14.4	6.9	23.2	11.2	0	3412 [132]	2		3EG J1823-1314 3FGL J1819.5-1345 3FGL J1823.2-1339	3FGL J1819.5-1345 3FGL J1823.2-1339	gunid
J1823-1504	275.63	-15.06	16.27	-0.60	0.19	0.19	0.18	-11.26	PL	5.7	1.91	0.20	19.3	6.2	31.2	10.1	0	3454 [133]	2	1AGL J1823-1454 1AGLR J1822-1456	3EG J1824-1514 0FGL J1821.4-1444	0FGL J1821.4-1444	unid
J1826-1438	276.46	-14.63	17.03	-1.10	0.33	0.42	0.21	26.44	PL	8.4	2.25	0.14	21.6	4.1	34.9	6.7	0	3430 [132]	2,5	1AGL J1823-1454 1AGLR J1822-1456 AGL TeV J1826-148	TeV J1826-1449 3EG J1824-1514 3FGL J1826.2-1450	LS 5039	hmxb
J1826-1257	276.52	-12.94	18.55	-0.37	0.15	0.11	0.21	11.45	PL	9.0	1.71	0.11	31.8	6.2	51.4	10.0	0	3486 [135]	2	1AGL J1826-1246 1AGL J1827-1227	3EG J1826-1302 3FGL J1826.1-1256	LAT PSR J1826-1256	psr
J1829+0549	277.13	5.82	35.53	7.74	0.58	0.79	0.41	2.89	PL	4.5	2.09	0.25	6.0	2.4	9.7	3.9	0	4227 [163]	3,5		3FGL J1830.1+0617	TXS 1827+062	fsrq
J1829-1450	277.31	-14.83	17.23	-1.92	0.25	0.18	0.36	28.05	PL	5.9	2.01	0.16	16.4	4.3	26.5	7.0	0	3475 [134]	2		3FGL J1827.3-1446 3FGL J1829.2-1504	3FGL J1827.3-1446 3FGL J1829.2-1504	gunid
J1833-2104	278.37	-21.06	12.15	-5.68	0.21	0.18	0.23	9.91	PL	13.0	2.39	0.10	17.7	2.2	28.6	3.6	0	3417 [132]	2	1AGLR J1833-2057	3EG J1832-2110 3FGL J1833.6-2103	PKS 1830-211	FSRQ
J1836+5924	279.08	59.40	88.85	24.98	0.05	0.05	0.05	40.49	PC	41.3	1.21	0.16	71.8	5.2	116.1	8.4	0	5927 [229]		1AGL J1836+5923 1AGL J1836+5923**	3EG J1835+5918 3FGL J1836.2+5925	LAT PSR J1836+5925	psr
J1838-0623c	279.40	-6.38	25.67	0.16	0.83	0.64	1.06	14.40	PL	8.2	2.61	0.15	13.1	2.1	21.2	3.4	0	3735 [144]		1AGLR J1839-0550 AGL TeV J1837-069	TeV J1837-0656 TeV J1840-0533 3EG J1837-0606 3FGL J1834.8-0630c 3FGL J1836.5-0655e 3FGL J1837.9-0607 3FGL J1838.9-0646 3FGL J1839.3-0552	3FGL J1834.8-0630c HESS J1837-069 PSR J1837-0604 3FGL J1838.9-0646 3FGL J1839.3-0552	gunid

Table 10: 2AGL catalogue sources. See Table 4 for a description of the columns

Name 2AGL	R.A.	Dec.	l	b	r	θ_a	θ_b	ϕ	SM	$\sqrt{TS}$	α	$\Delta\alpha$	F_γ	δF_γ	F_e	δF_e	VI	Exp	$Flag$	AGL assoc.	γ-ray assoc.	ID or assoc.	$Class$
J1839-0544	279.79	-5.73	26.44	0.11	0.15	0.12	0.20	-79.83	PL	15.3	2.21	0.07	39.6	3.9	64.1	6.4	0	3883 [150]		1AGLR J1839-0550	TeV J1840-0533 3FGL J1838.9-0537 3FGL J1839.3-0552	LAT PSR J1838-0537	psr
J1843-1102	280.69	-11.03	22.13	-3.10	0.52	0.43	0.60	6.70	PL	4.9	3.19	0.20	2.3	0.5	3.8	0.8	0	3446 [133]	3,5		3FGL J1843.6-1114	PSR J1843-1113	psr
J1846-1219	281.60	-12.32	21.38	-4.48	0.37	0.27	0.49	-19.37	PL	5.8	2.94	0.22	3.9	0.9	6.3	1.5		3422 [132]	4		3FGL J1844.7-1224	3FGL J1844.7-1224	gunid
J1847-0157	281.82	-1.95	30.73	0.04	0.27	0.32	0.23	-44.56	PL	4.9	2.10	0.00	14.4	3.1	23.3	5.0	0	4136 [160]	1,2	AGL TeV J1848-017	TeV J1848-0147 3FGL J1848.4-0141	3FGL J1848.4-0141	gunid
J1849+6706	282.15	67.10	97.49	25.11	0.11	0.10	0.12	-31.32	PL	16.7	2.03	0.07	16.1	1.8	26.1	2.9	0	5626 [217]		1AGL J1846+6714 1AGLR J1848+6709	3FGL J1849.2+6705	S4 1849+67	FSRQ
J1856+0119e	284.07	1.32	34.66	-0.48	0.11	0.10	0.12	26.81	LP	13.2	2.54	0.30	56.8	8.2	91.8	13.2	0	5496 [212]		1AGL J1855+0122 1AGL J1856+0122	3EG J1856+0114 3FGL J1855.9+0121e	W44	SNR
J1857+0015	284.22	0.25	33.78	-1.10	0.27	0.30	0.24	-13.11	PL	4.7	1.77	0.21	11.7	4.4	18.9	7.1	0	4299 [166]	3				unid
J1859+0219	284.68	2.31	35.82	-0.57	0.29	0.37	0.22	57.66	PL	4.2	1.70	0.24	11.5	5.0	18.6	8.1	0	4445 [171]	3		TeV J1858+0205 3FGL J1857.9+0210	3FGL J1857.9+0210	gunid
J1900+0432	285.09	4.53	37.99	0.08	0.40	0.38	0.43	64.03	PL	8.0	2.65	0.19	10.2	1.9	16.5	3.1	0	4284 [165]	2	1AGL J1901+0429	3FGL J1900.3+0411c	3FGL J1900.3+0411c	gunid
J1905+0656	286.14	6.93	40.59	0.26	0.72	0.65	0.79	2.49	PL	4.4	2.63	0.23	5.5	1.3	8.8	2.1	0	4362 [168]	3,5	1AGL J1908+0614 AGL TeV J1907+062	3EG J1903+0550 3FGL J1902.6+0655 3FGL J1906.6+0720	3FGL J1902.6+0655 3FGL J1906.6+0720	gunid
J1909+0559	287.14	5.98	40.20	-1.06	0.20	0.24	0.16	-33.11	PL	10.6	2.21	0.10	21.5	3.1	34.7	5.0	0	4560 [176]	2	1AGL J1908+0614 AGL TeV J1907+062	3FGL J1907.9+0602	LAT PSR J1907+0602	psr
J1910-0637	287.39	-6.62	29.07	-7.03	0.38	0.44	0.33	7.91	PL	4.9	2.33	0.25	6.2	2.2	10.0	3.5	0	4082 [157]	3				unid
J1911+0907	287.74	9.12	43.26	-0.14	0.26	0.25	0.28	-29.59	PL	5.4	1.64	0.20	11.6	4.1	18.8	6.5	0	4693 [181]	3,5	AGL TeV J1911+090	TeV J1911+0905 3FGL J1910.9+0906	W49B	snr
J1913+0050	288.19	0.83	36.11	-4.36	0.65	0.60	0.71	51.26	PL	6.1	2.96	0.28	3.2	0.9	5.2	1.4	0	4184 [161]	3				unid
J1913-1928	288.19	-19.47	17.64	-13.29	0.65	0.73	0.57	14.22	PL	5.0	2.29	0.19	6.0	1.7	9.7	2.8	0	3404 [131]	2		3EG J1911-2000 3FGL J1911.2-2006 3FGL J1911.4-1908	PKS B1908-201 PMN J1911-1908	unid
J1922-2115	290.57	-21.26	16.88	-16.06	0.39	0.40	0.38	32.84	PL	5.1	1.60	0.25	8.0	3.1	12.9	4.9	0	2961 [114]	3		3EG J1921-2015 3FGL J1923.5-2104	TXS 1920-211	fsrq
J1924+1416	290.91	14.27	49.27	-0.48	0.21	0.18	0.25	-34.34	PL	7.7	1.96	0.12	16.7	3.5	27.0	5.7	0	4844 [187]	3	1AGL J1922+1403 AGL TeV J1923+141	TeV J1922+1411 3FGL J1923.2+1408e	W51C	snr
J1927-4318	291.73	-43.30	355.07	-24.37	0.55	0.47	0.60	-22.66	PL	4.6	1.87	0.27	6.3	2.8	10.3	4.6	0	3316 [128]	2				unid
J1938-7744	294.53	-77.73	316.69	-28.94	1.13	0.61	1.08	-90.00	PL	4.6	2.46	0.26	3.4	1.1	5.5	1.7	0	3977 [153]	2		3FGL J1925.8-7826	3FGL J1925.8-7826	gunid
J1953+3258	298.26	32.97	68.85	2.86	0.12	0.13	0.11	18.86	PL	10.6	1.62	0.13	15.0	3.0	24.3	4.8	0	5074 [196]			3FGL J1952.9+3253	PSR J1952+3252	psr
J1957+5017	299.20	50.29	84.28	11.00	0.35	0.26	0.44	59.38	PL	4.7	1.55	0.31	4.0	1.9	6.4	3.1	0	5853 [226]	3,5		3FGL J1957.7+5034	LAT PSR J1957+5033	psr
J1958+6519	299.54	65.32	98.06	17.94	0.27	0.21	0.34	-36.84	PL	4.6	1.76	0.36	3.8	2.3	6.2	3.7	0	6245 [241]	3		TeV J1959+6508 3FGL J2000.0+6509	1ES 1959+650	bll
J1958+2853	299.62	28.88	65.96	-0.26	0.19	0.17	0.22	-7.48	PL	7.4	1.85	0.13	12.5	2.8	20.2	4.6	0	5294 [204]	3		3EG J1958+2909 3FGL J1958.6+2845	LAT PSR J1958+2846	psr

Table 10: 2AGL catalogue sources. See Table 4 for a description of the columns

Name 2AGL	R.A.	Dec.	l	b	r	θ_a	θ_b	ϕ	SM	$\sqrt{TS}$	α	$\Delta\alpha$	F_γ	δF_γ	F_e	δF_e	VI	Exp	$Flag$	AGL assoc.	γ-ray assoc.	ID or assoc.	$Class$
J2002+4355	300.58	43.91	79.20	6.95	0.35	0.21	0.55	-41.69	PL	5.2	1.79	0.25	6.1	2.5	9.9	4.1	0	6236 [241]	3	AGL TeV J2001+438	TeV J2001+4353 3FGL J2001.1+4352	MG4 J200112+4352	bll
J2005+7225	301.23	72.41	105.11	20.48	0.67	0.42	0.84	-8.81	PL	4.1	2.18	0.42	3.2	0.9	5.2	1.4	0	6033 [233]	3,5		3FGL J2010.3+7228	4C +72.28	bll
J2020+3824	305.06	38.40	76.40	1.13	0.51	0.62	0.41	-35.26	PL	9.5	2.61	0.17	9.9	1.1	15.9	1.8	0	5600 [216]	5		3FGL J2022.2+3840	3FGL J2022.2+3840	spp
J2021+3654	305.25	36.90	75.25	0.15	0.08	0.08	0.09	13.87	PC	21.3	1.38	0.30	70.9	7.9	114.6	12.8	0	6291 [243]		1AGL J2021+3652 1AGLR J2021+3653 AGL TeV J2019+368	TeV J2019+3648 3EG J2021+3716 3FGL J2021.1+3651	PSR J2021+3651	PSR
J2021+4029	305.35	40.48	78.24	2.12	0.05	0.05	0.05	-3.94	PC	43.8	1.76	0.09	119.3	5.9	192.8	9.6	0	6037 [233]		1AGL J2022+4032 1AGLR J2021+4030	3EG J2020+4017 3FGL J2021.0+4031e 3FGL J2021.5+4026	Gamma Cygni LAT PSR J2021+4026	SNR
J2025+3352	306.27	33.86	73.24	-2.27	0.21	0.19	0.23	34.94	PL	8.4	2.11	0.13	12.3	2.5	19.8	4.0	0	5560 [215]			3EG J2027+3429 3FGL J2025.2+3340	B2 2023+33	BCU
J2027-0740	306.66	-7.67	36.94	-24.63	0.21	0.18	0.24	-36.49	PL	12.0	2.38	0.10	12.2	1.8	19.7	2.8	1	4109 [159]	2	1AGL J2026-0732 1AGLR J2027-0747	3EG J2025-0744 3FGL J2025.6-0736	PKS 2023-07	FSRQ
J2029+4403	307.21	44.05	81.96	3.06	0.22	0.21	0.22	-35.56	PL	6.2	1.93	0.18	10.0	3.0	16.1	4.9	0	5991 [231]	5				unid
J2032+4135	308.08	41.59	80.34	1.09	0.25	0.29	0.21	1.74	PL	8.6	2.17	0.12	15.7	2.7	25.4	4.4	0	5914 [228]	2	1AGL J2032+4102 1AGLR J2031+4130 AGL TeV J2032+415	TeV J2031+4133 3EG J2033+4118 3FGL J2032.2+4126	LAT PSR J2032+4127	psr
J2033+4060	308.21	41.00	79.92	0.66	0.22	0.21	0.24	-11.17	PL	8.2	2.00	0.11	17.0	3.1	27.4	5.1	0	5939 [229]		1AGL J2032+4102 1AGLR J2033+4057 AGL TeV J2032+415	TeV J2031+4040 3EG J2033+4118 2FGL J2032.1+4049	Cyg X-3	HMXB
J2044+5012e	311.00	50.21	88.44	4.69	0.25	0.33	0.18	-32.40	PL	6.2	1.97	0.17	8.0	2.3	12.9	3.7	0	6221 [240]	3,5		3FGL J2045.2+5026e	HB 21	snr
J2055+2521	313.75	25.36	70.32	-12.57	0.24	0.20	0.28	-49.54	PL	5.3	1.77	0.32	5.6	3.0	9.0	4.9	0	5310 [205]	3		2FGL J2055.8+2539		unid
J2057-4711	314.15	-47.19	352.67	-40.44	0.33	0.42	0.23	24.45	PL	6.0	2.05	0.19	8.0	2.5	13.0	4.1	0	2544 [98]	3		3EG J2055-4716 3FGL J2056.2-4714	PKS 2052-47	fsrq
J2144+1730	325.98	17.49	71.98	-26.30	0.62	0.45	0.80	-1.03	PL	4.4	2.11	0.25	4.2	1.7	6.8	2.7	0	4679 [181]	3		3FGL J2143.5+1744	OX 169	fsrq
J2147+0951	326.84	9.85	66.15	-32.06	0.43	0.49	0.35	26.92	PL	5.0	2.34	0.21	4.6	1.4	7.4	2.2	0	4399 [170]	2		3FGL J2147.2+0929	PKS 2144+092	fsrq
J2157-3015	329.32	-30.26	17.62	-51.91	0.41	0.24	0.56	27.42	PL	4.9	1.74	0.24	16.6	7.0	26.9	11.3		765 [30]	3	AGL TeV J2158-302	TeV J2158-3013 3EG J2158-3023 3FGL J2158.8-3013	PKS 2155-304	bll
J2202+4214	330.42	42.23	92.41	-10.36	0.18	0.17	0.19	-19.10	PL	7.8	1.97	0.15	7.5	1.7	12.0	2.8	0	6275 [242]	3	AGL TeV J2202+422	TeV J2202+4216 3EG J2202+4217 3FGL J2202.7+4217	BL Lacertae	BLL
J2203+1739	330.84	17.64	75.82	-29.46	0.21	0.24	0.18	25.11	PL	5.5	1.64	0.24	5.7	2.1	9.2	3.5	0	4678 [180]	3		3FGL J2203.4+1725	PKS 2201+171	fsrq
J2206-1044	331.60	-10.73	47.73	-47.92	0.52	0.43	0.49	5.35	PL	4.3	2.30	0.32	6.6	3.0	10.7	4.8	1	1778 [69]	3				unid
J2227+6418	336.76	64.29	108.05	5.68	0.62	0.68	0.56	-13.91	PL	7.3	2.75	0.16	3.9	0.7	6.4	1.2		6109 [236]	2				unid
J2228-0818	336.88	-8.30	55.09	-51.12	0.25	0.25	0.20	6.07	PL	7.3	2.52	0.21	8.1	1.9	13.0	3.1	1	1912 [74]					unid
J2230+6113	337.58	61.22	106.77	2.86	0.19	0.15	0.26	1.74	PL	11.0	2.02	0.10	14.9	2.3	24.1	3.7	1	6284 [242]		1AGL J2231+6109 AGL TeV J2227+608	TeV J2227+6052 TeV J2228+6110 3EG J2227+6122 3FGL J2229.0+6114	PSR J2229+6114	PSR

Table 10: 2AGL catalogue sources. See Table 4 for a description of the columns

Name 2AGL	R.A.	Dec.	l	b	r	θ_a	θ_b	ϕ	SM	$\sqrt{TS}$	α	$\Delta\alpha$	F_γ	δF_γ	F_e	δF_e	VI	Exp	$Flag$	AGL assoc.	γ-ray assoc.	ID or assoc.	$Class$
J2232+1132	338.02	11.53	77.15	-38.65	0.39	0.48	0.28	7.13	PL	5.0	1.82	0.24	5.8	2.3	9.3	3.7	0	4256 [164]	3		3EG J2232+1147 3FGL J2232.5+1143	CTA 102	fsrq
J2238+5900	339.57	59.00	106.51	0.44	0.32	0.38	0.28	18.85	PL	4.3	1.70	0.27	5.5	2.5	8.8	4.0	0	6238 [241]	3		3FGL J2238.4+5903	LAT PSR J2238+5903	psr
J2247+1558	341.70	15.96	84.19	-37.36	0.42	0.45	0.34	-25.29	PL	9.5	2.76	0.15	6.1	1.0	9.8	1.5	0	4133 [159]	2,5		3EG J2243+1509 3FGL J2246.2+1547	NVSS J224604+154437	bcu
J2254+1609	343.50	16.16	86.13	-38.18	0.06	0.05	0.05	84.94	PL	55.6	2.21	0.03	75.1	2.4	121.4	3.9	1	4266 [165]		1AGL J2254+1602 1AGLR J2254+1609	3EG J2254+1601 3FGL J2254.0+1608	3C 454.3	FSRQ
J2303+2120	345.78	21.33	91.79	-34.91	0.46	0.35	0.54	-7.50	PL	4.3	2.44	0.24	3.2	1.1	5.1	1.8	0	4604 [178]	2				unid
J2303+4425	345.84	44.41	103.37	-14.31	0.32	0.40	0.24	67.62	PL	4.4	1.56	0.25	3.7	1.5	6.0	2.5	0	5852 [226]	3,5		3FGL J2302.7+4443	PSR J2302+4442	psr
J2332+8215c	352.99	82.25	120.14	19.82	0.62	0.85	0.43	-41.78	PL	5.8	2.70	0.75	2.4	0.6	3.8	0.9	0	6964 [269]	3		3FGL J2355.5+8154		unid
J2336+8009	354.03	80.15	119.61	17.76	0.36	0.27	0.46	28.77	PL	6.2	2.24	0.19	4.6	1.3	7.5	2.1	0	6186 [239]	5		3FGL J2340.7+8016	1RXS J234051.4+801513	bll

Table 11: Spectral information of 2AGL catalogue sources. See Table 9 for a description of the columns.

									0.1 – 0.3 GeV		0.3 – 1 GeV		1 – 3 GeV		3 – 10 GeV				
Name 2AGL	$\sqrt{TS}$	SM	α	$\Delta\alpha$	E_c	ΔE_c	β	$\Delta\beta$	F_1	$\sqrt{TS}_1$	F_2	$\sqrt{TS}_2$	F_3	$\sqrt{TS}_3$	F_4	$\sqrt{TS}_4$	ID or ass.	Flag	Class.
J0007+7308	26.2	PC	1.29	0.22	2003.9	1010.3			$16.01^{+2.23}_{-2.17}$	8.3	$15.50^{+1.04}_{-1.01}$	22.0	$6.45^{+0.96}_{-0.89}$	11.1	$2.44^{+0.99}_{-0.83}$	4.1	LAT PSR J0007+7303		psr
J0032+0512c	4.0	PL	2.18	0.27					< 8.09	1.7	$1.69^{+0.60}_{-0.55}$	3.6	< 0.90	1.3	< 0.78	0.0	PSR J0030+0451	3,5	psr
J0135+4754	10.7	PL	1.98	0.11					$6.15^{+1.57}_{-1.52}$	4.3	$3.41^{+0.51}_{-0.48}$	9.0	$0.67^{+0.30}_{-0.26}$	3.2	< 1.98	2.2	OC 457		FSRQ
J0217+0127	4.7	PL	1.85	0.20					< 17.21	1.6	< 8.88	2.8	$2.51^{+1.27}_{-1.05}$	3.2	< 3.15	1.5	PKS 0215+015	3	fsrq
J0221+4250	9.8	PL	2.20	0.13					$7.65^{+1.47}_{-1.43}$	5.8	$2.01^{+0.38}_{-0.36}$	6.8	$0.67^{+0.22}_{-0.19}$	4.6	< 0.33	0.0	3C 66A		BLL
J0221+6208c	7.6	PL	2.33	0.14					$6.69^{+1.49}_{-1.46}$	4.8	$1.65^{+0.37}_{-0.36}$	5.1	$0.50^{+0.18}_{-0.16}$	3.8	< 0.20	0.0			gunid
J0237+1653	6.9	PL	2.26	0.16					$10.74^{+2.44}_{-2.34}$	5.1	$2.00^{+0.65}_{-0.60}$	3.8	< 0.73	0.2	< 1.23	1.0	AO 0235+164	2	bll
J0239+6120	22.9	PL	2.02	0.05					$24.37^{+2.37}_{-2.32}$	11.8	$9.90^{+0.80}_{-0.78}$	16.8	$3.65^{+0.55}_{-0.52}$	10.5	< 2.39	1.2	LS I +61 303		hmxb
J0247+6033	5.0	PL	1.65	0.25					< 10.79	2.2	< 3.03	2.2	$1.46^{+0.57}_{-0.48}$	4.0	< 5.88	1.1	PSR J0248+6021	3	psr
J0252+5038	6.1	PL	2.45	0.19					$4.64^{+1.16}_{-1.13}$	4.3	$0.86^{+0.25}_{-0.24}$	3.9	< 0.38	2.0	< 0.35	0.7	NVSS J025357+510256	2	FSRQ
J0305+7452	4.0	PL	1.60	0.19					< 4.37	0.6	$1.19^{+0.47}_{-0.43}$	3.0	< 1.16	1.8	< 4.22	1.6	PSR J0307+7443	3	psr
J0320+4124	6.3	PL	1.77	0.18					< 8.68	2.2	$2.51^{+0.69}_{-0.65}$	4.5	$1.08^{+0.50}_{-0.43}$	3.2	< 3.95	1.7	NGC 1275	2	rdg
J0328-1645	4.0	PL	1.79	0.36					< 22.53	2.1	< 7.70	2.7	< 4.74	1.6	< 7.43	0.0	RBS 0421	4	bll
J0429-3755	4.7	PL	1.92	0.28					$12.71^{+5.06}_{-4.62}$	3.1	< 6.31	2.6	< 4.57	2.7	< 8.96	0.0	PKS 0426-380	3	BLL
J0442+0046	4.2	PL	2.35	0.21					$6.88^{+2.30}_{-2.19}$	3.3	$1.30^{+0.50}_{-0.46}$	3.2	< 0.49	0.0	< 0.55	0.0	PKS 0440-00	2	fsrq
J0458-2323	6.3	PL	1.95	0.21					< 20.20	2.4	$5.41^{+1.57}_{-1.41}$	5.0	$1.84^{+1.14}_{-0.86}$	3.1	< 3.65	0.0	PKS 0454-234	2	fsrq
J0531+1334	4.1	PL	1.84	0.18					$11.33^{+4.22}_{-3.98}$	3.0	< 5.12	1.5	< 2.22	1.9	< 1.48	0.3	PKS 0528+134	3	FSRQ
J0534+2205	56.9	PL	2.32	0.03					$140.00^{+4.75}_{-4.68}$	42.1	$43.13^{+1.94}_{-1.90}$	36.8	$3.01^{+0.43}_{-0.40}$	12.0	$0.36^{+0.16}_{-0.13}$	4.1	Crab		PWN
J0538-4401	9.5	PL	2.23	0.14					$14.23^{+2.79}_{-2.67}$	6.1	$4.16^{+0.82}_{-0.76}$	7.1	< 0.97	1.5	< 1.54	1.1	PKS 0537-441	2	BLL
J0604-4005	4.4	PL	1.14	0.55					< 16.36	2.8	$1.45^{+0.71}_{-0.59}$	3.1	< 1.76	0.8	< 16.64	2.8	SUMSS J060251-401845	3	bcu
J0617+2239e	14.8	PL	1.74	0.10					$22.35^{+4.83}_{-4.62}$	5.4	$15.65^{+1.87}_{-1.78}$	12.8	$6.19^{+1.74}_{-1.52}$	6.3	< 10.73	0.9	IC 443		SNR
J0634+1749	76.4	PS	1.71	0.09	1232.0	69.1	0.5	0.2	$197.89^{+7.83}_{-7.70}$	38.2	$138.92^{+4.14}_{-4.07}$	67.4	$39.08^{+2.99}_{-2.86}$	28.8	$12.86^{+3.33}_{-2.89}$	8.4	Geminga		PSR
J0634+0633	5.4	PL	1.98	0.27					< 17.85	2.5	$4.79^{+1.27}_{-1.17}$	5.0	< 2.35	1.2	< 6.81	0.3	LAT PSR J0633+0632	3	psr
J0654+4514	6.2	PL	2.39	0.19					$6.29^{+1.72}_{-1.65}$	4.1	$1.42^{+0.39}_{-0.37}$	4.5	< 0.45	1.1	< 0.54	0.1	B3 0650+453	2	fsrq
J0714+3318	7.3	PL	2.16	0.18					$11.56^{+2.40}_{-2.30}$	5.7	$1.75^{+0.62}_{-0.56}$	3.6	$0.77^{+0.39}_{-0.31}$	3.5	< 1.60	0.1			unid
J0723+7122	14.0	PL	1.92	0.09					$12.39^{+2.15}_{-2.07}$	6.8	$5.38^{+0.74}_{-0.70}$	10.4	$1.78^{+0.51}_{-0.45}$	5.8	$1.98^{+1.26}_{-0.95}$	3.1	S5 0716+714		BLL
J0730-1130	5.2	PL	1.76	0.25					< 13.14	1.3	$4.83^{+1.33}_{-1.21}$	5.0	< 2.42	1.1	< 6.60	1.3	PKS 0727-11	3,5	fsrq
J0733-7655	4.3	PL	2.10	0.19					< 5.85	2.4	$1.00^{+0.37}_{-0.34}$	3.2	< 0.66	1.4	< 1.47	1.1	PKS 0736-770	3	bcu
J0819+4237	4.3	PL	1.34	0.20					< 4.77	0.0	< 2.40	1.2	$1.59^{+0.89}_{-0.69}$	3.3	$6.54^{+5.40}_{-3.58}$	3.3	S4 0814+42	2,5	bll
J0835-4514	168.9	PS	1.71	0.04	3913.1	533.6	1.3	0.3	$502.18^{+8.89}_{-8.81}$	89.6	$312.39^{+4.85}_{-4.81}$	128.8	$109.76^{+3.98}_{-3.90}$	61.0	$21.90^{+2.94}_{-2.73}$	17.0	Vela PSR		PSR
J1015-5852	7.7	PL	2.04	0.13					$11.35^{+2.95}_{-2.88}$	4.1	$4.07^{+0.94}_{-0.90}$	4.9	$1.60^{+0.65}_{-0.58}$	3.3	< 5.11	1.3	PSR J1016-5857		PSR
J1020-5906	5.3	PL	1.78	0.22					< 14.74	2.4	$3.32^{+1.09}_{-1.03}$	3.5	$1.99^{+0.93}_{-0.80}$	3.0	< 12.14	2.0	1FGL J1018.6-5856	2,5	hmxb
J1020-5752	10.9	PL	2.13	0.09					$14.99^{+2.83}_{-2.77}$	5.7	$7.47^{+0.97}_{-0.94}$	9.2	< 1.86	2.0	< 3.26	0.4	PSR J1019-5749	2	psr
J1029-5834	9.1	PL	1.91	0.11					< 14.68	2.7	$9.19^{+1.22}_{-1.18}$	9.2	< 3.36	2.9	< 8.17	1.8	PSR J1028-5819	3	psr
J1045-5954	7.8	PL	2.04	0.13					$8.67^{+2.68}_{-2.62}$	3.4	$4.95^{+0.91}_{-0.88}$	6.4	$1.58^{+0.62}_{-0.55}$	3.5	< 2.62	0.0	Eta Carinae		bin

Table 11: Spectral information of 2AGL catalogue sources. See Table 9 for a description of the columns.

									0.1 – 0.3 GeV		0.3 – 1 GeV		1 – 3 GeV		3 – 10 GeV				
Name 2AGL	$\sqrt{TS}$	SM	α	$\Delta\alpha$	E_c	ΔE_c	β	$\Delta\beta$	F_1	$\sqrt{TS}_1$	F_2	$\sqrt{TS}_2$	F_3	$\sqrt{TS}_3$	F_4	$\sqrt{TS}_4$	ID or ass.	Flag	Class.
J1045-5735	9.0	PL	2.26	0.13					$12.40^{+2.15}_{-2.11}$	6.3	$2.84^{+0.60}_{-0.58}$	5.5	$1.08^{+0.36}_{-0.32}$	4.1	< 1.79	1.5	LAT PSR J1044-5737	5	psr
J1048-5836	6.8	PL	2.00	0.10					< 9.26	1.5	$4.68^{+0.91}_{-0.88}$	6.1	$2.10^{+0.66}_{-0.58}$	4.7	< 3.08	0.1	PSR J1048-5832	2,5	psr
J1049-8010	5.5	PL	2.15	0.21					$4.04^{+1.19}_{-1.16}$	3.6	$0.90^{+0.31}_{-0.29}$	3.5	< 0.75	2.4	< 0.60	0.0	PKS 1057-79	2	bll
J1052-6234	6.3	PL	2.40	0.18					$5.72^{+1.66}_{-1.62}$	3.6	$1.37^{+0.40}_{-0.38}$	3.8	< 0.69	2.2	< 0.79	1.2	PMN J1047-6217	2	BCU
J1059-5233	17.0	PL	1.78	0.08					$10.45^{+2.47}_{-2.38}$	4.8	$10.99^{+1.05}_{-1.00}$	15.6	$2.68^{+0.81}_{-0.71}$	5.5	< 8.54	2.5	PSR J1057-5226		psr
J1103-7747	4.4	PL	2.01	0.24					< 5.55	2.0	$1.24^{+0.42}_{-0.40}$	3.4	< 1.12	2.3	< 0.92	0.0	3FGL J1104.3-7736c	3	gunid
J1105+3813	6.1	PL	1.57	0.27					< 11.52	0.8	$3.99^{+1.44}_{-1.26}$	4.2	$3.06^{+1.31}_{-1.05}$	4.8	< 4.96	0.0	Mkn 421	2	bll
J1111-6060	8.9	PL	1.99	0.12					$8.15^{+2.67}_{-2.60}$	3.2	$5.97^{+0.94}_{-0.90}$	7.7	$1.59^{+0.61}_{-0.54}$	3.6	< 2.00	0.0	PSR J1112-6103		psr
J1119-6443	5.0	PL	2.11	0.21					< 8.48	2.1	$2.18^{+0.62}_{-0.59}$	4.0	< 1.46	2.7	< 0.80	0.0	AT20G J112319-641735	3	bcu
J1120-6222	4.9	PL	1.85	0.25					$7.93^{+2.87}_{-2.78}$	3.0	< 3.84	2.6	$1.53^{+0.68}_{-0.59}$	3.2	< 3.97	0.6		2	unid
J1136-6045	4.8	PL	1.58	0.30					< 10.68	1.8	$2.19^{+0.84}_{-0.78}$	3.0	$1.51^{+0.75}_{-0.63}$	3.0	< 8.80	1.4	LAT PSR J1135-6055	2,5	psr
J1138-1724	5.7	PL	2.05	0.22					$8.27^{+2.53}_{-2.41}$	3.7	$1.95^{+0.67}_{-0.61}$	3.7	< 1.49	2.4	< 1.61	0.0	2FHL J1137.9-1710 5BZB J1137-1710	2	BLL
J1158+6009	4.0	PL	2.36	0.21					$4.96^{+1.89}_{-1.80}$	3.0	< 1.77	2.3	< 0.82	2.3	< 0.82	0.9	RX J1154.0+6022	3,5	fsrq
J1203-2701c	4.6	PL	2.36	0.26					$4.17^{+1.43}_{-1.38}$	3.2	$0.91^{+0.33}_{-0.30}$	3.3	< 0.36	0.2	< 0.46	1.1		2,5	unid
J1204-6247	5.3	PL	1.38	0.28					< 10.45	1.5	< 3.54	2.5	$2.86^{+0.91}_{-0.80}$	4.7	< 8.90	0.8	PSR J1203-63	3	psr
J1228+4910	4.0	PL	1.30	0.60					< 18.03	2.0	< 2.93	1.8	$2.14^{+1.31}_{-0.98}$	3.3	< 9.12	0.0	TXS 1226+492	3,5	FSRQ
J1228+0154	5.0	PL	2.32	0.24					$9.61^{+2.97}_{-2.79}$	3.8	$2.12^{+0.82}_{-0.73}$	3.5	< 0.56	0.0	< 2.18	0.0	3C 273	2	FSRQ
J1255-0543	7.5	PL	2.18	0.16					$12.41^{+3.18}_{-3.02}$	4.6	$3.96^{+0.97}_{-0.89}$	5.6	< 2.02	2.1	< 2.13	0.0	3C 279	2	FSRQ
J1312-3403	6.6	PL	2.24	0.17					$5.80^{+1.52}_{-1.47}$	4.2	$1.42^{+0.39}_{-0.36}$	4.5	< 0.75	2.8	< 0.31	0.0		2	unid
J1324-4348	5.4	PL	2.69	0.25					$3.80^{+0.87}_{-0.85}$	4.7	$0.51^{+0.15}_{-0.14}$	3.8	< 0.18	1.7	< 0.13	0.7	Cen A	2	rdg
J1330-5606	4.4	PL	2.40	0.18					$4.47^{+1.38}_{-1.35}$	3.4	< 1.27	2.6	< 0.33	0.8	< 0.78	1.9	PMN J1329-5608	3,5	bcu
J1350+3037	4.0	PL	2.07	0.31					< 14.66	2.8	< 3.23	2.2	< 1.81	2.0	< 1.94	0.0	B2 1348+30B	4	fsrq
J1402-8142	4.4	PL	2.20	0.26					< 5.12	2.8	< 1.22	2.8	< 0.66	2.4	< 0.36	0.0		4	unid
J1407-6136c	4.8	PL	1.72	0.18					< 10.82	0.9	$5.29^{+1.32}_{-1.27}$	4.5	$2.68^{+0.99}_{-0.89}$	3.6	< 2.29	0.0	3FGL J1405.4-6119 PSR J1410-6132 LAT PSR J1413-6205	2	gunid
J1418-6106	14.7	PL	1.83	0.07					$20.14^{+3.72}_{-3.65}$	5.8	$13.83^{+1.41}_{-1.37}$	11.9	$4.51^{+1.01}_{-0.93}$	6.2	< 8.20	2.5	LAT PSR J1418-6058		psr
J1458-6055	7.5	PL	2.31	0.18					$9.25^{+1.90}_{-1.87}$	5.1	$1.93^{+0.45}_{-0.43}$	4.8	< 0.83	2.9	< 0.74	0.6	LAT PSR J1459-6053 3FGL J1456.7-6046	2	unid
J1459-3542	5.6	PL	2.09	0.18					< 6.10	1.9	$1.94^{+0.44}_{-0.41}$	5.5	< 0.51	0.6	< 1.65	0.9	PKS 1454-354	3	fsrq
J1507+1019	5.4	PL	2.15	0.20					$13.13^{+4.50}_{-4.18}$	3.5	$3.55^{+1.40}_{-1.25}$	3.3	< 2.70	2.5	< 4.09	0.9	PKS 1502+106	2	FSRQ
J1509-5854	6.5	PL	2.21	0.18					$8.22^{+2.27}_{-2.24}$	3.8	$2.85^{+0.65}_{-0.63}$	4.8	< 1.06	2.0	< 1.59	1.7	PSR J1509-5850	2	psr
J1513-0905	25.0	PL	2.19	0.05					$39.19^{+3.25}_{-3.17}$	15.3	$12.49^{+1.04}_{-1.01}$	18.4	$1.97^{+0.47}_{-0.42}$	7.0	< 1.94	2.0	PKS 1510-089		FSRQ
J1517-5909	5.4	PL	2.39	0.22					$5.81^{+1.71}_{-1.69}$	3.5	$1.53^{+0.42}_{-0.40}$	4.0	< 0.52	1.6	< 0.29	0.0	PSR J1513-5908	2,5	PSR
J1602-4859	5.2	PL	2.93	0.30					$4.13^{+0.86}_{-0.85}$	5.0	< 0.49	1.6	< 0.09	0.8	< 0.03	0.0	PMN J1603-4904	3	bll
J1616-7716	4.3	PL	2.19	0.24					< 4.78	2.1	$1.02^{+0.31}_{-0.29}$	3.9	< 0.26	0.0	< 1.18	1.4	PKS 1610-77	3,5	fsrq
J1622-4926	7.0	PL	2.14	0.22					$13.36^{+2.93}_{-2.89}$	4.7	$3.71^{+0.90}_{-0.88}$	4.4	< 1.80	2.8	< 1.81	1.5	PSR J1620-4927	2,5	psr
J1624-2406	6.0	PL	2.15	0.19					< 8.83	2.6	$2.50^{+0.56}_{-0.53}$	5.5	< 1.00	1.6	< 1.30	1.0	0FGL J1625.9-2423 1FGL J1623.5-2345c	3	gunid

Table 11: Spectral information of 2AGL catalogue sources. See Table 9 for a description of the columns.

									0.1 – 0.3 GeV		0.3 – 1 GeV		1 – 3 GeV		3 – 10 GeV				
Name 2AGL	$\sqrt{TS}$	SM	α	$\Delta\alpha$	E_c	ΔE_c	β	$\Delta\beta$	F_1	$\sqrt{TS}_1$	F_2	$\sqrt{TS}_2$	F_3	$\sqrt{TS}_3$	F_4	$\sqrt{TS}_4$	ID or ass.	Flag	Class.
J1625-2021	5.2	PL	2.08	0.17					< 11.17	2.9	< 3.93	2.9	< 1.31	2.7	< 0.85	2.1	1FGL J1626.2-2038	4	gunid
J1626-2943	5.5	PL	2.10	0.00					$6.88^{+1.92}_{-1.86}$	3.9	< 2.09	2.7	$0.70^{+0.32}_{-0.27}$	3.1	< 1.45	1.7	PKS 1622-29	1,2	FSRQ
J1626-2511	11.7	PL	2.49	0.10					$9.91^{+1.41}_{-1.38}$	7.8	$2.34^{+0.34}_{-0.32}$	8.5	$0.31^{+0.14}_{-0.12}$	3.0	< 0.45	0.9	PKS 1622-253		fsrq
J1628-4448	7.7	PL	2.68	0.15					$8.12^{+1.30}_{-1.29}$	6.5	$1.02^{+0.25}_{-0.24}$	4.4	< 0.15	0.3	< 0.12	0.3		2	unid
J1631-2039	5.9	PL	2.13	0.19					$6.08^{+1.96}_{-1.89}$	3.4	$1.83^{+0.55}_{-0.52}$	4.0	$0.78^{+0.37}_{-0.32}$	3.0	< 2.14	0.9			unid
J1631-2425	5.9	PL	2.13	0.18					< 9.02	2.7	$2.75^{+0.60}_{-0.57}$	5.6	< 0.67	0.0	< 2.32	1.4	3FGL J1628.2-2431c	3	gunid
J1634-4734e	12.2	PL	2.49	0.11					$16.58^{+1.96}_{-1.95}$	8.9	$3.99^{+0.50}_{-0.49}$	8.8	$0.51^{+0.18}_{-0.17}$	3.2	< 0.50	0.9	HESS J1632-478		pwn
J1635-4704	23.2	PL	2.93	0.06					$21.48^{+1.09}_{-1.08}$	21.2	$2.28^{+0.21}_{-0.20}$	11.8	< 0.21	2.8	< 0.07	1.4	TeV J1634-4716 3FGL J1636.2-4709c	2,5	unid
J1636-4610	9.4	PL	2.73	0.15					$10.00^{+1.37}_{-1.35}$	7.6	$1.44^{+0.27}_{-0.26}$	5.8	< 0.23	0.9	< 0.12	0.0		2,5	unid
J1639-4647	9.7	PL	2.31	0.12					$14.90^{+2.50}_{-2.47}$	6.2	$4.99^{+0.73}_{-0.71}$	7.5	$0.77^{+0.30}_{-0.28}$	3.0	< 1.44	2.5	3FGL J1638.6-4654		spp
J1640-5050c	6.8	PL	2.84	0.17					$4.45^{+0.86}_{-0.85}$	5.4	< 0.53	2.0	< 0.06	0.0	< 0.07	1.5	*3FGL J1643.6-5002	3	unid
J1649-5037	8.4	PL	2.76	0.16					$7.61^{+1.05}_{-1.03}$	7.7	$0.64^{+0.18}_{-0.17}$	3.8	< 0.20	2.8	< 0.09	0.1	PMN J1650-5044	2	bcu
J1654-4704c	5.3	PL	1.98	0.19					$10.65^{+2.92}_{-2.87}$	3.8	$2.39^{+0.80}_{-0.77}$	3.3	< 1.92	2.8	< 2.14	0.6	3FGL J1652.2-4649 3FGL J1655.1-4644 3FGL J1655.7-4712	2	gunid
J1703-5705	5.1	PL	2.68	0.36					$3.14^{+0.79}_{-0.77}$	4.2	< 0.57	2.6	< 0.16	1.7	< 0.11	0.9	3FGL J1702.8-5656	3,5	gunid
J1706-6212	5.1	PL	2.48	0.24					$3.34^{+0.95}_{-0.93}$	3.7	$0.50^{+0.18}_{-0.18}$	3.0	< 0.26	2.0	< 0.07	0.0	MRC 1659-621	2	fsrq
J1710-4429	43.5	PC	1.51	0.10	3025.2	957.4			$72.74^{+4.85}_{-4.77}$	17.9	$50.46^{+2.16}_{-2.12}$	34.6	$23.80^{+2.11}_{-2.02}$	19.1	$4.74^{+1.98}_{-1.65}$	4.1	PSR J1709-4429		PSR
J1715-3815	4.0	PL	2.20	0.29					$7.82^{+2.76}_{-2.72}$	3.0	< 3.63	2.7	< 0.83	0.4	< 1.44	0.2	CTB 37A	3,5	snr
J1718-0432	6.9	PL	2.63	0.21					$5.46^{+1.08}_{-1.05}$	5.5	$0.72^{+0.21}_{-0.20}$	4.0	< 0.24	1.5	< 0.25	1.7	3FGL J1720.3-0428	2	gunid
J1720-3859	5.0	PL	1.96	0.21					< 15.41	2.8	$3.18^{+1.00}_{-0.96}$	3.5	< 2.15	2.3	< 2.76	0.2	3FGL J1721.8-3919	3,5	gunid
J1720-3328	4.0	PL	2.35	0.24					$6.71^{+2.18}_{-2.15}$	3.2	< 2.19	2.2	< 0.66	1.0	< 0.66	0.0	TXS 1714-336	3,5	bll
J1731-0527	6.0	PL	2.09	0.18					< 7.39	1.8	$2.34^{+0.57}_{-0.54}$	5.0	< 1.35	2.2	< 1.31	0.7		3	unid
J1733-3130	9.4	PL	2.12	0.10					< 15.14	2.6	$8.01^{+1.09}_{-1.06}$	8.5	$1.64^{+0.58}_{-0.52}$	3.7	< 1.83	0.0	LAT PSR J1732-3131	2	psr
J1736-7819	5.1	PL	2.40	0.26					$2.63^{+0.91}_{-0.89}$	3.0	$0.67^{+0.20}_{-0.19}$	3.8	< 0.24	1.6	< 0.28	0.8	3EG J1720-7820	2	unid
J1737-3206	10.7	PL	2.15	0.10					$4.27^{+3.29}_{-3.24}$	5.5	$2.10^{+1.05}_{-1.03}$	9.3	$0.51^{+0.59}_{-0.54}$	4.6	< 0.47	0.0	3FGL J1737.3-3214c		spp
J1739-2837	9.9	PL	2.48	0.12					$8.03^{+2.19}_{-2.16}$	3.8	$4.63^{+0.56}_{-0.55}$	9.5	$0.78^{+0.25}_{-0.23}$	3.9	< 1.12	1.6	3FGL J1736.5-2839 3FGL J1740.5-2843		gunid
J1740-3013	8.1	PL	1.97	0.13					< 7.82	0.0	$10.40^{+1.44}_{-1.40}$	8.4	$2.62^{+0.87}_{-0.79}$	4.0	< 6.98	1.9	HESS J1741-302	2	unid
J1741+5126	4.4	PL	2.52	0.23					$2.54^{+0.82}_{-0.80}$	3.3	$0.41^{+0.16}_{-0.15}$	3.0	< 0.10	0.0	< 0.09	0.0	4C +51.37	2	FSRQ
J1743-2051	4.9	PL	1.83	0.21					< 9.40	1.3	$3.60^{+0.88}_{-0.83}$	4.9	< 1.47	0.8	< 3.35	0.8	LAT PSR J1741-2054	3	psr
J1743-2613c	8.6	PL	2.68	0.16					$7.50^{+1.85}_{-1.83}$	4.2	$3.19^{+0.43}_{-0.42}$	8.0	$0.80^{+0.17}_{-0.16}$	5.6	$0.35^{+0.14}_{-0.13}$	3.1			unid
J1744-3045	12.0	PL	1.96	0.08					$14.73^{+4.04}_{-3.96}$	3.8	$13.82^{+1.45}_{-1.41}$	11.5	< 3.47	2.7	< 7.33	1.8	3FGL J1744.7-3043	2	gunid
J1746-2921	6.2	PL	1.49	0.15					< 2.58	0.0	$12.11^{+1.93}_{-1.87}$	7.3	$4.38^{+1.60}_{-1.44}$	3.6	< 15.04	1.2		2,5	unid
J1746-2832	21.6	PL	2.12	0.05					$40.64^{+3.94}_{-3.89}$	11.2	$20.51^{+1.44}_{-1.41}$	17.3	$5.84^{+0.93}_{-0.89}$	8.5	< 6.32	2.1	3FGL J1747.0-2828		gunid
J1747-3232	6.4	PL	2.08	0.15					$10.28^{+3.01}_{-2.95}$	3.6	$3.10^{+0.85}_{-0.81}$	4.1	$1.41^{+0.55}_{-0.49}$	3.4	< 1.63	0.0	LAT PSR J1746-3239		psr
J1748-2950	8.1	PL	1.75	0.11					< 4.60	0.0	$13.47^{+1.78}_{-1.73}$	8.9	$3.31^{+1.25}_{-1.12}$	3.4	< 12.14	2.0	PSR J1747-2958	2	psr
J1749-2448	7.5	PL	2.35	0.14					$11.57^{+2.33}_{-2.29}$	5.3	$2.45^{+0.57}_{-0.55}$	4.8	< 1.13	2.5	< 1.09	1.1	Terzan 5	2	glc

Table 11: Spectral information of 2AGL catalogue sources. See Table 9 for a description of the columns.

									0.1 – 0.3 GeV		0.3 – 1 GeV		1 – 3 GeV		3 – 10 GeV				
Name 2AGL	$\sqrt{TS}$	SM	α	$\Delta\alpha$	E_c	ΔE_c	β	$\Delta\beta$	F_1	$\sqrt{TS}_1$	F_2	$\sqrt{TS}_2$	F_3	$\sqrt{TS}_3$	F_4	$\sqrt{TS}_4$	ID or ass.	Flag	Class.
J1754-2626	6.5	PL	2.67	0.23					< 5.66	1.4	$2.54^{+0.38}_{-0.38}$	7.2	$0.39^{+0.15}_{-0.14}$	3.0	< 0.48	2.6		2	unid
J1760+7821	4.0	PL	2.10	0.00					< 4.38	2.0	< 1.22	2.7	< 0.62	2.2	< 0.81	1.4	S5 1803+784	1,4	bll
J1801-2334	7.5	LP	3.38	0.46	2935.1	543.3	0.7	0.2	< 14.66	0.9	$19.28^{+3.27}_{-3.17}$	6.7	$11.96^{+3.86}_{-3.57}$	3.8	< 10.09	1.8	W28	2	SNR
J1803-3935	9.9	PL	2.20	0.13					$10.93^{+1.81}_{-1.77}$	6.7	$2.51^{+0.47}_{-0.45}$	6.5	$0.60^{+0.25}_{-0.22}$	3.4	< 0.89	0.5	PMN J1802-3940		FSRQ
J1804-2153	5.6	PL	2.10	0.00					$14.71^{+3.55}_{-3.49}$	4.3	$3.41^{+1.06}_{-1.02}$	3.5	< 1.84	1.5	< 0.83	0.0	PSR J1803-2149	1,2	psr
J1810-2339	14.4	PL	1.80	0.09					$19.94^{+3.90}_{-3.81}$	5.5	$11.87^{+1.32}_{-1.28}$	11.3	$4.73^{+1.02}_{-0.93}$	6.9	< 6.78	1.4	PSR J1809-2332		psr
J1813-1245	12.6	PL	2.25	0.09					$18.55^{+2.65}_{-2.61}$	7.5	$5.69^{+0.72}_{-0.70}$	9.4	$1.07^{+0.35}_{-0.32}$	4.1	< 2.27	1.2	LAT PSR J1813-1246		psr
J1820-1150c	6.1	PL	2.55	0.26					$8.55^{+2.03}_{-2.01}$	4.3	$2.02^{+0.44}_{-0.43}$	5.0	< 0.46	1.0	< 0.83	2.8		2	unid
J1822-1336	5.0	PL	2.33	0.38					$8.60^{+2.75}_{-2.71}$	3.2	$2.71^{+0.70}_{-0.68}$	4.2	< 0.85	1.0	< 1.68	1.0	3FGL J1819.5-1345 3FGL J1823.2-1339	2	gunid
J1823-1504	5.7	PL	1.91	0.20					$11.78^{+4.16}_{-4.08}$	3.0	$4.54^{+1.32}_{-1.27}$	3.8	< 3.59	2.9	< 4.63	0.8	0FGL J1821.4-1444	2	unid
J1826-1438	8.4	PL	2.25	0.14					$14.33^{+2.99}_{-2.95}$	5.0	$4.64^{+0.81}_{-0.79}$	6.3	< 1.72	2.5	< 1.78	1.2	LS 5039	2,5	hmxb
J1826-1257	9.0	PL	1.71	0.11					< 18.82	2.2	$9.51^{+1.62}_{-1.57}$	6.7	$4.53^{+1.23}_{-1.13}$	4.9	< 13.56	2.9	LAT PSR J1826-1256	2	psr
J1829+0549	4.5	PL	2.09	0.25					$5.00^{+1.79}_{-1.74}$	3.0	< 1.93	2.6	< 1.14	2.7	< 0.57	0.0	TXS 1827+062	3,5	fsrq
J1829-1450	5.9	PL	2.01	0.16					$11.05^{+3.51}_{-3.45}$	3.3	$4.18^{+1.04}_{-1.00}$	4.5	< 2.11	1.8	< 2.11	0.0	3FGL J1827.3-1446 3FGL J1829.2-1504	2	gunid
J1833-2104	13.0	PL	2.39	0.10					$14.73^{+1.75}_{-1.72}$	9.3	$2.87^{+0.40}_{-0.39}$	8.7	< 0.75	2.5	< 0.29	0.0	PKS 1830-211	2	FSRQ
J1836+5924	41.3	PC	1.21	0.16	1988.4	662.3			$26.69^{+2.60}_{-2.53}$	12.8	$26.17^{+1.29}_{-1.26}$	33.7	$15.01^{+1.43}_{-1.36}$	19.6	$3.32^{+1.23}_{-1.03}$	5.2	LAT PSR J1836+5925		psr
J1838-0623c	8.2	PL	2.61	0.15					$9.94^{+1.78}_{-1.76}$	5.8	$1.30^{+0.38}_{-0.37}$	3.7	$0.34^{+0.13}_{-0.12}$	3.1	< 0.20	0.0	3FGL J1834.8-0630c HESS J1837-069 PSR J1837-0604 3FGL J1838.9-0646 3FGL J1839.3-0552		gunid
J1839-0544	15.3	PL	2.21	0.07					$27.20^{+2.97}_{-2.94}$	9.8	$8.33^{+0.92}_{-0.90}$	10.3	$2.07^{+0.45}_{-0.42}$	5.9	< 1.50	1.7	LAT PSR J1838-0537		psr
J1843-1102	4.9	PL	3.19	0.20					$2.84^{+0.63}_{-0.62}$	4.7	< 0.26	1.4	< 0.05	1.2	< 0.01	0.0	PSR J1843-1113	3,5	psr
J1846-1219	5.8	PL	2.94	0.22					< 2.69	1.8	< 0.36	1.3	< 0.08	0.9	< 0.06	1.9	3FGL J1844.7-1224	4	gunid
J1847-0157	4.9	PL	2.10	0.00					$9.77^{+3.05}_{-3.00}$	3.3	< 3.32	1.6	$2.49^{+0.56}_{-0.52}$	5.6	< 2.29	1.6	3FGL J1848.4-0141	1,2	gunid
J1849+6706	16.7	PL	2.03	0.07					$9.35^{+1.36}_{-1.33}$	7.8	$3.92^{+0.43}_{-0.41}$	12.5	$1.58^{+0.29}_{-0.27}$	8.9	< 0.57	0.0	S4 1849+67		FSRQ
J1856+0119e	13.2	LP	2.54	0.30	1018.7	59.0	1.0	0.1	$13.88^{+4.45}_{-4.33}$	3.3	$34.41^{+3.58}_{-3.50}$	11.2	$14.16^{+2.77}_{-2.61}$	6.5	< 1.38	1.2	W44		SNR
J1857+0015	4.7	PL	1.77	0.21					< 8.23	0.3	$4.06^{+1.12}_{-1.07}$	4.0	< 2.59	2.4	< 2.11	0.0		3	unid
J1859+0219	4.2	PL	1.70	0.24					< 7.90	0.0	$4.84^{+1.28}_{-1.23}$	4.2	< 2.54	1.7	< 4.36	1.1	3FGL J1857.9+0210	3	gunid
J1900+0432	8.0	PL	2.65	0.19					$8.80^{+1.49}_{-1.48}$	6.1	$1.67^{+0.33}_{-0.32}$	5.4	< 0.28	1.0	< 0.16	0.5	3FGL J1900.3+0411c	2	gunid
J1905+0656	4.4	PL	2.63	0.23					< 6.55	2.6	$0.94^{+0.32}_{-0.31}$	3.1	< 0.40	2.3	< 0.22	0.6	3FGL J1902.6+0655 3FGL J1906.6+0720	3,5	gunid
J1909+0559	10.6	PL	2.21	0.10					$14.35^{+2.42}_{-2.38}$	6.3	$5.08^{+0.70}_{-0.68}$	8.3	< 1.31	2.9	< 0.45	0.0	LAT PSR J1907+0602	2	psr
J1910-0637	4.9	PL	2.33	0.25					$4.94^{+1.54}_{-1.51}$	3.4	< 1.63	2.8	< 0.62	2.3	< 0.52	0.2		3	unid
J1911+0907	5.4	PL	1.64	0.20					< 5.25	0.0	$4.98^{+1.03}_{-0.99}$	5.6	< 2.43	2.2	< 5.16	1.1	W49B	3,5	snr
J1913+0050	6.1	PL	2.96	0.28					$3.75^{+0.69}_{-0.68}$	5.7	< 0.35	1.8	< 0.07	0.5	< 0.03	0.3		3	unid
J1913-1928	5.0	PL	2.29	0.19					$4.77^{+1.47}_{-1.43}$	3.5	$1.12^{+0.37}_{-0.35}$	3.5	< 0.51	0.7	< 0.33	0.0	PKS B1908-201 PMN J1911-1908	2	unid
J1922-2115	5.1	PL	1.60	0.25					< 5.26	0.4	$2.49^{+0.70}_{-0.65}$	4.5	< 1.73	2.2	< 6.36	2.0	TXS 1920-211	3	fsrq
J1924+1416	7.7	PL	1.96	0.12					< 11.21	2.4	$5.72^{+0.88}_{-0.86}$	7.4	< 1.88	2.4	< 1.47	0.2	W51C	3	snr

Table 11: Spectral information of 2AGL catalogue sources. See Table 9 for a description of the columns.

									0.1 – 0.3 GeV		0.3 – 1 GeV		1 – 3 GeV		3 – 10 GeV				
Name 2AGL	$\sqrt{TS}$	SM	α	$\Delta\alpha$	E_c	ΔE_c	β	$\Delta\beta$	F_1	$\sqrt{TS}_1$	F_2	$\sqrt{TS}_2$	F_3	$\sqrt{TS}_3$	F_4	$\sqrt{TS}_4$	ID or ass.	Flag	Class.
J1927-4318	4.6	PL	1.87	0.27					< 7.95	2.4	$1.52^{+0.55}_{-0.51}$	3.4	< 1.28	1.3	$2.03^{+1.40}_{-1.03}$	3.0		2	unid
J1938-7744	4.6	PL	2.46	0.26					$2.73^{+0.93}_{-0.90}$	3.3	$0.57^{+0.21}_{-0.19}$	3.2	< 0.19	1.0	< 0.27	0.8	3FGL J1925.8-7826	2	gunid
J1953+3258	10.6	PL	1.62	0.13					$8.19^{+2.22}_{-2.15}$	4.0	$4.14^{+0.71}_{-0.67}$	7.4	$2.18^{+0.58}_{-0.52}$	5.9	< 6.64	2.8	PSR J1952+3252		psr
J1957+5017	4.7	PL	1.55	0.31					< 4.87	1.1	$1.34^{+0.41}_{-0.38}$	4.1	< 1.04	1.8	< 4.59	1.2	LAT PSR J1957+5033	3,5	psr
J1958+6519	4.6	PL	1.76	0.36					$3.72^{+1.39}_{-1.33}$	3.0	< 1.51	2.8	< 0.82	1.5	< 3.90	2.8	1ES 1959+650	3	bll
J1958+2853	7.4	PL	1.85	0.13					< 9.93	2.5	$4.35^{+0.75}_{-0.72}$	6.9	< 1.76	2.6	< 1.98	0.0	LAT PSR J1958+2846	3	psr
J2002+4355	5.2	PL	1.79	0.25					< 7.72	2.4	$1.70^{+0.52}_{-0.49}$	3.8	< 1.43	2.4	< 3.91	2.2	MG4 J200112+4352	3	bll
J2005+7225	4.1	PL	2.18	0.42					$3.82^{+1.06}_{-1.03}$	3.9	< 0.84	1.8	< 0.44	1.5	< 0.29	0.0	4C +72.28	3,5	bll
J2020+3824	9.5	PL	2.61	0.17					$13.54^{+1.24}_{-1.23}$	11.6	$2.26^{+0.28}_{-0.27}$	9.1	< 0.17	0.0	< 0.08	0.0	3FGL J2022.2+3840	5	spp
J2021+3654	21.3	PC	1.38	0.30	960.6	361.1			$28.84^{+4.22}_{-4.13}$	7.5	$29.08^{+2.05}_{-2.01}$	18.0	$13.94^{+2.19}_{-2.07}$	8.8	< 2.72	2.1	PSR J2021+3651		PSR
J2021+4029	43.8	PC	1.76	0.09	3307.6	1335.7			$68.47^{+3.48}_{-3.44}$	23.1	$37.36^{+1.47}_{-1.45}$	35.0	$10.21^{+1.02}_{-0.97}$	15.6	$2.04^{+0.91}_{-0.79}$	3.3	Gamma Cygni LAT PSR J2021+4026		SNR
J2025+3352	8.4	PL	2.11	0.13					$12.50^{+1.87}_{-1.84}$	7.2	$2.76^{+0.52}_{-0.50}$	6.1	$0.73^{+0.28}_{-0.25}$	3.4	< 0.69	0.0	B2 2023+33		BCU
J2027-0740	12.0	PL	2.38	0.10					$9.15^{+1.22}_{-1.19}$	8.4	$2.33^{+0.30}_{-0.29}$	9.8	< 0.42	2.1	< 0.22	0.0	PKS 2023-07	2	FSRQ
J2029+4403	6.2	PL	1.93	0.18					$8.08^{+2.18}_{-2.13}$	3.9	$2.38^{+0.62}_{-0.60}$	4.3	$0.90^{+0.40}_{-0.35}$	3.0	< 2.01	0.8		5	unid
J2032+4135	8.6	PL	2.17	0.12					$16.99^{+2.18}_{-2.15}$	8.3	$3.93^{+0.64}_{-0.63}$	6.8	< 1.05	1.8	< 0.63	0.0	LAT PSR J2032+4127	2	psr
J2033+4060	8.2	PL	2.00	0.11					$12.65^{+2.51}_{-2.47}$	5.3	$4.95^{+0.81}_{-0.78}$	6.9	$1.16^{+0.45}_{-0.41}$	3.2	< 0.94	0.0	Cyg X-3		HMXB
J2044+5012e	6.2	PL	1.97	0.17					< 7.33	2.4	$2.24^{+0.50}_{-0.48}$	5.2	< 1.28	2.9	< 0.57	0.0	HB 21	3,5	snr
J2055+2521	5.3	PL	1.77	0.32					< 5.84	1.9	$1.72^{+0.48}_{-0.45}$	4.4	< 1.33	2.4	< 2.43	1.0		3	unid
J2057-4711	6.0	PL	2.05	0.19					< 7.46	2.0	$2.48^{+0.57}_{-0.53}$	5.7	< 0.62	0.7	< 1.95	2.0	PKS 2052-47	3	fsrq
J2144+1730	4.4	PL	2.11	0.25					< 4.87	1.8	$1.15^{+0.34}_{-0.32}$	4.0	< 0.45	0.6	< 1.10	0.0	OX 169	3	fsrq
J2147+0951	5.0	PL	2.34	0.21					$3.38^{+1.10}_{-1.07}$	3.3	$0.84^{+0.26}_{-0.25}$	3.8	< 0.30	0.7	< 0.20	0.0	PKS 2144+092	2	fsrq
J2157-3015	4.9	PL	1.74	0.24					< 12.60	1.7	< 4.32	2.7	$2.46^{+1.00}_{-0.84}$	4.2	< 3.22	0.0	PKS 2155-304	3	bll
J2202+4214	7.8	PL	1.97	0.15					< 5.38	2.3	$2.43^{+0.41}_{-0.39}$	7.5	< 0.69	1.5	< 2.31	2.0	BL Lacertae	3	BLL
J2203+1739	5.5	PL	1.64	0.24					< 4.73	0.8	$2.24^{+0.51}_{-0.48}$	5.7	< 0.84	0.5	< 5.56	1.8	PKS 2201+171	3	fsrq
J2206-1044	4.3	PL	2.30	0.32					$5.32^{+1.73}_{-1.67}$	3.3	< 1.52	2.3	< 0.58	1.8	< 0.58	0.0		3	unid
J2227+6418	7.3	PL	2.75	0.16					$3.39^{+0.66}_{-0.65}$	5.3	$0.34^{+0.12}_{-0.11}$	3.1	< 0.07	0.0	< 0.04	0.0		2	unid
J2228-0818	7.3	PL	2.52	0.21					$7.24^{+1.48}_{-1.44}$	5.4	$1.01^{+0.29}_{-0.28}$	4.1	$0.30^{+0.12}_{-0.11}$	3.3	< 0.26	0.7			unid
J2230+6113	11.0	PL	2.02	0.10					$7.28^{+1.69}_{-1.65}$	4.6	$4.33^{+0.56}_{-0.54}$	9.4	$0.77^{+0.29}_{-0.26}$	3.5	< 2.64	2.0	PSR J2229+6114		PSR
J2232+1132	5.0	PL	1.82	0.24					< 5.69	1.4	$2.01^{+0.53}_{-0.49}$	4.8	< 0.62	0.0	< 4.35	2.7	CTA 102	3	fsrq
J2238+5900	4.3	PL	1.70	0.27					< 5.26	0.8	$2.05^{+0.58}_{-0.54}$	4.2	< 1.09	1.2	< 3.90	1.2	LAT PSR J2238+5903	3	psr
J2247+1558	9.5	PL	2.76	0.15					$5.78^{+0.81}_{-0.80}$	7.6	$0.69^{+0.14}_{-0.13}$	5.6	< 0.19	2.5	< 0.10	1.4	NVSS J224604+154437	2,5	bcu
J2254+1609	55.6	PL	2.21	0.03					$52.86^{+2.00}_{-1.97}$	34.7	$16.54^{+0.65}_{-0.64}$	41.1	$2.67^{+0.31}_{-0.30}$	14.1	$0.83^{+0.36}_{-0.30}$	4.1	3C 454.3		FSRQ
J2303+2120	4.3	PL	2.44	0.24					$2.74^{+0.91}_{-0.89}$	3.2	$0.51^{+0.19}_{-0.18}$	3.1	< 0.13	0.0	< 0.18	0.0		2	unid
J2303+4425	4.4	PL	1.56	0.25					< 1.77	0.0	$1.50^{+0.44}_{-0.41}$	4.2	< 1.37	2.8	< 2.38	0.0	PSR J2302+4442	3,5	psr
J2332+8215c	5.8	PL	2.70	0.75					$2.46^{+0.49}_{-0.49}$	5.3	< 0.34	2.3	< 0.10	1.9	< 0.03	0.0		3	unid
J2336+8009	6.2	PL	2.24	0.19					$3.71^{+0.96}_{-0.94}$	4.1	$0.83^{+0.24}_{-0.22}$	4.0	$0.23^{+0.11}_{-0.09}$	3.0	< 0.20	0.0	1RXS J234051.4+801513	5	bll

Table 12: AGILE astronomer's telegrams (ATEL) in pointing mode and associated 2AGL catalogue sources. The first column reports possible associations with other counterparts, or only the AGL name if no association was possible, the second column reports a classification of the source, the third column the number of Astronomer's Telegram on this source, the fourth and fifth columns the period of integration, the sixth column shows the ID of the Telegram, followed by the 95% circular confidence region parameters in Galactic coordinates (l, b), and radius r in degree. The last column reports an association with a 2AGL source or published paper if the source is not present in the 2AGL catalogue. If the circular confidence region parameters are not present, a direct association is given with the source in the text of the Telegram.

Positionally Consistent (association)	Object Class	ATELs	Start (UTC)	Stop (UTC)	ATEL ID	l	b	r	2AGL Assoc. or published papers
3C 454.3	Blazar	8	2007 Jul 24 14:30	2007 Jul 27 05:27	1160				J2254+1609
			2007 Jul 24 14:30	2007 Jul 30 11:40	1167				
			2007 Nov 02 13:50	2007 Nov 12 17:01	1278				
			2007 Nov 02 12:00	2007 Nov 22 18:33	1300				
			2008 May 24 03:10	2008 May 27 04:17	1545				
			2008 Jun 15 10:46	2008 Jun 16 07:11	1581				
			2008 Jun 25 03:00	2008 Jun 26 03:00	1592				
			2008 Jul 25 18:00	2008 Jul 28 03:00	1634				
PKS 1510-089	Blazar	4	2008 Mar 18 03:00	2008 Mar 20 03:00	1436	351.61	40.09	0.50	J1513-0905
			2009 Mar 08 14:00	2009 Mar 10 4:00	1957	351.15	40.02	0.50	
			2009 Mar 12 07:00	2009 Mar 13 05:00	1968	351.21	40.12	0.50	
			2009 Mar 18 05:45	2009 Mar 19 05:33	1976				
PKS 1830-211	Blazar	1	2009 Oct 12 00:03	2009 Oct 13 04:57	2242				J1833-2104
Mkn 421	Blazar	1	2008 Jun 09 17:02	2008 Jun 15 02:17	1583				J1105+3813
3EG J0721+7120	Blazar	1	2007 Sep 10 13:50	2007 Sep 20 10:13	1221	143.8	27.60	0.40	J0723+7122
3EG J1410-6147	SNR	1	2008 Feb 21 06:00	2008 Feb 22 07:30	1394	312.2	-0.30	0.50	J1407-6136c
W Comae	Blazar	1	2008 Jun 09 17:02	2008 Jun 15 02:17	1582				(Acciari et al. 2009)
AGLJ2021+4029	PWN	3	2008 Apr 27 01:39	2008 Apr 28 01:27	1492	78.01	2.19	1.00	J2021+4029
			2008 May 22 06:00	2008 May 27 06:00	1547	77.90	2.60	0.50	
			2007 Nov 02 12:00	2008 May 01 00:00	1585	78.31	2.05	0.25	
AGL J2021+4032	PWN	1	2008 Nov 16 14:33	2008 Nov 17 14:22	1848	78.30	2.10	0.20	J2021+4029
AGL J2030+4043	HMXB	1	2008 Nov 02 20:43	2008 Nov 03 20:32	1827	79.44	0.85	0.90	J2033+4060/Cygnus X-3
AGL J0229+2054	Unidentified	1	2008 Jul 30 15:34	2008 Jul 31 15:23	1641	151.7	-36.40	1.00	
AGL J1734-3310	Unidentified	1	2009 Apr 14 00:00	2009 Apr 15 00:00	2017	355.17	-0.28	0.65	

Table 13: AGILE only sources. A * in the 'ID or Assoc.' column indicates a possible marginal positional association. See Table 4 for a description of the columns.

Name 2AGL	R.A.	Dec.	l	b	θ_a	θ_b	ϕ	$\sqrt{TS}$	$Flag$	ID or Assoc.	Class
J0714+3318	108.42	33.30	184.44	18.81	0.45	0.17	-54.48	7.3			unid
J1120-6222	169.98	-62.37	292.54	-1.36	0.41	0.23	-3.77	4.9	2		unid
J1138-1724	174.48	-17.39	279.03	42.04	0.32	0.23	24.24	5.7	2	2FHL J1137.9-1710 5BZB J1137-1710	BLL
J1203-2701c	180.85	-27.02	289.91	34.63	0.59	0.31	-25.51	4.6	2,5		unid
J1312-3403	198.09	-34.05	307.87	28.62	0.31	0.27	15.07	6.6	2		unid
J1402-8142	210.49	-81.70	305.58	-19.20	0.41	0.36	25.06	4.4	4		unid
J1628-4448	247.01	-44.80	338.09	2.78	0.43	0.35	-43.83	7.7	2		unid
J1631-2039	247.64	-20.64	356.71	18.64	0.45	0.24	41.00	5.9			unid
J1636-4610	249.00	-46.16	338.05	0.83	0.36	0.33	8.89	9.4	2,5		unid
J1640-5050c	250.06	-50.83	335.04	-2.81	1.02	0.70	-30.25	6.8	3	*3FGL J1643.6-5002	unid
J1731-0527	262.80	-5.45	18.53	15.11	0.55	0.37	42.67	6.0	3		unid
J1736-7819	264.06	-78.32	314.94	-22.86	0.36	0.34	18.19	5.1	2	3EG J1720-7820	unid
J1740-3013	265.02	-30.22	358.28	0.35	0.34	0.18	-12.78	8.1	2	HESS J1741-302	unid
J1743-2613c	265.79	-26.22	2.03	1.88	0.43	0.36	25.58	8.6			unid
J1746-2921	266.48	-29.35	359.68	-0.27	0.18	0.12	8.47	6.2	2,5		unid
J1754-2626	268.45	-26.44	3.07	-0.27	0.66	0.18	-3.44	6.5	2		unid
J1820-1150c	274.95	-11.83	18.81	1.51	0.79	0.26	44.49	6.1	2		unid
J1823-1504	275.63	-15.06	16.27	-0.60	0.19	0.18	-11.26	5.7	2	0FGL J1821.4-1444	unid
J1857+0015	284.22	0.25	33.78	-1.10	0.30	0.24	-13.11	4.7	3		unid
J1910-0637	287.39	-6.62	29.07	- 7.03	0.44	0.33	7.91	4.9	3		unid
J1913+0050	288.19	0.83	36.11	-4.36	0.71	0.60	51.26	6.1	3		unid
J1927-4318	291.73	-43.30	355.07	- 24.37	0.60	0.47	-22.66	4.6	2		unid
J2029+4403	307.21	44.05	81.96	3.06	0.22	0.21	-35.56	6.2	5		unid
J2055+2521	313.75	25.36	70.32	-12.57	0.28	0.20	-49.54	5.3	3		unid
J2206-1044	331.60	-10.73	47.73	-47.92	0.49	0.43	5.35	4.3	3		unid
J2227+6418	336.76	64.29	108.05	5.68	0.68	0.56	-13.91	7.3	2		unid
J2228-0818	336.88	-8.30	55.09	-51.12	0.25	0.20	6.07	7.3			unid
J2303+2120	345.78	21.33	91.79	-34.91	0.54	0.35	-7.50	4.3	2		unid
J2332+8215c	352.99	82.25	120.14	19.82	0.85	0.43	-41.78	5.8	3		unid

Table 14: Unidentified γ-ray sources. See Table 4 for a description of the columns.

Name 2AGL	R.A.	Dec.	l	b	θ_a	θ_b	ϕ	$\sqrt{TS}$	*Flag*	ID or Assoc.	Class
J0221+6208c	35.20	62.13	133.17	1.05	0.57	0.36	-36.16	7.6			gunid
J1103-7747	165.71	-77.78	297.16	-16.14	0.98	0.54	-27.99	4.4	3	3FGL J1104.3-7736c	gunid
J1407-6136c	211.69	-61.59	311.77	-0.02	1.10	0.62	18.72	4.8	2	3FGL J1405.4-6119 PSR J1410-6132 LAT PSR J1413-6205	gunid
J1624-2406	246.12	-24.10	353.00	17.45	0.43	0.24	3.50	6.0	3	0FGL J1625.9-2423 1FGL J1623.5-2345c	gunid
J1625-2021	246.32	-20.35	356.11	19.77	0.43	0.34	-4.23	5.2	4	1FGL J1626.2-2038	gunid
J1631-2425	247.74	-24.41	353.77	16.13	0.51	0.38	-27.45	5.9	3	3FGL J1628.2-2431c	gunid
J1654-4704	253.54	-47.06	339.40	-2.12	0.33	0.23	-20.50	5.3	2	3FGL J1652.2-4649 3FGL J1655.1-4644 3FGL J1655.7-4712	gunid
J1703-5705	255.63	-57.08	332.25	-9.29	0.41	0.33	2.49	5.1	3,5	3FGL J1702.8-5656	gunid
J1718-0432	259.43	-4.54	17.57	18.46	0.69	0.37	-26.05	6.9	2	3FGL J1720.3-0428	gunid
J1720-3859	259.96	-38.99	348.67	-1.01	0.50	0.40	-45.57	5.0	3,5	3FGL J1721.8-3919	gunid
J1739-2837	264.74	-28.62	359.50	1.41	0.37	0.34	8.81	9.9		3FGL J1736.5-2839 3FGL J1740.5-2843	gunid
J1744-3045	265.89	-30.76	358.21	-0.57	0.13	0.11	-0.71	12.0	2	3FGL J1744.7-3043	gunid
J1746-2832	266.55	-28.54	0.41	0.10	0.11	0.09	-41.96	21.6		3FGL J1747.0-2828	gunid
J1822-1336	275.42	-13.61	17.46	0.27	0.39	0.30	-48.47	5.0	2	3FGL J1819.5-1345 3FGL J1823.2-1339	gunid
J1829-1450	277.31	-14.83	17.23	-1.92	0.36	0.18	28.05	5.9	2	3FGL J1827.3-1446 3FGL J1829.2-1504	gunid
J1838-0623c	279.40	-6.38	25.67	0.16	1.06	0.64	14.40	8.2		3FGL J1834.8-0630c HESS J1837-069 PSR J1837-0604 3FGL J1838.9-0646 3FGL J1839.3-0552	gunid
J1846-1219	281.60	-12.32	21.38	-4.48	0.49	0.27	-19.37	5.8	4	3FGL J1844.7-1224	gunid
J1847-0157	281.82	-1.95	30.73	0.04	0.32	0.23	-44.56	4.9	1,2	3FGL J1848.4-0141	gunid
J1859+0219	284.68	2.31	35.82	-0.57	0.37	0.22	57.66	4.2	3	3FGL J1857.9+0210	gunid
J1900+0432	285.09	4.53	37.99	0.08	0.43	0.38	64.03	8.0	2	3FGL J1900.3+0411c	gunid
J1905+0656	286.14	6.93	40.59	0.26	0.79	0.65	2.49	4.4	3,5	3FGL J1902.6+0655 3FGL J1906.6+0720	gunid
J1938-7744	294.53	-77.73	316.69	-28.94	1.08	0.61	-90.00	4.6	2	3FGL J1925.8-7826	gunid

Table 15: 2AGL sources with detection in the range 30-100 MeV. See Table 9 for a description of the columns.

					0.03 - 0.05 GeV		0.05 - 0.1 GeV			
Name 2AGL	$\sqrt{TS}$	SM	α	$\Delta\alpha$	F_a	$\sqrt{TS}_a$	F_b	$\sqrt{TS}_b$	Flag	ID or assoc.
J0007+7308	26.2	PC	1.29	0.22	$58.06^{+20.18}_{-19.85}$	3.0	$23.20^{+6.54}_{-6.40}$	3.7		LAT PSR J0007+7303
J0534+2205	56.9	PL	2.32	0.03	$383.61^{+28.16}_{-27.76}$	15.4	$218.65^{+10.44}_{-10.29}$	25.9		Crab
J0634+1749	76.4	PS	1.71	0.09	< 177.42	2.2	$78.09^{+14.16}_{-13.79}$	6.1		Geminga
J0835-4514	168.9	PS	1.71	0.04	$399.01^{+36.49}_{-35.95}$	12.1	$438.50^{+15.69}_{-15.51}$	35.7		Vela PSR
J1324-4348	5.4	PL	2.69	0.25	< 44.25	0.8	$11.83^{+3.95}_{-3.89}$	3.1	2	Cen A
J1458-6055	7.5	PL	2.31	0.18	< 60.08	1.3	$20.97^{+5.88}_{-5.81}$	3.7	2	LAT PSR J1459-6053 3FGL J1456.7-6046
J1513-0905	25.0	PL	2.19	0.05	$114.86^{+38.73}_{-37.91}$	3.1	$61.72^{+11.01}_{-10.76}$	6.1		PKS 1510-089
J1517-5909	5.4	PL	2.39	0.22	$50.79^{+17.22}_{-17.05}$	3.0	$17.98^{+5.51}_{-5.45}$	3.3	2,5	PSR J1513-5908
J1622-4926	7.0	PL	2.14	0.22	< 90.21	2.3	$35.37^{+7.67}_{-7.59}$	4.7	2,5	PSR J1620-4927
J1634-4734e	12.2	PL	2.49	0.11	< 72.08	2.1	$18.76^{+5.87}_{-5.82}$	3.3		HESS J1632-478
J1635-4704	23.2	PL	2.93	0.06			$65.40^{+3.92}_{-3.89}$	17.9	2,5	TeV J1634-4716 3FGL J1636.2-4709c
J1636-4610	9.4	PL	2.73	0.15	< 70.05	2.6	$14.89^{+4.70}_{-4.66}$	3.2	2,5	
J1640-5050c	6.8	PL	2.84	0.17			$18.59^{+3.63}_{-3.60}$	5.3	3	*3FGL J1643.6-5002
J1710-4429	43.5	PC	1.51	0.10	< 82.88	1.0	$53.55^{+10.84}_{-10.68}$	5.2		PSR J1709-4429
J1803-3935	9.9	PL	2.20	0.13	< 60.74	1.0	$20.45^{+6.16}_{-6.06}$	3.4		PMN J1802-3940
J1804-2153	5.6	PL	2.10	0.00	$92.14^{+24.36}_{-24.09}$	3.9	$49.98^{+9.03}_{-8.93}$	5.8	1,2	PSR J1803-2149
J1810-2339	14.4	PL	1.80	0.09	< 76.26	0.8	$31.14^{+10.43}_{-10.28}$	3.1		PSR J1809-2332
J1813-1245	12.6	PL	2.25	0.09	< 73.45	1.1	$23.31^{+8.06}_{-7.97}$	3.0		LAT PSR J1813-1246
J1833-2104	13.0	PL	2.39	0.10	$64.95^{+19.96}_{-19.75}$	3.3	$43.80^{+6.17}_{-6.09}$	7.5	2	PKS 1830-211
J1836+5924	41.3	PC	1.21	0.16	< 70.89	1.1	$22.08^{+7.28}_{-7.10}$	3.2		LAT PSR J1836+5925
J1838-0623c	8.2	PL	2.61	0.15	< 63.81	1.5	$19.62^{+5.79}_{-5.74}$	3.5		3FGL J1834.8-0630c HESS J1837-069 PSR J1837-0604 3FGL J1838.9-0646 3FGL J1839.3-0552
J1839-0544	15.3	PL	2.21	0.07	$70.93^{+23.02}_{-22.79}$	3.1	$50.31^{+8.09}_{-8.01}$	6.5		LAT PSR J1838-0537
J1847-0157	4.9	PL	2.10	0.00	< 93.55	1.9	$43.41^{+8.37}_{-8.27}$	5.4	1,2	3FGL J1848.4-0141
J1910-0637	4.9	PL	2.33	0.25			$23.55^{+5.76}_{-5.69}$	4.2	3	
J1924+1416	7.7	PL	1.96	0.12	< 41.57	0.0	$23.66^{+7.48}_{-7.38}$	3.3	3	W51C
J2020+3824	9.5	PL	2.61	0.17	< 56.74	2.5	$20.91^{+3.88}_{-3.85}$	5.5	5	3FGL J2022.2+3840
J2021+4029	43.8	PC	1.76	0.09	< 94.93	2.8	$74.71^{+7.52}_{-7.44}$	10.6		Gamma Cygni LAT PSR J2021+4026
J2025+3352	8.4	PL	2.11	0.13			$27.37^{+5.30}_{-5.23}$	5.4		B2 2023+33
J2027-0740	12.0	PL	2.38	0.10	< 72.31	1.8	$16.95^{+4.96}_{-4.89}$	3.5	2	PKS 2023-07
J2032+4135	8.6	PL	2.17	0.12	< 72.52	2.5	$26.48^{+5.61}_{-5.55}$	4.9	2	LAT PSR J2032+4127
J2254+1609	55.6	PL	2.21	0.03	$113.04^{+20.32}_{-20.09}$	5.8	$74.49^{+6.02}_{-5.95}$	13.6		3C 454.3

Appendix A: AGILE-only sources and the non-detection by Fermi-LAT

In this Appendix, we show that the Fermi-LAT non-detection of some of the short flaring episodes observed by the AGILE-GRID in correspondence of the so-called AGILE-only sources (see Sect. 7.2) might be due to poor exposure and non-optimal viewing angle of the source within the FoV of the instrument.

To verify that, we compared the Fermi-LAT attitude data with the AGILE-GRID data during the time intervals of two transient episodes observed only by AGILE-GRID for the 2AGL J1138-1724 and 2AGL J1402-8142 sources.

For the former case, 2AGL J1138-1724, we compared the AGILE-GRID/FERMI-LAT visibility for the γ-ray flare observed by AGILE-GRID from its position during the one-day time interval MJD 54968.5-54969.5 (see Sect. 7.2). For this period we found that the Fermi-LAT observed the 2AGL J1138-1724 sky region at an off-axis angle greater than 50° for more than 80% of its total exposure time, while for AGILE-GRID the off-axis viewing angle was always below 50° because of the constant pointing attitude (see Fig. A.1, *left panel*)[7]

Analogously, we compared the AGILE-GRID/Fermi-LAT visibility of the 2AGL J1402-8142 sky region during a transient episode detected by AGILE-GRID on the two-day timescale ranging from MJD 54751.5 to MJD 54753.5. Again, for the Fermi-LAT, the source viewing angle is mostly above 50° off-axis, while for the AGILE-GRID the source is almost always in good visibility (see Figure A.1, *right panel*).

Even for AGILE-only detections occurring on longer OB timescales, the AGILE-GRID pointing attitude can always guarantee an optimum source viewing angle with respect to the Fermi-LAT. This is the case, for instance, of the 2AGL J1628-4448 detection during the OB 6200 (30-day long) (see Sect. 7.2). Also on this longer interval, the source visibility for the AGILE-GRID is, for most of the time, well below an off-axis angle of 40°, while for the Fermi-LAT it is just below 50° for 14% of the time (see Fig. A.2).

Besides the source visibility/exposure due to the different observing modes (AGILE-GRID in pointing, Fermi-LAT in all-sky survey observing mode), particularly relevant over short time intervals, other reasons can be invoked to explain the Fermi-LAT non-detection of the AGILE-only sources. Among these, we can consider: source variability, different spectral response of the instruments, event classification algorithms, and background model (especially important for sources near the Galactic plane).

Appendix B: Evaluation of the maximum likelihood method for detection of 2AGL sources

The detection process reported in Sect. 4 can be divided in the following steps: (i) the determination of the seeds, (ii) iterative analysis of seeds, and (iii) refined analysis.

For the evaluation of the list of initial seeds we considered that the most seeds found with the significance TS maps method has also been found with the wavelet method, wherein only one trial for each seed has been carried out. A second trial could be considered during the iterative analysis of seeds.

To evaluate the final number of spurious sources involved in the 2AGL procedure, that is related with the refined analysis, we performed a set of Monte Carlo simulations of AGILE-GRID observations, to compare the data distribution of TS produced by the analysis procedure with that predicted by Wilks's theorem. The probability that the result of a trial in an empty field has $TS \geq h$ is the complement of the cumulative distribution of TS. Simulated data are generated using a background model and the AGILE-GRID IRFs described in Sect. 2. The energy range used is 100 MeV–10 GeV. We considered a typical mean value of the exposure, considering the ring centred at ($l = 39.375, b = -22.024$), simulating observation of an empty field (considering only isotropic background model with $g_{\rm iso} = 5$ and putting $g_{\rm gal} = 0$), adding Poisson-distributed noise to each pixel, and analysing each resulting sky map exactly as flight data. We performed a maximum likelihood analysis at the centre of the ring, keeping the position and spectral index of a candidate source fixed. Figure B.1 shows the resulting TS distribution (left panel) and the related p-value distribution (right panel); if we fit the TS distribution with the function $\eta\chi^2_1(TS)$ if $TS > 1$ (see (Bulgarelli et al. 2012a)) we get $\eta = 0.5$, i.e. $TS = 16$ corresponds to 4σ significance and $TS = 9$ corresponds to 3σ significance.

[7] At high values of the off-axis angle (> 50°), the Fermi-LAT sensitivity is up to 50% lower than the nominal on-axis value.

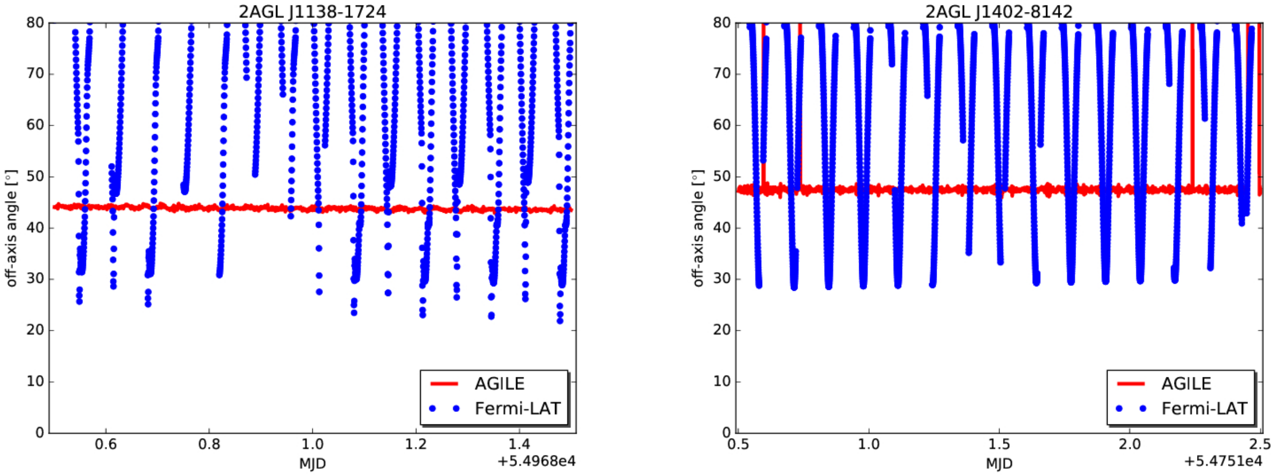

Fig. A.1: *Left panel:* Time-evolution of the off-axis viewing angles for the AGILE-only source 2AGL J1138-1724, as observed by AGILE-GRID (red points) and Fermi-LAT (blue points) during the 1-day time interval MJD 54968.5–54969.5. *Right panel*: The same plot of the AGILE-GRID/Fermi-LAT off-axis viewing angles for the 2AGL J1402-8142 AGILE-only source over the time interval MJD 54751.5–54753.5.

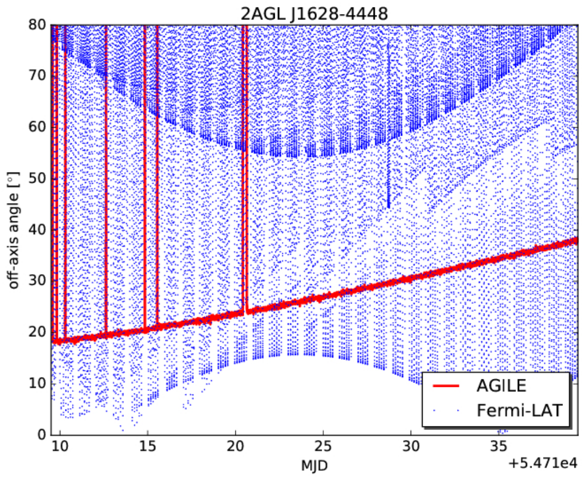

Fig. A.2: Time-evolution of the off-axis viewing angles for the AGILE-only source 2AGL J1628-4448, as observed by the AGILE-GRID (red points) and the Fermi-LAT (blue points) during the 30-day AGILE OB 6200 time-interval (MJD 54719.5-54749.5).

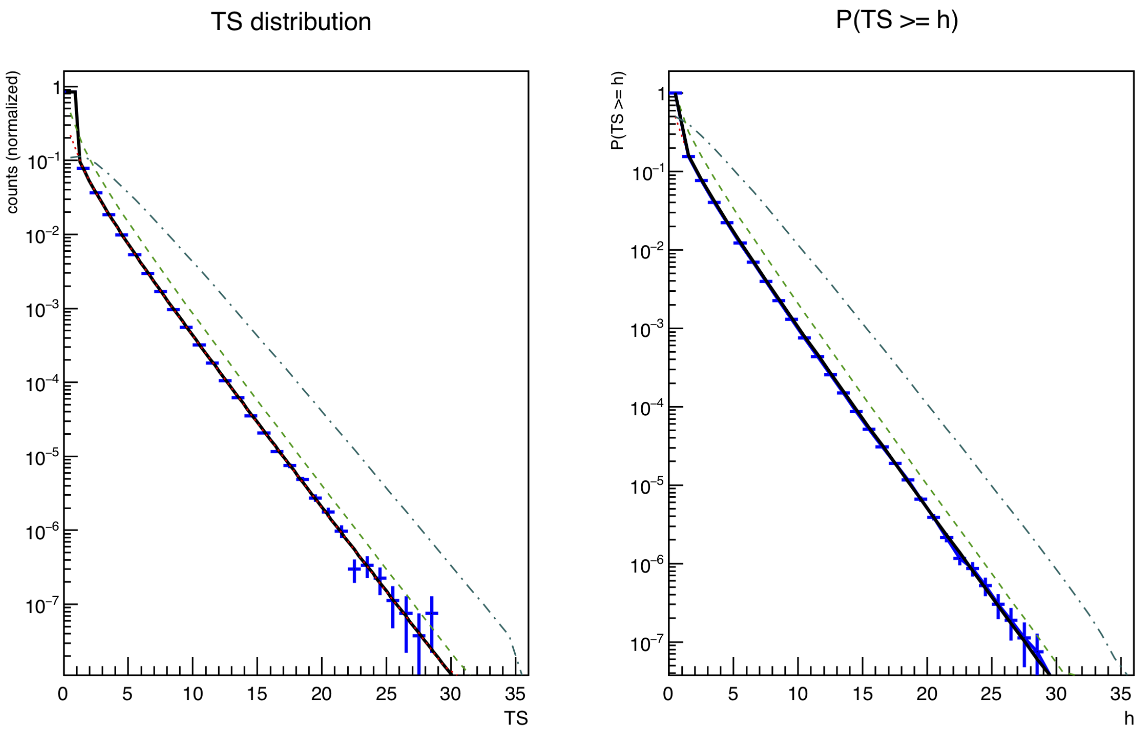

Fig. B.1: TS distribution (left side) and p-distribution (right side) of a simulated empty field, with $g_{\rm gal} = 0$ and $g_{\rm iso} = 5$, flux free, and position and spectral parameters fixed. The blue crosses indicate the calculated distribution, the black line indicates the best fit, the red dotted line indicates the $0.5\chi^2_1$ theoretical distribution, the green dashed line indicates the χ_1 theoretical distribution, and the cyan dash-dotted line indicates the $0.5\chi^2_3$ distribution.